DANISH NATIONAL SPACE CENTER

Surface deformations analyzed using GPS time series

Shfaqat Abbas Khan

Danish National Space Center
Scientific report No. 1, 2005

THE DANISH NATIONAL SPACECENTER IS A RESEARCH CENTER
UNDER THE MINISTRY OF SCIENCE, TECHNOLOGY AND INNOVATION

Surface deformations analyzed using GPS time series

Shfaqat Abbas Khan

Danish National Space Center

Scientific report No. 1

Copenhagen, 2005

ISBN 97-8879-1694-004
ISBN 87-91694-00-0

www.spacecenter.dk

Summary

The aim of this thesis is to analyze GPS time series from continuously operating GPS stations in Denmark, Greenland and Alaska, USA. The study mainly focuses on displacements observed using GPS caused by surface loading of the Earth at different frequencies. The largest surface loading deformations appear with semi-diurnal and diurnal periods and are caused by ocean tides. These effects are relative small but the increasing accuracy of positioning with GPS has made it necessary to take them into account. However, positioning with GPS is not a simple issue of surface displacements, indeed precise positioning requires corrections due to a number of different effects, such as the signal delays through the ionosphere and troposphere, correction due to polar motion etc. Thus, in order to observe surface deformations caused by the ocean tides it is necessary to model, especially the troposphere correctly, and make sure one signal is not absorbed into the other. Chapter 4 is a case study involving the ocean tide loading and the zenith troposphere delay (ZTD). The study demonstrates how the ocean tide loading variations can be observed using GPS, and how absorbtion of the ocean tide loading signal into the zenith troposphere delay can be avoided. Furthermore, when comparing observations with modeled values it is also necessary to consider the accuracy of the model. Thus, the ocean tide loading displacements are modeled using different ocean tide models, moreover, the influence of the coastline resolution is considered. Even though the purpose of the study is to analyze diurnal and semi-diurnal variations, it shows that the different GPS data processing strategies generate signals with period of 12 h, 8 h, 4.8 h, 4 h etc. This led directly to the case study given in Chapter 5. The purpose of this study is to detect the non-linear loading effects at two different superconducting gravity sites in Japan: Esashi and Matsushiro. One is located relatively close to the east coast and the other is close to the west coast of Japan. To compare these gravity observations with tide gauges, several tide gauge sites have been selected located on the east and west coasts of Japan. Hence, it is possible to broadly locate the 'sources' of the observed shallow water loading tides. The study shows that the shallow-water tides at the Japanese east coast have an amplitude of a few millimeters, as observed from tide gauges. However, they are still able to generate an ocean tide loading signal at gravity sites located several hundred kilometers inland.

The second half of the thesis considers secular variations in the GPS signal. These variations are mainly caused by postglacial Rebound. The case study given in chapter 6 focuses on secular vertical surface motions in west Greenland. Wahr et al. [2001] showed that the area is subsiding due to the Earth's viscoelastic response to past ice mass variability. In their study they use GPS data from Kellyville (KELY) and Kulusuk (KULU) (see Figure 6.1). They showed that KELY is sinking by 5.8 +/- 1.0 mm/yr and KULU is sinking by 2.1 +/- 1.5 mm/yr. The subsidence at KELY is explained by glaciation during the last 4000 years, although the area has been deglaciating prior to 4000 years ago. This is in fact supported by geological evidence in the area, which shows that the ice sheet may have expanded about 50 km during the last 4000 years [*Le Meur and Huybrechts*, 1996]. However, the geologic observations were carried out only in the Kangerlussuaq area (near KELY).

Furthermore, the recent uplift model by Tarasov and Peltier do also show subsidence at the western part of Greenland [*Tarasov and Peltier*, 2002]. In their recent GrB ice-sheet margin model they show that the ice sheet margin in west Greenland (between latitude 62° N to 72° N) has re-advanced during the last 8000 years to its current position, resulting in subsidence of land along the west coast. The purpose of this stydy is to take a closer look at the area below latitude of 65° N, and see whether the re-advance of the ice-sheet margin really took place here or if the re-advance only occurred in the mid-western part of Greenland. The question is answered by deriving uplift rates using GPS and tide gauge observations. The GPS measurements from Kely show an average uplift rate of -3.80 ± 0.60 mm/yr. The negative uplift rate (=subsidence) is explained by *Wahr et al.* [2001] as a result of ice margin advancement in the area during the past 4 kyrs. However, GPS measurements at QAQ1 suggest crustal uplift rate of 3.23 ± 1.76 mm/yr, which indeed suggests, the ice margin advancement during the past 4 kyrs did not took place in this area. Additionally, the tide gauge in Nuuk suggests a crustal uplift rate of -1.68 ± 1.75 mm/yr, which indicate the ice margin have not advanced much as 50 km during the past 4 kyrs as near KELY

Acknowledgment

First and foremost I would like to extend my gratitude to my supervisors Carl Christian Tscherning and Per Knudsen for giving me the opportunity to gain an insight into topics hitherto unknown to me. Additionally, I would like to thank Per Knudsen for not only being an excellent supervisor, but also for being a good friend and colleague.

In the beginning of this study I spend some time at the Onsala Space Observatory working with Hans-Georg Scherneck. I am very grateful for all his help and kindness. We had an excellent collaboration resulting in a joint paper. At the end of my study I spend few months in Boulder. Thanks to John Wahr, my stay in Boulder was very successful. I'm very grateful for all that he has done for me. Well, I can only say it has been pleasure learning from the best scientists in the world.

I would like to thank Palle Bo Nielsen from the Royal Danish Administration of Navigation and Hydrography (Farvandsvæsenet) for access to the Greenland tide gauge data. Regarding GPS data, I'm grateful for all the help and support provided by Finn Bo Madsen and Ole B Hansen (from Danish National Space Center). Moreover I would like to thank Jan Johansson from Onsala Space Observatory for help with the installation of the GIPSY OASIS II software.

I would also like to thank all the co-authors appearing on the publications related to this thesis; C C Tscherning, P Knudsen, H.-G. Scherneck, J L Høyer, J Wahr and Eric Leuliette.

Further, I would like to thank my wife and children (N. Shaheen, Maliha and Hasan) for given me the time and support required to complete such a study. Finally I would like to thank all my colleagues at Kort og Matrikelstyrelsen (now at the Danish National Space Center), especially Niels Kjær and Henning Föh.

Shfaqat Abbas Khan

Copenhagen, November 2004

Contents

Chapter 1

Introduction

1.1 History

The first operational satellite-based navigation system called TRANSIT was developed by the Johns Hopkins Applied Physics Laboratory (APL) in 1959 and the first Transit satellite was launched in 1959. In 1963 The Aerospace Corporation started study on using a space system for a navigation system for vehicles moving rapidly in three dimensions. This led directly to the concept of GPS. The world-wide available global positioning system (GPS) is a satellite based system providing precise three-dimensional positions. The system is developed in the U.S.A by the US Department of Defense to provide all-weather round-the-clock navigation capabilities for military ground, sea, and air forces, and was in the beginning primary used for military purposes, but has since become available for civil use e.g. boating, aircraft and hiking. GPS employs 24 satellites in orbits with altitude of 20200 km and an inclination angle of 55 degrees. The orbit period is exactly 12 hours of sidereal day, hence, the satellite configurations repeats every day four minutes earlier with respect to Universal Time, UT. These satellites are placed in 6 orbit planes with four satellites in each plane. The full constellation of 24 spacecrafts was completed on March 9, 1994.

The fundamental positioning principle is based on the measurements of pseudoranges between the user and at least 4 satellites. If precise positioning at centimeter level using short time of observations is desired (few hours), then relative positioning is essential. This requires a fixed reference station with known coordinates and precise GPS satellite orbits. The idea is to measure bias errors between the GPS satellites and the reference station, and then use these bias errors to correct bias errors between the GPS satellites and the station with unknown coordinates. This procedure is also known as Differential GPS (DGPS).

When using DGPS, corrections due to the troposphere, ionosphere, Earth rotation etc. have to be applied. However, with the increasing accuracy of GPS, more and more effects have to be taken into account. *Baker* [1995] showed GPS baseline observations across Great Britain, pointing out the decimeter loading tide range in the vertical. *Lambert et al.* [1998] considered coastal places in eastern and western Canada, using a relatively short section of data. Their investigation treated all tides, lunar as well as solar species, simultaneously. More recently, ocean loading tides have been found to affect the estimate of the zenith tropospheric delay (ZTD), a parameter estimated from GPS that has a potential use in weather prediction as

an indicator of the content of perceptible water in an atmospheric column [*Dragert et al.*, 2000], [*Dach and Dietrich*, 2000].

Additionally, an accuracy of few millimeters may be achieved by averaging GPS estimated site coordinated over a day. *van Dam et al.* [1994] used this high accuracy of precise point positioning (PPP) to detect atmospheric pressure loading in vertical positions at various GPS sites, pointing out the pressure load is largest at higher latitudes. *van Dam and Wahr* [1998] also studied the influence of non-tidal loading and hydrologic loading on vertical GPS displacements. Furthermore, the capability of using GPS to detect crustal motions due Postglacial Rebound is investigated by e.g. *Johansson et al.* [2002] and *Scherneck et al.* [2002]. In their BIFROST-project (Baseline Inferences from Fennoscandian Rebound Observations, Sealevel and Tectonics) they include more than 40 GPS sites located in Fennoscandia to detect the ongoing crustal motions (vertical and horizontal) caused by the last ice age. Their GPS observations agree very well with predicted deformations. Recently, *Wahr et al.* [2001], studied postglacial rebound in Greenland, however, their observed uplift rates could not be explained with existing deglaciation models. Hence, they used the GPS uplift rates to improve existing postglacial rebound models. Their GPS uplift rates are now also used in the latest deglaciation models by *Tarasov and Peltier* [2002].

1.2 This study

The purpose of this thesis is to analyze GPS time series from continuously operating GPS stations. The thesis will focus on semi-diurnal, diurnal, semi-annual, annual and secular motions caused by surface mass loading and try to explain these observed motions by loading models. The semi-diurnal and diurnal surface motions are mainly caused by solid Earth tide and ocean tide loading. Since solid Earth tide is well known and well modeled, it will not be discussed in this thesis. Additionally, it is not a 'load' problem.

The previous studies i.e. by *Dragert et al.* [2000] considered the total loading effect (sum of the main 8 semi-diurnal and diurnal constituents) and claimed that some of the loading signal was absorbed into the tropospheric zenith delay. This thesis will take a step further and look at the main constituents individually. The reason for looking at the constituents individually is; if there are any non-loading surface variations or periodic errors in the GPS signal with periods equal to the considered loading constituents, they will also be absorbed into the troposphere parameters. Chapter 4 is a case study involving ocean tide load, ZTD and GPS and focus on the diurnal and semi-diurnal frequencies.

Furthermore, the aim is to primarily use GPS observations from sites located in Denmark and Greenland. Since the ocean tide loading effect is rather small around Denmark and Greenland, data from Alaska is used. However, the secular surface deformations caused by postglacial rebound are studies for sites in Denmark and Greenland. Chapter 6 deals with postglacial rebound in Greenland and Chapter 7 deals with postglacial rebound in Denmark.

The primary data source used in this thesis is GPS. However, additionally data sources may be used if they are useful and able to confirm or disconfirm conclusions derived upon the GPS data analysis. The case study concerning ocean loading in

Alaska introduced new problems, which led to a case study involving data from Superconducting Gravimeters (SG). Chapter 5 is a case study about non-linear loading tides observed using SG. Furthermore, the case study about postglacial rebound in Greenland does also involve tide gauge observations.

Each of the case studies given in the Chapters 4, 5 and 7 are published in refereed journals or proceeding. The final publications are enclosed in Appendix B.

The study concerning post glacial rebound, GPS and tide gauge in Greenland is ongoing and the results presented here are currently being prepared for publication. The final paper will be submitted to Journal of Geophysical Research by end of January 2005. Co-authors are John Wahr and Eric Leuliette from University of Colorado at Boulder. Furthermore, it should be noticed that the software used for estimation of the uplift rates is fully developed by John Wahr. Additionally, the first part of section 6.5 (regarding Topex/Poseidon and altimetry data) has been written by Eric Leuliette.

Chapter 2

GPS

2.1 Motivation

Positioning with GPS is one among several techniques available for determination of coordinates near or on the Earth. This chapter gives the basic principels of GPS positioning and an introduction to the correction concept. Considering GPS, the basic positioning principle can be regarded as the determination of pseudoranges between a desired point and at least 4 GPS satellites. Pseudoranges or biased ranges means, that a clock reading at the transmitter antenna is compared with clock reading at the receiver antenna. Thus, the travel time from a GPS satellite to a GPS receiver yields the biased range. This requires exact known positions of the satellites and the satellite time. However, the satellites are moving objects and affected by several disturbing forces, which makes it difficult to determine the exact position. The fundamental equation describing the relation between an observation point $\bar{r}_B$ and the satellite position $\bar{r}_S$ can be formulates as [*Seeber*, 1993],

$$\bar{r}_S(t) = \bar{r}_B(t) + \bar{\rho}(t) \tag{2.1}$$

$\bar{\rho}(t)$ is the distance between the satellite and the observation point. The satellite and the observation point are both functions of time, in other words, equation (2.1) contains time dependent effects. To get an overview of these effects it is convenient to divide them into three main groups.

The first group considers e.g. clock parameters and effects, which delays the signal propagating from the satellite to the GPS receiver. The main 'signal delaying' effects included in this group are the tropospheric and the ionospheric delays. The different softwares often estimate bias parameters to take these effects into consideration.

The second group considers geocentric motion of the observation point and the geodynamic parameters giving the relation between the Conventional Terrestrial System CTS (Earth fixed reference system) and the Conventional Inertial System CIS (space fixed reference system). This group includes for instance, Earth rotation, polar motion, solid Earth tide, ocean tide loading etc.

The third group can be related to the satellite orbit motions. The satellite motions cannot be treated as "pure" Keplerian motions. The satellite motions are perturbed from "pure" Keplerian motions by the so-called "perturbing forces". These forces must be applied to the equation of motion to obtain highly accurate

satellite orbits. This group is briefly mentioned in this chapter.

2.1.1 Software packages for GPS data processing

The BERNESE software version 4.2 [*Beutler et al.*, 2000] developed at the University of Berne, Switzerland, and the GIPSY OASIS II software [Zumberge, 1997] developed at the Jet Propulsion Laboratory (JPL), USA, is used to process the GPS data used in this thesis. The BERNESE software estimates station coordinates relative to coordinates of a known station. This processing strategy is also known as differential GPS, since it is the coordinate difference or the baseline between the two stations which is processed. The purpose of processing the baseline between two stations is that some of the errors can be reduced or eliminated. The GIPSY OASIS II software is also able to estimate site coordinates relative to a known station. However, the GIPSY OASIS II software contains a very useful processing strategy, the so-called 'Precise Point Positioning' (PPP), which is able to give single station coordinates with millimeter accuracy (when averaging over 24 hours). PPP is very effective because coordinates for every station are processed individually. Hence, the coordinates do not depend on any reference station. This strategy is very useful when studying e.g. continental drift or postglacial rebound.

2.2 Signal propagation errors and corrections

A signal propagating through a media is affected by the nature and state of the media. The GPS satellites transmit S_{L1} and S_{L2} signals containing carrier phase and code signals. The S_{L1} signal contains a carrier phase L1, a precise code P1 and a less accurate code C/A. The S_{L2} signal contains a carrier phase L2 and a precise code P2. The L1 and and L2 carrier phases have frequencies of ω_1 =1575.72 MHz and ω_2 =1227.60 MHz, corresponding to wavelengths of 19.05 cm and 24.45 cm, respectively. The S_{L1} signal can be described as [*Wübbena*, 1991],

$$S_{L1} = A_p P_i(t) D_i(t) \sin(\omega_1 t) + A_c C_i(t) D_i(t) \cos(\omega_1 t)$$

t is the time and i denotes the i'th satellite. A_p is the amplitude of the P1-code. $P_i(t)$ is the P-code sequence with state ± 1. $D_i(t)$ is the data stream with state ± 1. A_c is the amplitude of the C/A-code and $C_i(t)$ is the C/A-code sequence with state ± 1. The L1 carrier signal is given by $\sin(\omega_1 t)$. Similar, the S_{L2} signal can be described as [*Wübbena*, 1991],

$$S_{L2} = B_p P_i(t) D_i(t) \sin(\omega_2 t)$$

B_p is the amplitude of the P2-code.

Table 2.1: GPS satellite signals.

L1 carrier frequency	1575.42 MHz
L2 carrier frequency	1227.60 MHz
P-code (chipping rate) frequency	10.23 MHz
P-code periods	266 days and / 7 days
C/A-code (chipping rate)	1.023 MHz
C/A-code periods	1 millisecond

The P-code frequency in Table 2.1 corresponds to a wavelength of 29.31 m and the C/A-code frequency corresponds to a wavelength of 293.1 m. The P-code sequence repeats after 266 days. Additionally, portions of 7 days are assigned for each satellite, which makes it possible to identify each satellite, even thought all satellites transmit on the same frequency.

All of these signals propagate through the atmosphere, which is subdivided into the troposphere and the ionosphere. In order to describe the influence of the ionosphere and the troposphere, the basic observation equations are used. However, no attempt to derive the equation will be made here, the equations are given in i.e. the BERNESE GPS software version 4.2 users manual [*Beutler et al.*, 2000, p.153] and the GIPSY OASIS II manual [*Gregorius*, 1996, p. 7],

$$L^i_{Fk} = \varrho^i_k - \Delta\varrho^i_{Fk,ion} + \Delta\varrho^i_{k,trop} + c\delta_k - c\delta^i + \lambda_F n^i_{Fk} \tag{2.2}$$

$$P^i_{Fk} = \varrho^i_k + \Delta\varrho^i_{Fk,ion} + \Delta\varrho^i_{k,trop} + c\delta_k - c\delta^i \tag{2.3}$$

Equation (2.2) is the basic observation equation for the L_1 and L_2 carrier phases and equation (2.3) is the basic observation equation for the P_1 and P_2 code measurements. The index, F, is 1 or 2 corresponding to the two frequencies.

ϱ^i_k.....is the geometric distance between the receiver k and the satellite i
f_F.....is carrier frequency
$\Delta\varrho^i_{Fk,ion}$....is the ionospheric delay
$\Delta\varrho^i_{k,trop}$.....is the tropospheric refraction
$c\delta_k$.....is the receiver clock error and c is the velocity of light
$c\delta^i$.....is the satellite clock error
λ_F.....is the wavelength of the L_F carrier
n^i_{Fk}.....is the unknown integer of cycles, also called phase ambiguity.

Some of the biases and errors can be eliminated or at least reduced by forming differences between the observation equations. Singe differences can be performed between two receivers or two satellites. Double differences are performed between pair of receivers and pair of satellites. This eliminates the receiver clock errors and the satellite clock errors. The BERNESE software and the GIPSY OASIS II software (but not the PPP strategy) performs double differences. Furthermore, triple differences, which are differences of double differences at two different epochs, are performed to eliminate phase ambiguities within given intervals.

2.2.1 Tropospheric effects

The troposphere extends from the surface of the Earth to about 40 km above the surface. Signals propagating in the troposphere are mainly dependent on the air pressure, water vapor and the temperature along the signal path. For GPS stations close to each other, neither the troposphere nor the ionosphere have any large influence on positioning, because the residual errors are almost the same, and thus disappear when using the differential GPS technique. When the distance between stations is more than 50 km [*Seeber*, 1993, p. 307], the troposphere above each station can be very different. Consequently, the signal delay between any satellite and ground station will be different.

The propagation velocity in a certain media is given by $v = c/n$. Here, c is the velocity in vacuum and n is the "index of refraction". In geodesy the "refractivity" N is used instead of n. The relation between these two indexes is,

$$N = (n - 1) \cdot 10^6$$

When considering the troposphere, the tropospheric refractivity N_T is separated into a dry and a wet component, because they have different behavior along the signal path,

$$N_T = N_d + N_w$$

The total delay due to the tropospheric refraction is obtained by integration along the signal path [*Beutler et al.*, 2000, p. 187].

$$\Delta\varrho_{trop} = \Delta\varrho_{dry,trop} + \Delta\varrho_{wet,trop} = 10^{-6} \int_{r_o}^{r_d} N_d dr + 10^{-6} \int_{r_o}^{r_w} N_w dr \qquad (2.4)$$

The integration is performed from the ground station, r_o, to the effective altitude of the dry, r_d, and the wet, r_w, components, respectively. Mean values of the dry and the wet effective altitudes are $r_d \backsimeq 40$ km and $r_w \backsimeq 11$ km [*Seeber*, 1993, p. 46-47]. N_w and N_d depend on several parameters including the zenith angle z (the angle between the signal path and the vertical, see Figure 2.1).

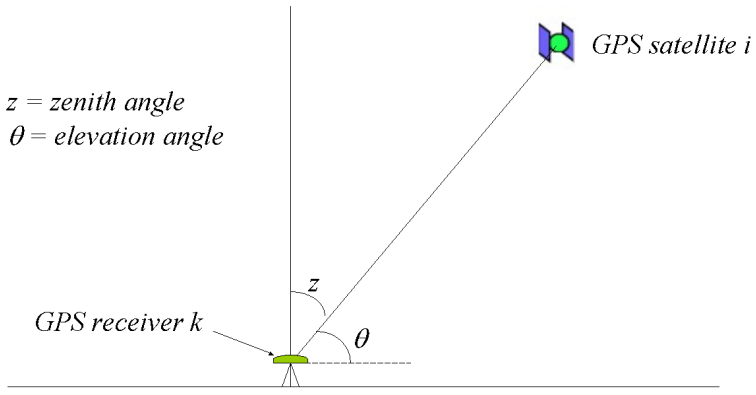

Figure 2.1: Definition of angles

The BERNESE and the GIPSY OASIS II software allow usage of different models, to correct for the tropospheric refraction. All models refer to $z = 0$, meaning that the refraction is estimated for a direct vertical path. The zenith dependency or the actual path is taken into account by multiplying the path delay corresponding to $z = 0$ (will be denoted $\Delta\varrho^0_{trop}$) with a so-called mapping function $f(z)$,

$$\Delta\varrho_{trop} = f_d(z)\Delta\varrho^0_{dry,trop} + f_w(z)\Delta\varrho^0_{wet,trop} \tag{2.5}$$

To first order, all mapping functions are approximately given as $1/\cos(z)$. The default troposphere model available in the BERNESE software package is the Saastamoinen model [*Saastamoinen*, 1973],

$$\Delta\varrho_{trop} = f(z)\Delta\varrho^0_{trop} = \frac{0.002277}{\cos(z)}\Big[p + \Big(\frac{1255}{T} + 0.05\Big)e - \tan^2(z)\Big] \tag{2.6}$$

T is the temperature in degrees Kelvin, p is the air pressure in mbar and e is the partial water vapor pressure in mbar. The BERNESE software allows several other possibilities to model the tropospheric delay. Besides the Saastamoinen model, BERNESE allows usage of the Hopfiled models and the Essen-Frome model.

To show the magnitude of the tropospheric influence Table 2.2 (adopted from *Seeber*, 1993, p.48) is displayed. The table displays the dry and wet tropospheric refractions for different elevation angles. For z=0, the dry tropospheric refraction is about 2.31 meters, while the refraction due to the wet troposphere is about 0.20 meters. However, when using a zenith angle of 5 degrees, the dry tropospheric refraction becomes about 23.61 meters and the wet tropospheric refraction becomes about 2.21 meters.

Table 2.2: Dry and Wet Tropospheric delay for different elevation angles.

Elevation angle z	90^o	20^o	15^o	10^o	5^o
$\Delta\varrho_{dry,trop}$	2.31 m	6.71 m	8.81 m	12.90 m	23.61 m
$\Delta\varrho_{wet,trop}$	0.20 m	0.58 m	0.77 m	1.14 m	2.21 m

The BERNESE software allows usage of meteorological observations, namely the air pressure p, temperature T and humidity H at height h (the station height). However, if meteorological observations are not available, the meteorological parameters are determined using the following expressions [*Berg*, 1948],

$$p = p_r(1 - 0.0000226(h - h_r))^{5.225}$$

$$T = T_r - 0.0065(h - h_r)$$

$$H = H_r e^{-0.0006396(h-h_r)}$$

h_r, p_r, T_r and H_r are reference values. These are set to $h_r = 0$ m, $p_r = 1013.25$ mbar, $T_r = 18$ Celsius and $H_r = 50\%$, which are the recommended values by *Beutler et al.* [2000].

When estimating tropospheric parameters for individual stations, the total tropospheric delay can be formulated as [*Beutler et al.*, 2000],

$$\Delta\varrho_{trop} = f_{apr}(z)\Delta\varrho^0_{apr,trop} + f_{par}(z)\Delta\varrho^0_{par,trop}(t) \tag{2.7}$$

$f_{apr}(z)$ is the a priori mapping function. $\Delta\varrho^0_{apr,trop}$ is the a priori specified zenith delay. $f_{par}(z)$ is the mapping function used for parameter estimation. $\Delta\varrho^0_{par,trop}(t)$ is the zenith troposphere parameter. $\Delta\varrho^0_{par,trop}(t)$ is time dependent. However, the parameters are estimated for some specified time interval e.g. 3 hour. Within the specified time interval, $\Delta\varrho^0_{par,trop}(t)$ is assumed constant. Furthermore, the a priori zenith delay, $\Delta\varrho^0_{apr,trop}$ is introduced, when meteorological observations are used. If no meteorological data are available, it is recommended not to use any a priori model at all.

When using low elevation observations, it is recommended to weight the data with a specified weighting function. Signals with a low elevation angle travel through a longer distance through the troposphere, than signals with high elevation angle. Hence, signals with low elevation angle are more affected by tropospheric noise. On the other hand, usage of observation with low elevation angle improves estimation of the zenith troposphere delay and the vertical site coordinate. The weighting function is therefore introduced to minimize the tropospheric noise by denoting the low angle observations a less weight than observations with a high elevation angle. Based on test with several weighting functions, $w(z)$, *Beutler et al.* [2000, p. 196] recommends the function $w(z) = \cos^2(z)$.

2.2.2 Ionospheric effects

The ionosphere extends from about 50 km to 1000 km above the Earth's surface, remembering that GPS satellites have an altitude of 20200 km above the surface of the Earth. In the ionosphere it is the presence of free electrons and ions, which delay the GPS signal. Similar to the troposphere, the signal delay in the ionosphere is characterised by the index of refraction, n. But here, the signal delay is dependent on the electron density, n_e. The spatial distribution of the electrons is obtained by separating the ionosphere into spherical layers. The principle layers are named D, E, F_1 and F_2. The ionosphere is a dispersive medium, or in other words, the propagation velocity depends on the frequency. The index n for a ionised gas can be formulated as [*Seeber*, 1993, p. 42]

$$n^2 = 1 - n_e\frac{C^2e^2}{\pi f^2 m_e} \qquad \Rightarrow \qquad n_{carrier} \approx 1 - \frac{C\cdot n_e}{f^2} \tag{2.8}$$

Where $C = 40.3$, m_e is electron mass and $e = 1.6022\cdot 10^{-19}$ (the elementary mass). The last expression is obtained by neglecting the higher order terms. This expression can be used for carrier phases. Regarding code measurements, the expression is given by changing the sign,

$$n_{code} = 1 + \frac{C\cdot n_e}{f^2} \tag{2.9}$$

It is obvious, that higher frequencies minimize the last term in equations (2.8) and (2.9), therefore high frequencies are recommended. GPS satellites transmit two frequencies as mentioned in previous section. Since the two frequencies will experience different delays, it is possible to correct for the first-order ionospheric signal delay. The ionospheric delay on L_1 ans L_2 carrier phases are given by,

$$\Delta\varrho_{1,ion} = -\frac{40.3}{f_1^2}\int_s n_e ds \tag{2.10}$$

$$\Delta\varrho_{2,ion} = -\frac{40.3}{f_2^2}\int_s n_e ds \tag{2.11}$$

The ionospheric delays on the P1 and P2 carrier phases are given as in equations (2.10) and (2.11), however, with a positive sign.

2.2.3 Linear combinations

Both carrier phase and code observations lead to pseudoranges. Forming differences or linear combinations of the observations may be useful in order to estimate parameters. A useful linear combination is the so-called wide-lane linear combination of L_1 and L_2. The combination is denoted as L_5,

$$L_5 = \frac{1}{f_1 - f_2}(f_1 L_1 - f_2 L_2) \tag{2.12}$$

The BERNESE software performs the wide-lane combination on double difference level (between pair of receivers, k and l and pair of satellites, i and j). Neglecting the ionospheric refraction, $\Delta\varrho^{ij}_{Fkl,ion}$, and the tropospheric refraction, $\Delta\varrho^{ij}_{kl,trop}$, gives,

$$L^{ij}_{5kl} = \varrho^{ij}_{kl} + \underbrace{\frac{c}{f_1 - f_2}}_{\lambda_5 \simeq 86cm}\underbrace{(n^{ij}_{1kl} - n^{ij}_{2kl})}_{n^{ij}_{5kl}} \tag{2.13}$$

n^{ij}_{5kl} is called the wide-lane ambiguity. The purpose of using L_5 is to detect 'cycle slip', which is a jump in the carrier phase by a integer number of cycles. The advantage of using L_5 is that the ambiguity has to be solved for a signal with wavelength 4 times larger than the original signal. Another very useful linear combination is the narrow-lane or the L_3 combination,

$$L_3 = \frac{1}{f_1^2 - f_2^2}(f_1^2 L_1 - f_2^2 L_2) \tag{2.14}$$

$$P_3 = \frac{1}{f_1^2 - f_2^2}(f_1^2 P_1 - f_2^2 P_2) \tag{2.15}$$

The L_3 is also known as the ionosphere-free linear combination because the ionospheric path delay is eliminated. Performing the L_3 linear combination on double differences and neglecting the tropospheric refraction yields,

$$L^{ij}_{3kl} = \varrho^{ij}_{kl} + c\frac{f_2}{f_1^2 - f_2^2}n^{ij}_{5kl} + \underbrace{\frac{c}{f_1 + f_2}}_{\lambda_3 \simeq 11cm} n^{ij}_{1kl} \tag{2.16}$$

The formal L_3 wavelength is about 11 cm and n^{ij}_{1kl} is called the narrow-lane ambiguity. The ionosphere-free linear combination has the lowest noise level and hence yields the best results.

For GPS signals the ionospheric delay varies from 1 m to 100 m dependent on the total electron content. Additionally, even when performing linear combinations,

the ionosphere is not totally removed because the higher terms in equation (2.8) are neglected. On double difference level the difference between L_3 and the true range is less than few millimeters even for long baselines [*Beutler et al.*, 2000, p.189]. Moreover, for low elevation angles and very high electron content, the difference between L_3 and the true range on zero difference level is few centimeters.

Table 2.3: Maximum vertical ionospheric range error in meter. Adopted from *Wűbbena* (1991).

Frequency	1 order effect	2 order effect	3 order effect
L1	32.5	0.036	0.002
L2	53.5	0.076	0.007
L1/L2	0.0	0.026	0.006

Table 2.3 displays the maximum vertical ionospheric range error on zero difference level. When using both the L_1 and the L_2 frequencies, the first order term is eliminated. The second-order ionospheric delay is caused by the Faraday rotation effect induced by the Earth's magnetic field. In general it is about 1000 times smaller than the first order effect.

2.2.4 Multipath

Multipath simply means, that there is more than one propagation path between the satellite and the receiver. This occurs when the signal from the SV is reflected by objects such as a buildings or even the landscape. The horizontal ground may also reflect the signal. If the receiver is very close to the sea surface, the water may reflect the signal.

Both code and carrier measurements can be affected by multipath. The effect on carrier phase produces phase shift, which is seen as a periodic bias. The error in the carrier phase signal is given by [*Seeber*, 1993, p. 308]

$$\Theta = arctan(\frac{sin\Phi}{\alpha^{-1} + cos\Phi}) \tag{2.17}$$

with amplitude

$$B = A\sqrt{1 + \alpha^2 + 2\alpha cos\Phi} \tag{2.18}$$

where Φ is the phase shift of the reflected signal due to the phase of the direct signal and α is a damping factor between 0 (= no reflection) and 1 (= reflected and not reflected signals are equally damped).
The multipath effect is dependent on the direction of the incoming signal. Hence, the effect is dependent on the satellite geometry. Figure 2.2 shows the observed and calculated multipath effect. Due to changing in the satellite geometry, the effect varies with periods of about 30 min. Earlier results have demonstrated, that the multipath effects can produce an error high as ± 15 cm [*Seeber*, 1993, p. 308], [*Georgiadou et al.*, 1988].

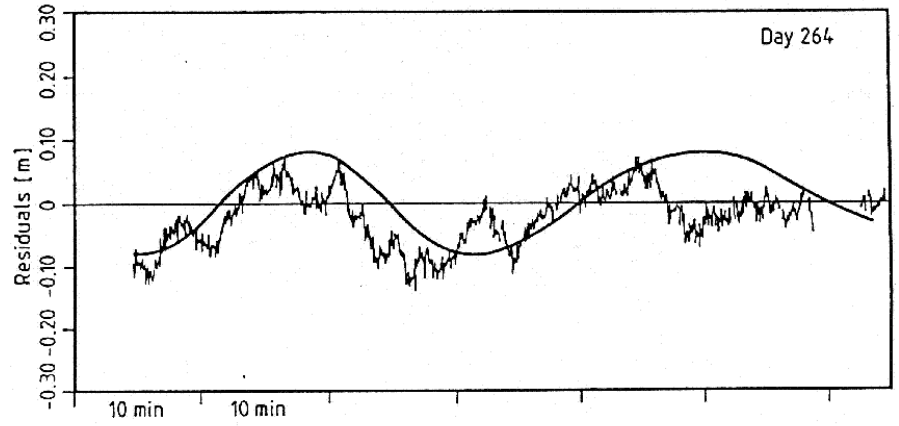

Figure 2.2: Observed and calculated (smooth curve) residuals showing the multipath effect (adopted from [*Seeber*, 1993]).

2.3 Tidal deformations and reference frame related issues

The second group of corrections considers geocentric motion of the observation point and the geodynamic parameters giving the relation between the Conventional Terrestrial System CTS (Earth fixed reference system) and the Conventional Inertial System CIS (space fixed reference system). Example of an Earth fixed reference system is the World Geodetic System, WGS-84. A point given in the CTS-system can be transformed into CIS-system using the expression [*Gregorius*, 1996],

$$\vec{r}_{CTS} = \mathbf{\Omega U W N P} \vec{r}_{CIS} \tag{2.19}$$

$\mathbf{\Omega}$, $\mathbf{U}$, $\mathbf{W}$, $\mathbf{N}$ and $\mathbf{P}$ are all matrixes. $\mathbf{N}$ and $\mathbf{P}$ are the nutation and precession matrixes, respectively. The Earth's rotation axis and the equatorial plane rotate with respect to an inertial system. This rotation is caused by the gravitational attraction of the Sun and the Moon. The resulting motion is composed of a secular mean component (precession) and a periodic component (nutation). $\mathbf{W}$ is the polar motion also known as 'the Wobble' and $\mathbf{U}$ is the Earth rotation. These are difficult to predict theoretically, instead they are observed by the International Earth Rotation Service (IERS). The polar motion is described by two parameters, x_p and y_p (pole coordinates), and the rotation is given by Greenwich Sidereal Time ($GAST$),

$$\mathbf{U} = \begin{pmatrix} \cos(GAST) & \sin(GAST) & 0 \\ -\sin(GAST) & \cos(GAST) & 0 \\ 0 & 0 & 1 \end{pmatrix} \quad \mathbf{W} = \begin{pmatrix} 1 & 0 & x_p \\ 0 & 1 & -y_p \\ -x_p & y_p & 1 \end{pmatrix}$$

The polar motion and the Earth rotation parameters are distributed by the IERS. $\mathbf{\Omega}$ is introduced to compensate for defects in the precession model. Thus, $\mathbf{\Omega}$ is the

perturbation rotation matrix, which describes small rotations about the rotation axis of the CTS-system.

Furthermore, a geocenter offset and scaling factor can be applied to equation (2.19) by,

$$\vec{r}_{A,CIS} = \alpha\vec{r}_{CIS} + \vec{r}_{offs}$$

The scaling factor is denoted, α, and $\vec{r}_{offs}$ is the offset vector.

Additionally, any point at the surface of the Earth will undergo motions caused by tidal effects, postglacial rebound, atmosphere loading etc. The BERNESE and GIPSY OASIS II software take the tidal effects into account,

$$\vec{r}_{B,CIS} = \vec{r}_{CIS} + \vec{r}_{tides} = \vec{r}_{CIS} + \vec{r}_{ET} + \vec{r}_{OT} + \vec{r}_{PT}$$

$\vec{r}_{ET}$ is the solid Earth tide. It is well known and can easily be modeled. $\vec{r}_{OT}$ is the ocean tide loading effect. The parameters (amplitude and phase lags) for each site has to be estimates and stored in a file, which is used by BERNESE or GIPSY. The ocean tide loading effect can easily be turned on or off by the BERNESE and GIPSY softwares. $\vec{r}_{PT}$ is the pole tide. The Earth's rotation axis describes a circle of about 20 m in diameter at the north pole. Taking the tidal effects and the scaling of the reference system into account, equation (2.19) becomes,

$$\vec{r}_{CTS} = \mathbf{\Omega UWNP}(\alpha\vec{r}_{CIS} + \vec{r}_{offs} + \vec{r}_{tides}) \tag{2.20}$$

2.4 Perturbed satellite motions

The third group of corrections are applied to the satellite orbits. When computing precise satellite orbits it is not enough to consider the two-body system containing the satellite and the Earth, where the satellite often in assumed to be massless. Indeed the Sun and the Moon must be included and the satellite mass can not be assumed neglectable. This gives perturbed Keplerian motion for the satellite orbits

$$\ddot{\vec{r}} = -\frac{GM}{r^3}\vec{r}_E + (\ddot{\vec{r}}_E + \ddot{\vec{r}}_S + \ddot{\vec{r}}_M + \ddot{\vec{r}}_P + \ddot{\vec{r}}_D + \ddot{\vec{r}}_{SP} + \ddot{\vec{r}}_A + \ddot{\vec{r}}_e + \ddot{\vec{r}}_o) \tag{2.21}$$

$\ddot{\vec{r}}_E$ is the acceleration due to non-spherically and inhomogeneous mass distribution within the Earth. The direct acceleration due to the Sun is $\ddot{\vec{r}}_S$, Moon $\ddot{\vec{r}}_M$ and other planets $\ddot{\vec{r}}_P$ ($\ddot{\vec{r}}_P$ is neglectable for most purposes). The atmospheric drag is denoted by $\ddot{\vec{r}}_D$, the solar radiation pressure by $\ddot{\vec{r}}_{SP}$ and the Earth reflected solar pressure by $\ddot{\vec{r}}_A$. The last three terms of equation (3.12) are indirect effects caused by tidal phenomenas. The term $\ddot{\vec{r}}_e$ is acceleration due to the solid Earth tide and $\ddot{\vec{r}}_o$ is acceleration due to the ocean tides. The acceleration due to the ocean tides can be computed using a global ocean tide model, such as the GOT00.2 model (*Ray*, [1999]).

2.5 The BERNESE GPS software

The BERNESE GPS software package version 4.2 is used in many scientific studies for various purposes. The software is able to estimate site coordinates, site velocities, Earth rotation parameters, orbit elements, ionosphere maps, troposphere models etc. The software consists of many sub programs, however, here only the main programs used in the data processing mechanism will be described. Furthermore, no attempt for a detailed description of the programs will be desired, instead a brief description of the main purpose will be given. Figure 2.3 shows some of the main programs used for estimation of site coordinates.

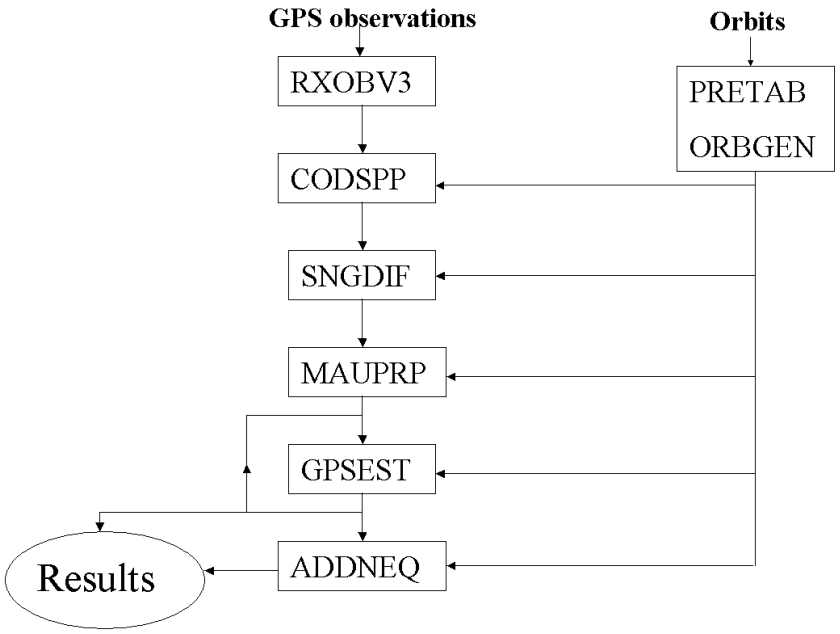

Figure 2.3: Flow diagram of the processing part of the BERNESE GPS software

The GPS data used in this study is given in standard Rinex format. The program, **RXOBV3**, is used to convert the Rinex data to BERNESE format (binary files). **RXOBV3** creates zero differences phase and code observation and header files (totally 4 files). However, before running **RXOBV3**, antenna/receiver and station informations have to be specified in separate files.

The GPS orbit files used in this study are obtained from the International GPS Service (IGS). The orbits are assumed to be error-free. Using **PRETAB** tabular ephemeredes in the J2000.0 system are created, together with satellite clock files. Next, **ORBGEN** is used to create the so-called standard orbits of arc, which are orbits obtained by solving the equation of motion (including the perturbation terms) within some specified time intervals. The output from both, **RXOBV3** and **PRETAB/ORBGEN** is used in the next step, **CODSPP**.

The data processing programs **CODSPP** computes the receiver clock correction, δ_k, while **SNGDIF** creates single differences. The program, **MAUPRP**, is used for cycle-slip screening. The main program, which does most of the processing is **GPSEST**. It generates the ionospheric-free L_3 solutions, troposphere parameters, site coordinates etc. The program has to be run several times depending on the goal of the analysis. **GPSEST** delivers solutions for each observing session, and

the next program, **ADDNEQ**, can be used to combine the solution from **GPSEST** to get a final solution e.g. network solutions for campaigns. For instance, if site coordinates for each day during a week have been estimated using **GPSEST**, then **ADDNEQ** can be used to obtained final site coordinates averaged over the week. However, **ADDNEQ** is not used in this thesis, since the purpose of this study is to analyze time series.

2.6 The GIPSY OASIS II software

The GIPSY OASIS II software is able to process baselines similar to the BERNESE software. Furthermore, GIPSY OASIS II is able to model precise satellite orbits. However, neither the orbit modeling or the baseline processing strategy is used in this thesis, instead the PPP strategy is used for single point positioning. The main idea behind PPP is that orbits and satellite clock parameters are estimated once in a global fiducial frame (or non-fiducial frame). JPL produces these parameters based on a global network of GPS stations. Hence, only the receiver clock parameter, zenith tropospheric delay (ZTD) and station coordinates have to be estimated. The only disadvantage is that the formal errors are too small because the GPS orbits are assumed perfect, which off course is not true. Thus, the formal errors delivered by PPP need scaling by a factor of two or so [*Gregorius*, 1996]. Once the site coordinates are processed in a non-fiducial frame they can be transformed to any reference frame e.g. ITRF1997 or ITRF2000. The daily transformation parameters (7-parameter Helmert transformation) can be obtained from JPL.

Chapter 3

Surface load on a spherical Earth

3.1 Motivation

One of the main problems in geophysics is deformations of the elastic Earth due to external driving forces. The deformations caused by gravitational attraction from the Sun, the Moon and other objects are very well understood and can be modeled very accurately. These tidal deformations are known as direct deformation and called 'body tide'. However, the Sun and Moon also cause tidal harmonic circulations in the oceans, which gives an indirect contribution to harmonic deformations of the Earth. The part of the deformations arising from the harmonic variations of the oceans are also rather well understood, however, modeling of these effects still needs to be improved. Deformations generated by the oceans are known as 'ocean loading' or 'ocean tide loading' if we consider only the tidal variations of the oceans. It is difficult to separate 'body tide' and 'ocean tide loading' from another. Both effects are generated from the same astronomical input, hence, they have a very similar temporal character. However, the spatial character of these two tidal effects may be very different. Body tides varies smoothly over the Earth's surface, and more dependent on the global rheological properties of the Earth rather than the local properties. The ocean tide loading effect has a more irregular varying structure and dependens locally on the elastic properties of the lithosphere (i.e. the upper mantel and crust) [*Farrell*, 1972] and in combination with variations in the ocean amplitudes, gives large loading variations near coastal areas. The various accepted Earth models, such as the Preliminary Reference Earth Model (PREM) [*Dziewonski and Anderson*, 1981]. allow us to accurately the solid Earth tide effect in gravity and surface displacements. Thus, it is possible to separate the ocean tide loading effect (of gravity variations or surface displacemnets) from the solid Earth tide effect, by subtracting the modeled solid Earth tides from the observations.

Modeling of the loading effect requires a model, in time and space, for the surface load and a model for the Earth's structure. The Earth model is used to determine a loading Green's functions, which are weighed sums of load Love numbers and yields the Earth's response to a surface mass load. W. E. Farrell published the standard method for determination of the various loading phenomena in 1972. His work is based on the earlier calculation made by *Longman* [1962,1963], *Alterman* [1959], *Pekeris and Jarosch* [1958]. Farrell's work is very important and is basically used in all present loading estimation programs. He delivered load Love numbers up to degree $n = 10000$ for different Earth models and the associated elastic loading

Green's functions [*Farrell*, 1972].

The theory described by *Farrell* [1972], is valid for an elastic Earth and can be used to determine the Earth's response to 'fast' changing surface loads. The oceans and the atmosphere are good examples of the so-called fast changing surface loads, where the viscous part of the deformations can be neglected. However, when considering 'slow' changing surface loads the viscous part of the deformations has to be considered. Changes in the volume of ice sheets and glaciers occur in the time scale of several hundred years or more. Thus, the deformations arising from the fact that the Earth is viscous are significant and must be taken into account.

In the first part of this chapter, Farrell's analysis of surface loading problem [*Farrell*, 1972] will be followed very closely. The theory is valid for any surface mass load (ocean, atmosphere, etc.). In order to keep things as simple as possible, I will ignore the deformations arising from the viscous Earth, since these can be neglected at the forcing periods I will be considering. However, the viscous problem will be included in the second half of this chapter. These results will be necessary to address the glacial loading problem.

3.2 The convolution integral

To compute the loading effect from e.g. the oceans or the atmosphere, we consider a point mass, dm, located at a distance, α, from the observation point P (see Figure 3.1).

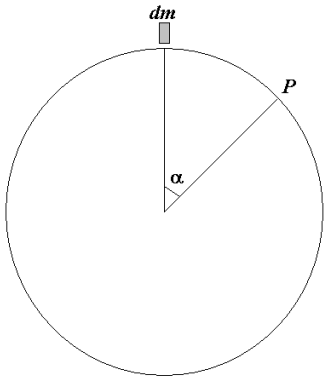

Figure 3.1: Point mass load on a sphere.

The point load has the unit of 1 kg and the mass is concentrated at a single point. The loading effect is given by,

$$dL(\alpha) = \mathcal{G}(\alpha)dm \tag{3.1}$$

The loading effect , dL, represents, for example gravity variations, 3 dimensional surface displacements, changes in the gravitational potential or tilt of the surface. $\mathcal{G}$ is the elastic Green's function, it describes the effect of a delta-function excitation. Furtheremore, the Green's function for e.g. gravity changes is different from the Green's function for vertical displacements. Each load effect has its own Green's function. The total loading effect, or the loading effect from all of the point masses is obtained by integrating over all mass elements,

$$L = \int \mathcal{G}(\alpha) dm \tag{3.2}$$

The above integral is also called the convolution integral, since the Green's function is convolved with the mass load distribution (see also Appendix A3). The integral can be expressed as an integral over the surface of the earth, Ω. Assume a surface element, $d\Omega$, is given by $dm = \rho H d\Omega$, where ρ is the density of the mass element and H is the thickness of the surface element. Then, the integral becomes

$$L = \int_{\Omega} \rho H \mathcal{G}(\alpha) d\Omega \tag{3.3}$$

In order to compute the Greens functions, load Love numbers are required.

3.3 Loading effects on an elastic Earth

3.3.1 Elastic load Love numbers

The solid Earth tide Love numbers, h and k were introduced by Love in 1909, and a third number, l, was introduced by Shida in 1912. However, in order to distinguish these numbers from load Love numbers, the load Love numbers are denoted by a prime, $h_n^{'}$, $l_n^{'}$ and $k_n^{'}$. The load Love numbers and solid Earth tide numbers are different from another. The solid Earth tide Love numbers are obtained assuming, that the surface of the Earth is stress-free, while a normal stress is applied in the case of the load Love numbers. The load Love numbers are obtained by solving the equation of motion, the stress strain relation and the Poisson's equation [*Longman*, 1962], [*Longman*, 1963], [*Farrell*, 1972]. To define the load Love numbers, the vertical surface displacements, u horizontal surface displacements, v, and the potential, ϕ, generated by the surface load are expanded into spherical harmonics,

$$u(\alpha) = \sum_{n=0}^{\infty} U_n(r) P_n(\cos\alpha) \tag{3.4}$$

$$v(\alpha) = \sum_{n=0}^{\infty} V_n(r) \frac{\partial P_n(\cos\alpha)}{\partial \alpha} \tag{3.5}$$

$$\phi(\alpha) = \sum_{n=0}^{\infty} \Phi_n(r) P_n(\cos\alpha) \tag{3.6}$$

$U_n(r)$, $V_n(r)$ and $\Phi_n(r)$ are the harmonic coefficients of the vertical displacement, the horizontal displacement and the potential, respectively. $P_n(\cos\alpha)$ are the Legendre polynomials of the n'th degree. Similarly the external gravity potential caused by a point mass can be expressed as,

$$\psi(\alpha) = \sum_{n=0}^{\infty} W_n P_n(\cos\alpha) \tag{3.7}$$

The harmonic coefficients of the external potential are independent of n and can be written as [*Farrell*, 1972],

$$W_n = \frac{ag}{m_e} \tag{3.8}$$

g is the gravity, a is the radius of the Earth and m_e is the mass of the Earth. For an axially symmetric force field, load Love numbers are defined as [*Farrell*, 1972],

$$U_n = W_n \frac{h_n^{'}}{g} \tag{3.9}$$

$$V_n = W_n \frac{l_n^{'}}{g} \tag{3.10}$$

$$\Phi_n = W_n k_n^{'} \tag{3.11}$$

When determining the Green's functions for the various loading phenomena, solutions for $h_n^{'}$, $nk_n^{'}$ and $nl_n^{'}$ are of interest (this will be discussed in the next section). These functions converge to a constant, when n increases to infinity. Consequently, only 40-50 numbers need to be computed, the remaining numbers can be interpolated using various interpolation schemes, such as cubic spline interpolation. Figure 3.2 displays the load Love numbers from 1 to 10.000 for an unit mass load at the surface of the Earth for two different Earth models (notice that the y-axis is logarithmic). The blue curves show load Love numbers for the Gutenberg-Bullen A Earth model (a spherical symmetric, non-rotating and elastic Earth). The dashed-black curves

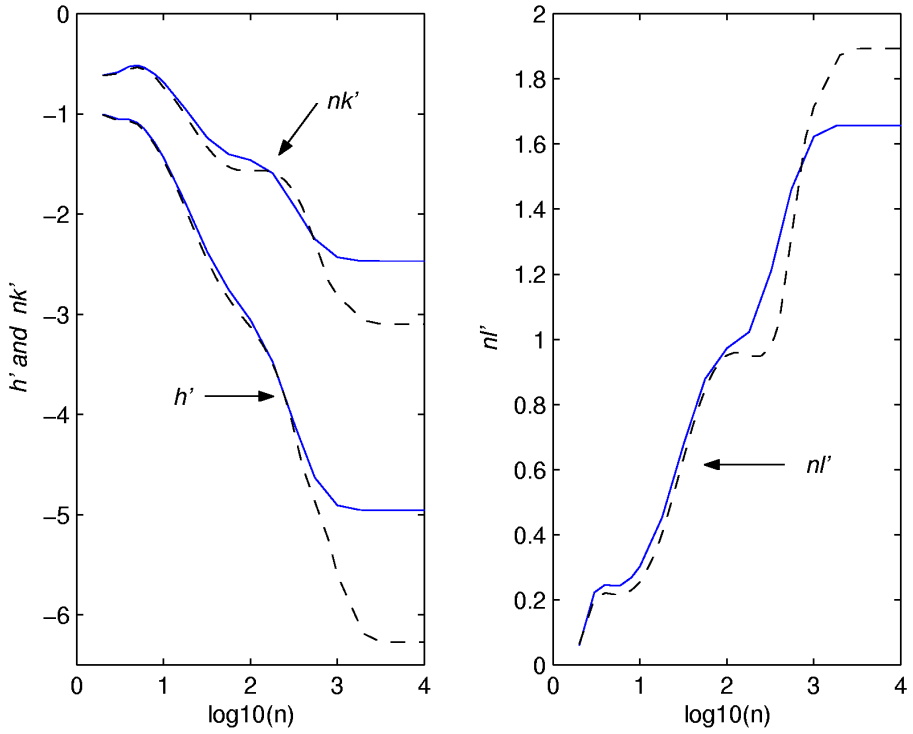

Figure 3.2: Load Love numbers for unit mass load at the surface of the Earth obtained by Farrell (blue curves) and Pagiatakis (dashed-black curves).

show load Love numbers obtained by *Pagiatakis* [1990] for an Earth model with following properties; rotation, Maxwell rheology and anisotropy as specified by the PREM Earth model. The load Love numbers for the two models are very similar for small degrees, while there seems to be larger differences for larger degrees. When using the Gutenberg-Bullen model A, $h_n^{'}$, $nl_n^{'}$ and $nk_n^{'}$ converges to -4.956, 1.657 and -2.469, respectively. Similar, when using the Pagiatakis-model, the values converges to -6.274, 1.894 and -3.097.

3.3.2 Elastic Green's functions

I. M. *Longman* [1962] introduced the elastic loading Green's functions in 1962. These functions represent a weighted sum of load Love numbers and denote the Earth's response to a unit point mass load. The response on the gravity potential at the surface of the Earth is given as a sum of three contributions,

$$\Upsilon_n = W_n + \Phi_n - gU_n \tag{3.12}$$

The first term, W_n, arise from the direct attraction from the surface mass load. The second term, Φ_n, is caused by changes in the mass distribution. The last term, gU_n, is due to vertical motions of the surface. The elastic Green's function for changes in surface gravity is obtained by differentiation of the surface potential with respect to r and making $r = a$ (see appendix A.2),

$$dg_{load}(\alpha) = \frac{g}{m_e}\sum_{n=0}^{\infty}[n + 2h_n^{'} - (n+1)k_n^{'}]P_n(\cos\alpha) \tag{3.13}$$

The elastic Green's function representing vertical displacements is obtained by substituting equation (3.8) and (3.9) into (3.4),

$$u(\alpha) = \sum_{n=0}^{\infty} U_n P_n(\cos\alpha) = \frac{a}{m_e}\sum_{n=0}^{\infty} h_n^{'} P_n(\cos\alpha) \tag{3.14}$$

Similarly, the elastic Green's function used to calculate horizontal displacements is obtained by inserting equation (3.10) into (3.5),

$$v(\alpha) = \sum_{n=0}^{\infty} V_n \frac{\partial P_n(\cos\alpha)}{\partial\alpha} = \frac{a}{m_e}\sum_{n=1}^{\infty} l_n^{'}\frac{\partial P_n(\cos\alpha)}{\partial\alpha} \tag{3.15}$$

In equations (3.13), (3.14) and (3.15) the summation is taken from $n = 0$ to infinity. However, the functions can be computed by evaluating upto a maximum degree N. In order to find N, Farrell defined the limit values by,

$$lim_{n\to\infty}\begin{bmatrix} h_n^{'} \\ nl_n^{'} \\ nk_n^{'} \end{bmatrix} = \begin{bmatrix} h_\infty^{'} \\ l_\infty^{'} \\ k_\infty^{'} \end{bmatrix} \tag{3.16}$$

Substituting (3.16) into (3.14) gives

$$u(\alpha) = \frac{ah_\infty^{'}}{m_e}\sum_{n=0}^{\infty} P_n(\cos\alpha) + \frac{a}{m_e}\sum_{n=0}^{\infty}(h_n^{'} - h_\infty^{'})P_n(\cos\alpha) \tag{3.17}$$

$h_n^{'}$ converges to a constant. Hence, $h_n^{'} - h_\infty^{'}$ becomes zero above $n = N$. Thus, the summation can be carried out for n =0 to $n = N$. Furthermore, the sum in the first term is known exactly (the analytic expression is given in equation A1 in Appendix 1). Substituting the analytic expression of the sum into (3.17) yields,

$$u(\alpha) = \frac{ah_\infty^{'}}{2m_e \sin(\frac{\alpha}{2})} + \frac{a}{m_e}\sum_{n=0}^{N}(h_n^{'} - h_\infty^{'})P_n(\cos\alpha) \tag{3.18}$$

The loading effect on the horizontal displacement is obtained by substituting (3.16) and into (3.15). This gives

$$v(\alpha) = \frac{al_\infty^{'}}{m_e}\sum_{n=1}^{\infty}\frac{1}{n}\frac{\partial P_n(\cos\alpha)}{\partial\alpha} + \frac{a}{m_e}\sum_{n=1}^{\infty}(nl_n^{'} - l_\infty^{'})\frac{1}{n}\frac{\partial P_n(\cos\alpha)}{\partial\alpha} \tag{3.19}$$

$nl_n^{'}$ converges to a constant. Hence, the $nl_n^{'} - l_\infty^{'}$ becomes zero above $n = N$. Again, using the analytic expression for the first sum (see equation A3 in Appendix 1), the horizontal displacements are given by,

$$v(\alpha) = -\frac{al_\infty^{'}}{2m_e}\frac{\cos(\frac{\alpha}{2})\left[1 + 2\sin(\frac{\alpha}{2})\right]}{\sin(\frac{\alpha}{2})\left[1 + \sin(\frac{\alpha}{2})\right]} + \frac{a}{m_e}\sum_{n=1}^{N}(nl_n^{'} - l_\infty^{'})\frac{1}{n}\frac{\partial P_n(\cos\alpha)}{\partial\alpha} \tag{3.20}$$

The expressions for the gravity effect can easily be derived analogue to the above expressions. Using the analytic expression of equation A2, the first term in the bracket in equation (3.13) becomes,

$$\frac{g}{m_e}\sum_{n=0}^{\infty}nP_n(\cos\alpha) = -\frac{g}{m_e}\frac{1}{4\sin(\frac{\alpha}{2})} \tag{3.21}$$

Using the analytic expression given in equation A1, the second term in the bracket in equation (3.13) can be written as,

$$\frac{g}{m_e}\sum_{n=0}^{\infty}2h_n^{'}P_n(\cos\alpha) = \frac{2gh_\infty^{'}}{m_e}\sum_{n=0}^{\infty}P_n(\cos\alpha) + \frac{2g}{m_e}\sum_{n=0}^{\infty}(h_n^{'} - h_\infty^{'})P_n(\cos\alpha)$$

$$= \frac{gh_\infty^{'}}{m_e\sin(\frac{\alpha}{2})} + \frac{2g}{m_e}\sum_{n=0}^{N}(h_n^{'} - h_\infty^{'})P_n(\cos\alpha) \tag{3.22}$$

The third term, which is caused by mass redistribution, can be expressed as,

$$\frac{g}{m_e}\sum_{n=0}^{\infty} -(n+1)(k_n^{'})P_n(\cos\alpha)$$

$$= -\frac{gk_\infty^{'}}{m_e}\sum_{n=0}^{\infty}P_n(\cos\alpha) - \frac{g}{m_e}\sum_{n=0}^{\infty}(nk_n^{'} - k_\infty^{'})P_n(\cos\alpha)$$

$$-\frac{gk_{\infty}^{'}}{m_e}\sum_{n=0}^{\infty}\frac{1}{n}P_n(\cos\alpha)-\frac{g}{m_e}\sum_{n=0}^{\infty}\frac{(nk_n^{'}-k_{\infty}^{'})}{n}P_n(\cos\alpha)$$

$$=\frac{gk_{\infty}^{'}}{m_e}\Big(\frac{1}{2\sin(\frac{\alpha}{2})}-\log\big[\sin(\frac{\alpha}{2})+\sin^2(\frac{\alpha}{2})\big]\Big)-\frac{g}{m_e}\sum_{n=0}^{N}\frac{n-1}{n}(nk_n^{'}-k_{\infty}^{'})P_n(\cos\alpha) \tag{3.23}$$

Normalized Greens function for vertical and horizontal displacements and gravity variations are displayed in Figure 3.3. The Greens functions show the response from a unit mass load at the surface at a distance α from the observations point. Mass elements closest to the observation point have the largest influence on the loading effect and mass elements at a distance of about $\alpha = 90$ degrees has the smallest influence. Furthermore, the loading effect decreases notably between $\alpha = 0$ and $\alpha = 5$ degrees. The functions displayed in Figure 3.3A represent elastic Green's functions for a continental crust. Figure 3.3B displays the vertical displacements elastic Green's functions for a continental crust (dotted curve) and oceanic crust (solid curve). Figure 3.3B shows that the near-field is very different for the two types of crusts, while the far-field is almost the same.

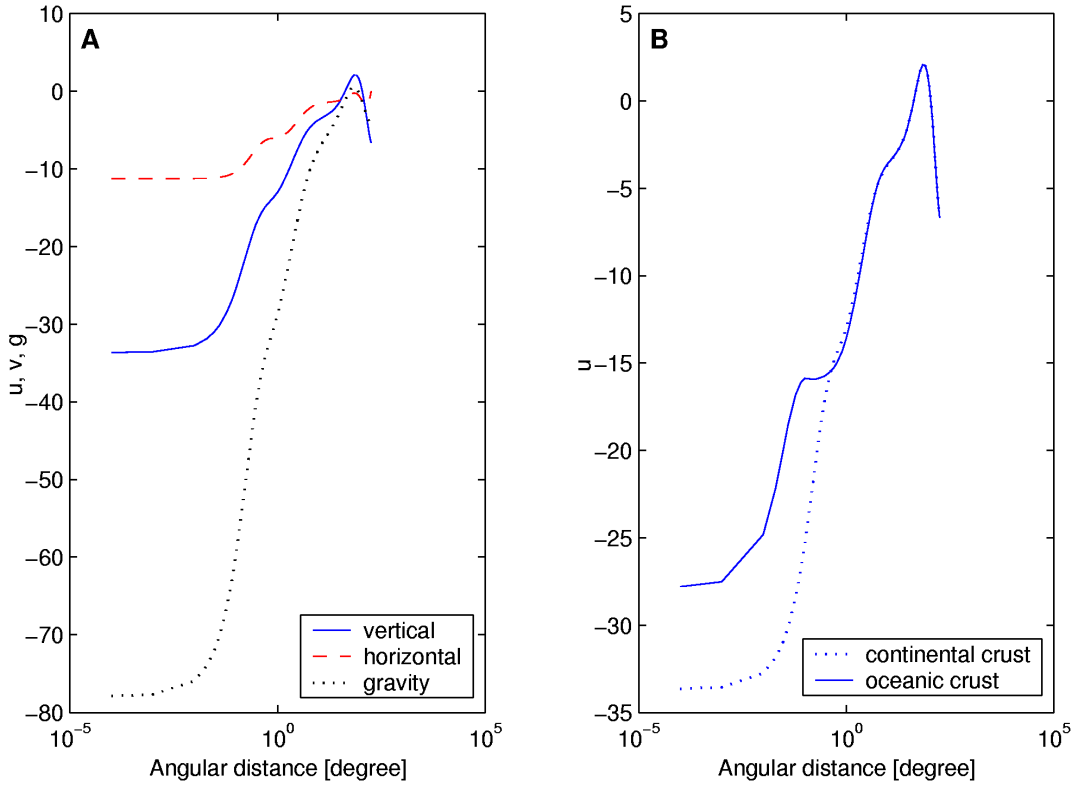

Figure 3.3: A) The blue (solid) curve displays the normalized Greens function for the vertical displacement [x $10^{12}(a\alpha)$, with a=6371 km and α in radians]. The red (dashed) curve displays the horizontal displacement [x$10^{12}(a\alpha)$]. The black (dotted) curve shows the gravity Greens function [x$10^{18}(a\alpha)$] All curves shows applied load of 1 kg. B) Vertical displacements Green's functions for a continental crust (dotted curve) and oceanic crust (solid curve). Notice, x-axis is logarithmic.

3.3.3 Tidal loading and ocean tides

Global ocean tide models are required to calculate the ocean tide loading effects. As seen in Figure 3.3 (Green's function), the near-field has the largest effect on the estimated load, however, it is notable that the far-field is not neglectable. Hence, ocean tide models covering all oceans are required to calculate the loading response at a point. During the past decades, several ocean tide models have been developed, some of them are based on hydrodynamic modeling and some are based on satellite altimetry observations. In general, satellite altimetry based ocean tide models are best in open ocean areas, while models based on tide gauge data and hydrodynamic modeling are best near coastal areas. Most of the satellite altimetry based models use TOPEX/POSEIDON (T/P) altimetry data. The T/P satellite measures the sea surface height and is designed to study the global ocean circulations. The satellite was launched on August 10, 1992 in French Guiana. The satellite has an altitude of 1336 km and an inclination of 66 degrees. Hence, to develop global ocean tide models it is necessary to combine the T/P altimeter data with some other satellite altimeter data (a satellite with higher inclination e.g. ERS1/2) or a hydrodynamic model.

In this thesis, the GOT99.2B ocean tide model developed by *Richard Ray* [1999] is used. The model is a long wavelength adjustment of the FES94.1 model using T/P data and is given on a 0.5 × 0.5 degree grid. Since, T/P is limited to the equator latitudes ± 66-degree, the model is identical to the FES94.1 model outside 66 degree latitudes. The FES94.1 model is a pure hydrodynamic model tuned to fit tide gauges globally and is calculated on a finite element grid with very high resolution near the coastal areas. The model is developed by *Le Provost et al.* [1995].

The various ocean tide models can be represented as a sum of harmonic constituents (or waves), which are determined by their frequencies ω_i, amplitudes A_i and phases φ_i. The total tidal variation is a sum of all the tidal harmonics, however, for most purposes it is sufficient to consider only the main 11 constituents. Each tidal constituent is given a name. Table 3.1 displays the name, period and frequency of the main diurnal, semi-diurnal and long periodic constituents. The ocean tide height can be expressed as,

$$H_{ot} = \sum_{j=1}^{N} H_{j,ot} = \sum_{j=1}^{N} A_j \cos(\omega_j t + \varphi_j) \tag{3.24}$$

N is the total number of tidal constituents. For numerical evaluation of the surface integral given in equation (3.3), the integral is replaced by a sum of surface cells. Considering ocean tide loading effects, the integral can be formulated as,

$$L_{ot}(\lambda, \theta, r, t) = \sum_{i=1}^{M} \rho_i H_{ot}(\lambda_i, \theta_i, t) \mathcal{G}(\alpha_i) d\Omega_i \tag{3.25}$$

The amplitude and phases in equation (3.24) depend on the surface coordinates (λ_i, θ_i). Hence, $H_{ot}(\lambda_i, \theta_i, t)$ denote the mean ocean tide height of the i'th cell at time t. M is the total number of cells. $d\Omega_i$ is the area of the i'th cell. α_i is the angular distance between the observation point and the i'th cell. Normally, the

Table 3.1: Main tidal constituents and their periods

Tidal Constituent	Period	Frequency
K_2	11 h 58 m	2.006 cpd
S_2	12 h 00 m	2.000 cpd
M_2	12 h 25 m	1.933 cpd
N_2	12 h 39 m	1.897 cpd
K_1	23 h 56 m	1.003 cpd
P_1	24 h 04 m	0.997 cpd
O_1	25 h 49 m	0.930 cpd
Q_1	26 h 52 m	0.893 cpd
M_f	13.66 d	0.073 cpd
M_m	27.55 d	0.036 cpd
S_{sa}	0.5 y	0.011 cpd
h:hours	m:minute	d:days
y:years	cpd:cycle per day	

angular distance will be computed from the mid-point of the cell. ρ_i is the mean sea water density of the i'th cell. It mainly depends on the salinity and temperature variations, however, these variations have a rather small influence on the load, thus, ρ_i is considered constant, $\rho = \rho_i$. Concerning the grid resolution, the far-field $\alpha_i > 10\,\text{deg}$, is represented in a grid as given in the ocean tide models (typically 0.5 $\times$ 0.5), while the near field is represented in a much higher grid resolution. A more detailed description of the grid resolution is given in the enclosed paper entitled 'The M_2 ocean tide loading wave in Alaska: Vertical and horizontal displacements, modeled and observed' by *Khan and Scherneck* [2003].

3.4 Loading effects on a viscoelastic Earth

One of the most widely accepted models of the late Pleistocene deglaciation is the ICE-3G model by *Tushingham and Peltier* [1991]. The model is based on the theory described in the papers by *Tushingham and Peltier* [1991] and *Peltier* [1974]. The theory by Peltier is an expansion of the loading description by Longman [1962,1963] and Farrel [1972] as described in previous section.

In order to compute the Earth's response to global glacial load, the behavior of the load in space and time are required together with a viscoelastic Earth model. One can again start with the basic equations, namely the equation of momentum conservation and Poisson's equation [Backus, 1967] in the Laplace domain and expand the vertical u and horizontal v displacements and the potential ϕ into spherical harmonics similar to equations (3.4) to (3.6). However, here the deformation and potential are not only dependent on the distance from the load, but also the spectra s.

$$u(\alpha, s) = \sum_{n=0}^{\infty} U_n(s) P_n(\cos\alpha) \tag{3.26}$$

$$v(\alpha, s) = \sum_{n=0}^{\infty} V_n(s) \frac{\partial P_n(\cos\alpha)}{\partial \alpha} \tag{3.27}$$

$$\phi(\alpha, s) = \sum_{n=0}^{\infty} \Phi_n(s) P_n(\cos\alpha) \tag{3.28}$$

The harmonic coefficients of the vertical displacement $U_n(r, s)$, the horizontal displacement $V_n(r, s)$ and the potential $\Phi_n(r, s)$ depend on spectra s, which is the Laplace transform variable. Since we now are dealing with a viscoelastic Earth, new load Love numbers have to be defined. Setting $r = a$, viscoelastic load Love numbers can be defined as,

$$U_n(s) = W_n \frac{h_n^{'}(s)}{g} \tag{3.29}$$

$$V_n(s) = W_n \frac{l_n^{'}(s)}{g} \tag{3.30}$$

$$\Phi_n(s) = W_n k_n^{'}(s) \tag{3.31}$$

Furthermore, it is convenient to separate the load Love numbers into viscous and elastic terms. Thus, in the spectral domain they can be formulated as,

$$h_n^{'}(s) = h_n^V(s) + h_n^E$$

$$l_n^{'}(s) = l_n^V(s) + l_n^E$$

$$k_n^{'}(s) = k_n^V(s) + k_n^E$$

Note, that the elastic part of the load Love numbers does not depend on the spectra s. In the time-domain, the above equations can be written as,

$$h_n^{'}(t) = h_n^V(t) + h_n^E\delta(t) = \mathcal{L}^{-1}[h_n^V(s)] + h_n^E\delta(t)$$

$$l_n^{'}(t) = l_n^V(t) + l_n^E\delta(t) = \mathcal{L}^{-1}[l_n^V(s)] + l_n^E\delta(t)$$

$$k_n^{'}(t) = k_n^V(t) + k_n^E\delta(t) = \mathcal{L}^{-1}[k_n^V(s)] + k_n^E\delta(t)$$

where $\mathcal{L}^{-1}$ denotes the inverse Laplace transformation. The above elastic load Love numbers are exactly as given in previous section. Now the viscoelastic Green's functions for the vertical and horizontal displacements are given as,

$$u(t, \alpha) = \frac{a}{m_e} \sum_{n=0}^{\infty} [h_n^V(t) + h_n^E\delta(t)] P_n(\cos\alpha) \tag{3.32}$$

$$v(t, \alpha) = \frac{a}{m_e} \sum_{n=1}^{\infty} [l_n^V(t) + l_n^E\delta(t)] \frac{\partial P_n(\cos\alpha)}{\partial\alpha} \tag{3.33}$$

The viscoelastic Green's function for gravity changes and gravitational potential perturbations are given by,

$$dg_{glac}(t,\alpha) = \frac{g}{m_e}\sum_{n=0}^{\infty}\Big(n\delta(t) + 2[h_n^V(t) + h_n^E\delta(t)] \\ -(n+1)[k_n^V(t) + k_n^E\delta(t)]\Big)P_n(\cos\alpha) \tag{3.34}$$

$$\phi(t,\alpha) = \frac{ag}{m_e}\sum_{n=0}^{\infty}(1 + k_n^V(t) + k_n^E\delta(t))P_n(\cos\alpha) \tag{3.35}$$

The total viscoelastic response for any loading phenomenon can be expressed as convolution of the load mass $H(t,\alpha)$ with the appropriate Green's function $G(\alpha, t-t')$,

$$L(t) = \int_{-\infty}^{t} dt' \int_{\Omega} G(t-t',\alpha)H(t',\alpha)d\Omega \tag{3.36}$$

The integration over time is performed from $-\infty$ to the present time, t. The surface loading mass $H(t,\alpha)$ is the total mass change due to deglaciation. Water mass loss of the ice sheets must be gained by the oceans. Thus,

$$H(t,\alpha) = \rho_i H_i(t,\alpha) + \rho_o H_o(t,\alpha) \tag{3.37}$$

The integration in equation (3.36) is performed over all oceans and ice sheets. Hence, $H(t,\alpha)$ must contain the total mass balance history of all oceans and ice sheets . ρ_i is the density of ice and ρ_o is the density of water. The viscoelastic response or lets say the convolution integral with an appropriate Green's function can be solved once the time history of the load is known. In the previous section the hydrodynamical load was given as an 'ocean tide model' based on satellite altimetry data and/or modeling tide gauge observation. Here, the load history of the ice sheets and oceans are determined using the so-called relative sea level (RSL) equation. No attempt to derive the equation is provided here, instead the equation is adopted from Peltier [1998], (also discussed in Farrell and Clark, 1976),

$$\delta RSL(t,\vec{r}) = C(t,\vec{r})\left[\int_{-\infty}^{t} dt' \int_{\Omega} d\Omega\left(H(t',\vec{r'})\frac{\phi(t-t',\alpha)}{g} \right.\right. \\ \left.\left. -u(t-t',\alpha)\right) + \frac{\Delta\mathbb{B}(t)}{g}\right] \tag{3.38}$$

$\vec{r}$ denotes the surface coordinates of the observation point, C is the 'ocean function', it defines the ocean area. C is zero over the continents and one over the oceans. ϕ and u are the gravitational potential perturbations Green's function and vertical displacements Green's function, respectively. $\Delta\mathbb{B}(t)$ is introduced to ensure that the total mass in the RSL equation is conserved.

Chapter 4

The M_2 ocean tide loading wave in Alaska

4.1 Motivation

The Earth undergoes deformation causing measurable displacements of the surface due to a variety of sources. This part of the study will focus on deformation caused by tides. These effects are relatively easy to resolve in observations of geodetic position owing to their nature of almost perfectly stationary, harmonic oscillations with well-defined and band-limited frequencies. The solid Earth tide, or more specifically the deformation of the Earth due to the tidal forces of the Moon and the Sun, is relatively well understood and has a relatively simple spatial structure *Melchior* [1978]. The deformation caused by ocean tide loading, however, is more difficult to predict. These tides appear with the same frequencies as the solid Earth effects. However, the amplitude of the components in phase and out of phase with the solid Earth tide depends strongly on the ocean tide in the region around the observing site. A limit of distance where the ocean tide influence becomes insignificant cannot be given in general.

This case study is an extension of the previous study by *Khan and Tscherning* [2001], which focused on the vertical crustal displacements due to the semi-diurnal ocean tide loading effect, derived from GPS observations in Alaska. However, the aim of this study is to observe the M_2 loading wave using GPS, for both vertical and horizontal displacements. In addition, in order to avoid absorption of ocean tide loading effect into the troposphere modeling, the GPS data will be processed using different strategies. Thereby, the observed M_2 loading wave will be compared with modeled results obtained by different global ocean tide models given on a $0.5^\circ \times 0.5^\circ$ grid resolution. When using the coarse grid resolution as given by the global ocean tide models, the coastal structure is not described very well. In order to study the influence of the coastal resolution on loading, the ocean tide loading effect is modeled using various coastal properties.

4.2 GPS Data Analysis

This study considers variations of the baseline between two GPS sites. Two GPS sites located in Southern Alaska are selected, because the ocean loading effect is

large and consequently easily observed by differential GPS (DGPS).

One GPS-site, FAIR (Fairbanks), is located several hundred kilometers away from the coastline, while the other GPS-site used, CHI3 (Cape Hinchinbrook 3), is located on an island near

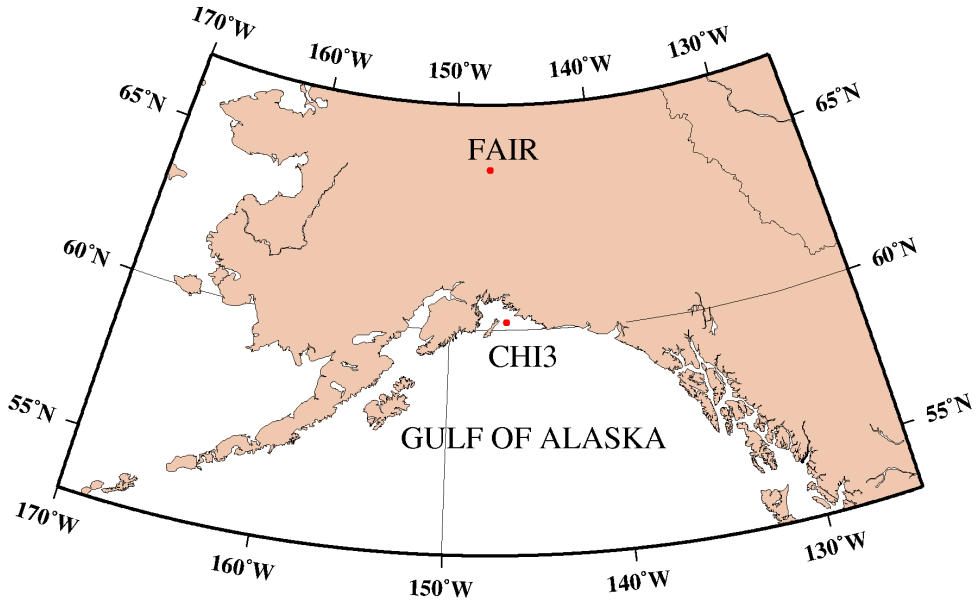

Figure 4.1: Map of Alaska and the location of the selected GPS sites.

the very irregular coastline of southern Alaska Figure 4.1. Hence, the locations of the GPS-sites are perfect for this investigation. The approximate station coordinates are listed in Table 4.1.

Table 4.1: GPS site coordinates

Station name	Latitude degrees	Longitude degrees	Height meter
FAIR (Fairbanks)	64.97800 N	147.4992 W	318.97
CHI3 (Cape Hinchinbrook 3)	60.23751 N	146.6466 W	94.56

Continuous GPS data is analyzed using different strategies for the troposphere correction. The data was sampled during the period of 13 June to 31 July 2000. The data was processed using the BERNESE 4.2 software [*Beutler et al.*, 2000]. Phase ambiguities were solved and kept fixed to integer values. Pole tide and solid Earth tide corrections were applied. Precise IGS satellite orbits were used and kept fixed. Finally, in order to investigate the tropospheric influence on the ocean tide loading effect, the coordinates were estimated using different tropospheric corrections and without applying ocean tide loading corrections. In order to obtain a good tropospheric delay, a cut off angle of 10 degrees was selected (satellite observations below 10 deg were excluded). This should give a good separation of the ocean tide loading and the troposphere. Below are listed different strategies used in this study.

Strategy 1: In the first strategy, the tropospheric influence is ignored. Hence, no tropospheric parameters (ZTD zenith tropospheric delay) were estimated in the

point positioning. However, an a priori Saastamoinen model was applied and hourly position solutions were estimated. This strategy was used by *Khan and Tscherning* [2001]. However, they used an elevation angle of 18 degrees, which was too high.

Strategy 2: First, 1-h ZTD parameters are estimated for each day using the Saastamoinen a priori delays and the 1/cos(Z) mapping function (Z is the zenith angle). These 1-h ZTD estimates derived from 24-h solutions were saved and used in the subsequent processing. Next, hourly site coordinates are estimated by applying the pre-estimated 1-h ZTD parameters based on 24-h solutions.

Strategy 3: In this processing, the site coordinates and ZTD are simultaneously estimated for hourly solutions. Hence, the site coordinates were corrected for the troposphere by applying 1-h ZTD parameters (derived from 1-h solutions). Once again, the 1-h ZTD estimations were carried out using Saastamoinen a priori delays and the cos(Z) mapping function. *Dragert et al.* [2000] and *Kirchner* [2001] used this strategy. However, Dragert used 3-hour sampling intervals instead of 1-h intervals, while Kirchner used 2-h intervals.

The hourly GPS solutions or the raw GPS signal contain variations of the baseline due to a variety of sources e.g. atmosphere loading, non-tidal ocean loading, ocean tide loading and various atmospheric phenomena affecting the GPS signal propagation. Most of these signals do not appear with the same frequencies as the ocean tide loading signal. Variation in the atmosphere e.g. temperature changes have cycles close to the diurnal ocean tide loading frequencies. Therefore, to detect the ocean tide loading signal a good tropospheric correction is necessary. The tropospheric correction can be applied e.g. using metrological data or using estimated ZTD parameters as described above (Strategy 2 and 3). Furthermore, we have to consider perturbations due to satellite orbit errors and multipath. These perturbations appear with the same frequencies as K_1 and K_2 (K_1 has period of 23 h 56 m and K_2 has period of 11 h and 58 m). Consequently, they have no influence on the M_2 loading tide. Moreover, satellite orbit errors can be neglected in baseline double-difference observations.

4.3 Precise ocean load modeling with high resolution coastlines

The ocean loading model computations are carried out with two different methods. One uses the point load convolution method as earlier described in *Scherneck* [1991]. The second one is a global map method, i.e. a modification of a spherical harmonics method originally described in *Ray and Sanchez* [1989]. Here, a gridded global map of loading effects is produced simultaneously. In the convolution method (as described in previous chapter) the tide mass is represented by mass points on a grid, and the convolution integral is replaced by a finite sum. The grid representation is taken from the original tide model grid. The grid constants of the models employed in the present work are $0.5^\circ \times 0.5^\circ$ aligned on half-integer multiples of one degree. However, this relatively coarse grid would create discretization errors of the loading effects in the near-field. Therefore, the grid is refined by a factor of five (grid

constants 10×10 per square degree) in each direction if the distance from the station is less than ten degrees. The tide value on the original grid is used throughout the resolved grid. In a zone three by three degrees wide and centered on the station a land-sea distribution mask with resolution 24×24 per square degree is used which is derived from the *TerrainBase* digital topography file [*Row et al.,* 1995] with an oversampling rate of 2×2; the grid is drawn and high-resolution coastlines [*Wessel and Smith, 1996*] are superimposed on a computer screen (see Figure 4.2 as an example). In an interactive program the mask can be updated and, especially in the immediate neighborhood of the station, further refined under visual inspection. The loading mass at each grid point is obtained from bilinear interpolation of the tide height in the original grid.

Adoption of a high-resolution land-ocean mask has a consequence on the mass conservation of an ocean tide model. If the model is based on measurements only, *Schwiderski* [1980] for instance used hydrodynamic interpolation between coastal points that represented the observed tidal heights), the introduction of a coastal feature will not have an effect on tide amplitude. However, if the tide model enforces local mass conservation by employing the equation of continuity, introduction of a coastal feature will primarily preserve the tide mass in the area; the hydrodynamic conditions are altered, only as a secondary effect, which may lead to an attenuated or enhanced tidal mass flow.

In the case of mass continuity, the following means are adopted in order to conserve mass, while adjusting the land-sea distribution to realistic, high-resolution coastlines. The tidal mass that is contained in a cell of the high-resolution grid (24×24 per square degree) is redistributed among all grid cells that have the state "sea" upon a state change.

In the map method the coastline resolution of the original loading grid is invariably built in. In order to demonstrate the impact of detailed coastline representation, following variants will be distinguished,

(1) map method;
(2) the global grid's land-sea representation with interpolation on
24×24 per square degree inside 3deg ×3deg area;
(3) as (2) but with the hand-edited TerrainBase land-sea distribution;
(4) as (3) but with the island on which the site is located treated
as "sea"; (5) as (3) but with mass redistribution turned off and site box treated as land;
(6) as (3) but with mass redistribution turned off and site box treated as ocean;
(7) as (4) but with the high-resolution grid box containing the site treated as "sea";
(8) rough land-sea distribution as given by ocean tide model.

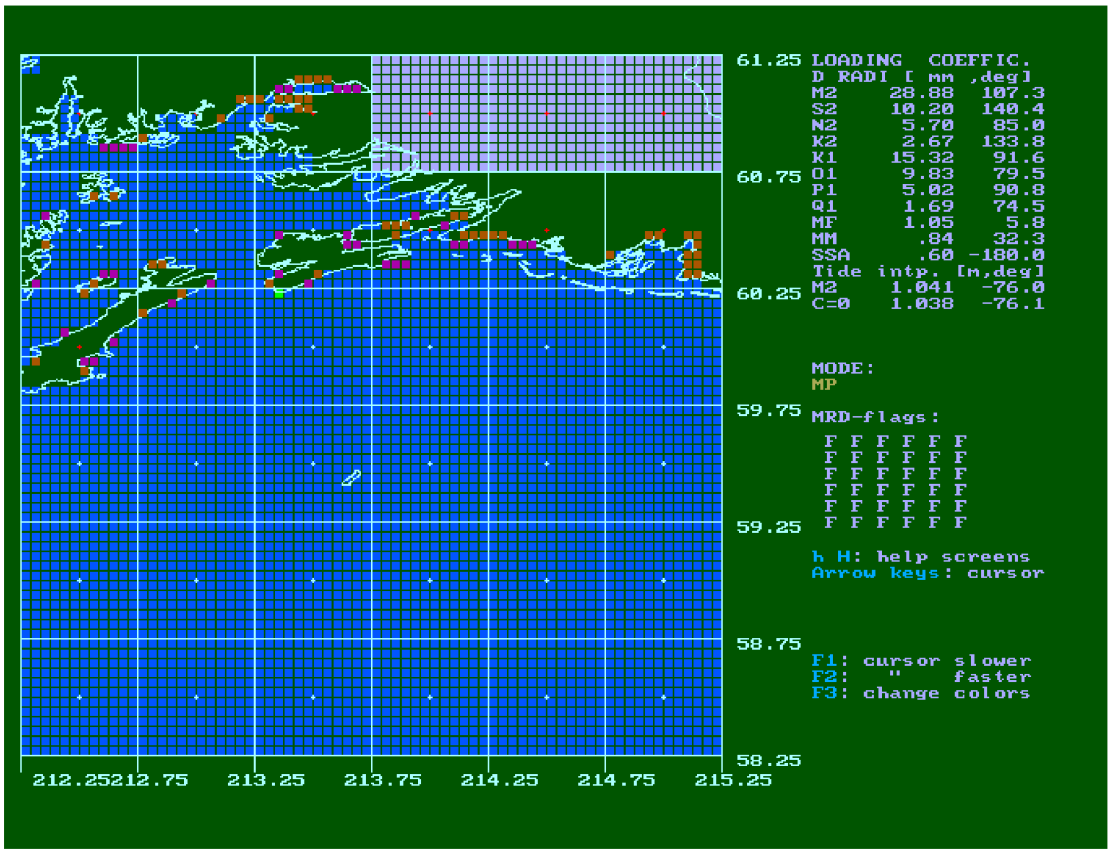

Figure 4.2: Visual interface for editing of land-sea representation. The grid cells edited in this session appear in red (state "sea" changed to "land") or purple (vice-versa). The grey boxes cannot be changed to sea since interpolation into these areas would be uncertain. The cells of the global model of state "sea" are indicated by a small white dot in the centre; in these areas interpolation of the tide is assumed safe. Those cells of the global model that are of state "land" and are neighbours to "sea" cells are indicated with a red dot in the centre; here, extrapolation of the tide is assumed possible.

4.4 Results

4.4.1 Coastal influence

In this section the GPS derived results will be compared with modeled results using different models and different coastal properties.

Predicted M_2 loading maps for vertical and horizontal displacements in Alaska are shown in Figure 4.3. The loading maps are obtained using the GOT99.2 ocean tide model [*Ray*, 1999]. Figure 4.3A shows the vertical M_2 amplitudes and Greenwich phase lags in the Alaska region. The M_2 amplitude reaches almost 42 mm in the Gulf of Alaska and about 29 mm at the GPS site, CHI3. However, the amplitude decreases significantly when crossing the coastline and has a value of only 9 mm at FAIR. This gives a relatively large differential M_2 amplitude between CHI3

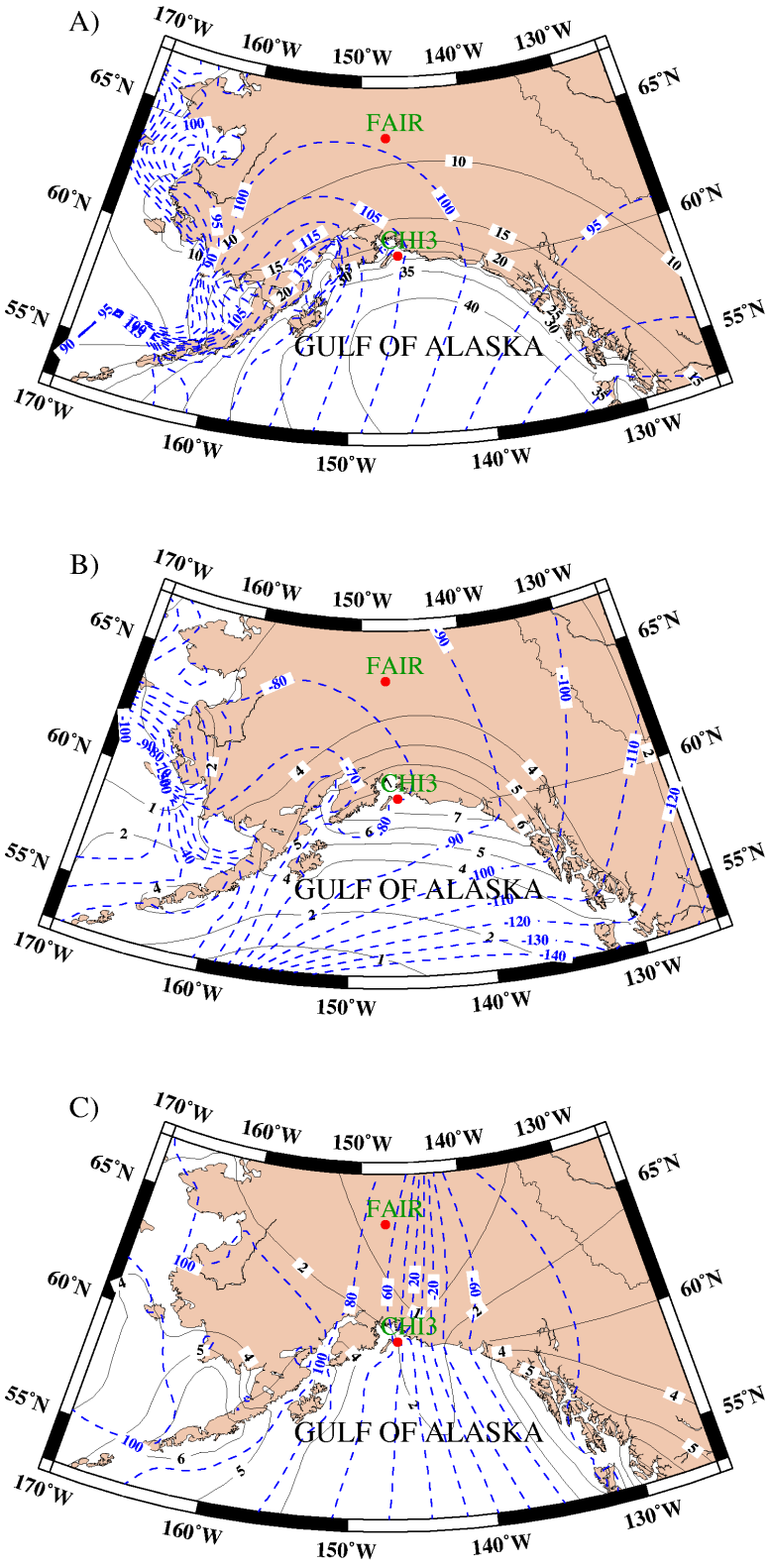

Figure 4.3: Contour maps for amplitudes and Greenwich phase lags. The solid lines display amplitude contours (in mm) and the dashed lines display phase lag contours (in degrees). The Figures display amplitudes and phase lags due to vertical (3A), north-south (3B) and east-west (3C) displacements. Amplitudes are given in mm and Greenwich phase lags in degrees. The up, north and east directions are comsidered

positive.

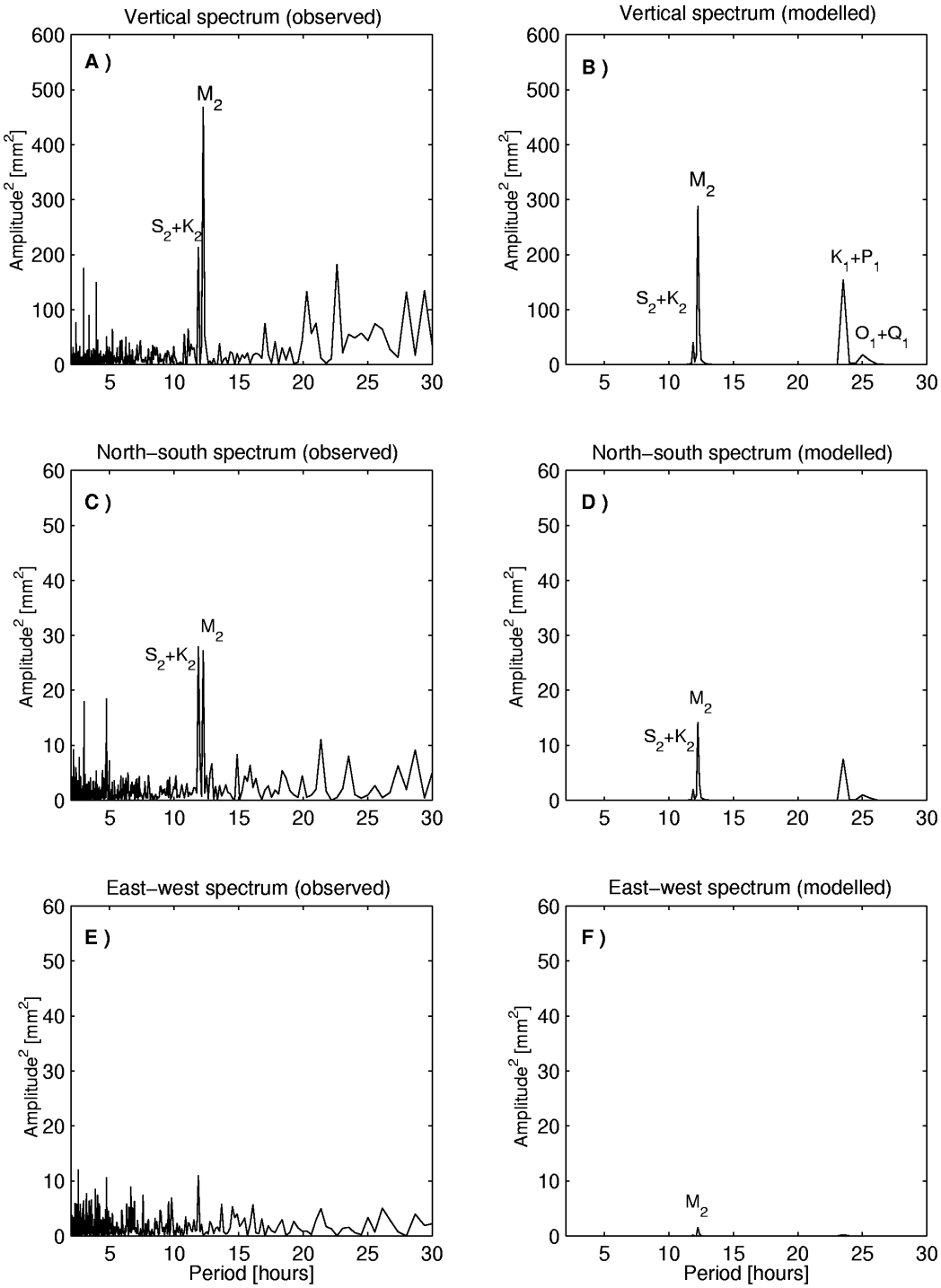

Figure 4.4: Power spectra. A) Power spectrum of relative vertical displacements based on hourly GPS solutions using strategy 1. B) Predicted power spectrum based on modeled ocean tide loading effect using the GOT99.2 ocean tide model. Similar C) displays spectrum of observed relative north-south displacements and D) displays the modeled north-south spectrum. E) displays spectra of observed relative east-west displacements and F) displays the modeled east-west spectrum.

and FAIR. The M_2 amplitudes in the north-south (NS) direction (Figure 4.3B) are much smaller than the vertical amplitudes. However, the NS amplitude in the vicinity of CHI3 is relatively large with an absolute value of almost 8 mm.

Figure 4.4A and 4.4B show the predicted and observed power spectra of hourly values of the differential vertical displacements for the baseline between FAIR and CHI3. The predicted loading power spectrum is based on the GOT99.2 ocean tide model. Both spectra show significant peaks at the M_2 period. The selected GPS-data cover only 7 weeks of observations, and we are therefore not able to separate K_2 from S_2, but have to consider these waves as one single wave '$S_2 + K_2$'. The observed spectrum (Figure 4.4A) shows a very large amplitude for the combined wave '$S_2 + K_2$', but, unfortunately the K_2 wave is affected by multipath, and the displayed peak of '$S_2 + K_2$' is not a pure loading peak. In order to obtain a reliable amplitude for the S_2 loading tide, we would need more than 6 months of continuous GPS data to separate S_2 from K_2. Regarding diurnal loading constituents, the spectra show no convincing similarities. Moreover, the tropospheric effect is large and increases the noise level. The O_1 wave is unaffected by the systematic satellite perturbations, but it has a relatively small amplitude which is below the noise level.

Figure 4.4C and 4.4D shows the observed and predicted power spectra of the differential north-south NS displacements. According to both predictions and observations, the differential NS loading effect is much larger than the east-west EW differential ocean loading effect (Figure 4.4E and 4.4F). This is caused by the natural distribution of the land and sea in the region. The observed NS power spectrum (Figure 4.4C) shows significant peaks with periods equal to the M_2, K_1 and O_1 tidal periods. Furthermore, an unexpectedly large peak appears with period equal to the K_2 tidal period. This relatively large peak is most likely generated by multipath effects or orbit errors rather than by the ocean tide loading effect. The differential EW loading effect (Figure 4.4E) is too small to be detected by DGPS and only noise and multipath are displayed. (Moreover, it should be noted that the displayed y-axis of the vertical NS and EW power spectra are not the same scale.) Hence, the vertical ocean tide loading effect (Figures 4.4A and 4.4B) is much larger than the horizontal loading effect (Figure 4.4C to 4.4F).

Predicted differential M_2 amplitudes and phase lags obtained using different global ocean tide models are listed in Table 4.2. All predicted values in Table 4.2 are calculated by including high-resolution coastline data (method "3" I Table 4.3. Moreover, our GPS results are obtained using strategy 3 (described in previous section). However, the GPS results will be discussed in more detail in the next section. The first model used is the SCHW [*Schwiderski*, 1980] and the second are two versions from the Grenoble group, FES95.2 [*Le Provost et al.*, 1994] with 0.5 deg $\times$ 0.5 deg resolution, and FES99 [*Lefvreet al.*, [2000], having 0.25 deg $\times$ 0.25 deg resolution. The FES92.2 and the FES99 model have TOPEX/POSEIDON assimilated into them (FES99 also tide gauges). The third model consistes of two versions of the Goddard tide model, GOT99.2 and GOT00.2 with 0.5 deg $\times$ 0.5 deg resolution [*Ray*, 1999], based on different lengths of TOPEX/POSEIDON altimetry. The fourth model, NAO99.b [*Matsumoto et al.*, 2000] assimilates TOPEX/POSEIDON altimetry in to a 0.5 deg $\times$ 0.5 deg resolution hydrodynamic model. Finally, the TPXO.5 model *Egbert et al.,* [1994] is a representative model that iterates the adjustment of hydrodynamic solutions to fit the TOPEX/POSEIDON altimetry.

Table 4.2: Predicted and observed (using Strategy 3) differential amplitudes and related Greenwich phase lags of the M_2 ocean tidal loading constituent. The autmoatic ocean loading provider was used with the models that are desginated with an a) in the second column.

		Diff. vertical M_2 disp.		Diff. north-south M_2 disp.	
Model	Remark	Amplitude	Phase lag	Amplitude	Phase lag
		[mm]	[deg.]	[mm]	[deg.]
SCHW		20.5	110.0	4.2	-78.6
FES95.2		17.9	112.6	4.1	-79.2
FES99	a)	22.0	114.4	4.8	-78.4
GOT99.2		19.3	110.2	4.5	-77.0
GOT99.2	a)	19.7	111.0	4.5	-80.1
GOT00.2	a)	20.2	111.3	4.4	-78.9
NAO99.b	a)	23.3	114.0	4.5	-78.7
TPXO.5	a)	23.6	112.2	4.5	-73.3
GPS obs.		21.3 ± 1.0	99.7 ± 2.8	5.4 ± 0.3	-106.3 ± 3.3

The loading results from the models FES99, GOT00.2, NAO99.b, and TPXO.5 have been computed with the automatic loading provider available at:
http://www.oso.chalmers.se/∼loading.
The method employed to resolve the coast uses the high-resolution coastlines from the Generic Mapping Tool package [*Wessel and Smith*, 1996]. In order to compare the two coastline methods, the loading effects from GOT99.2 is recomputed with the automatic loading provider, labeled GOT99.2 a) in Table 4.2. The coastline treatment employed by all modeling methods in Table 4.2 except the map method corresponds to variant (4), i.e. high resolution, no mass redistribution, and site-box treated as land. The automatic loading provider is able to go to higher geographical detail, but in all other respects the loading algorithm is always identical [*Scherneck and Bos*, 2002].

The model predictions are shown in Table 4.2. They appear to disagree at the 30 percent level, with FES95.2 at the lower end (17.9 mm) of the amplitude range and TPXO.5 at the upper (23.6 mm). The phase disagreement is bracketed in a 6deg interval, which implies a narrower scatter than in the amplitude case. Compared with our GPS observations, the amplitude (21.3 ± 1.0 mm) is seen to agree with the models at slightly above mid range, whereas the observed phase (99.7 ± 2.8deg appears to be low with respect to all models. The agreement for the horizontal M_2 loading effect is less good. In particular the predicted M_2 phase lags deviate by almost 30 degrees from the observed phase lag. Moreover, the amplitude range with FES95.2 at the lower end (4.1 mm) and FES99 at the upper end (4.8 mm), while our GPS observations gives 5.4 ± 0.3 mm. Table 4.3 displays the predicted differential vertical and horizontal M_2 amplitudes and phase lags. The predictions are based on the map method and the convolution method as described in the previous section (see no. 1 to 8 in Table 4.3). However, the map method (no. 1) shows the best agreements with the GPS results. Moreover, the map method gives a differential vertical amplitude of 22.4 mm, which is close to the observed value of 21.2 mm (using strategy 3). This excellent agreement in a difficult location should not be considered representative of the map method in general. However, a systematic comparison has still to be made. In method no. 5 and 6 the MRD

option is selected

Table 4.3: Predicted differential amplitudes and related Greenwich phase lags of the M_2 ocean tide loading constituent. The GOT99.2 ocean tide is used.

		Diff. vertical M_2		Diff. north-south M_2	
	Method	Ampl. [mm]	Phase lag [deg.]	Ampl. [mm]	Phase lag [deg.]
1	Map method	22.4	109.1	4.4	-78.0
2	High-resolution coastline data standard method	19.4	111.4	4.5	-79.2
3	High-resolution coastline data hand edited coastline	19.3	110.2	4.5	-77.0
4	High-resolution coastline data island and site treated as sea	20.8	111.2	4.1	-80.3
5	MRD-option = off site box is land	20.1	110.7	4.6	-78.0
6	MRD-option = off site box is ocean	20.5	110.1	4.6	-78.0
7	High-resolution coastline data island treated as sea	20.3	110.8	4.6	-80.3
8	Rough land-sea distribution as given by ocean tide model	20.9	111.6	4.3	-80.6

"off". The MRD option stands for Mass ReDistribution and implies that tide mass of an ocean tide model is redistributed in the zone in which coastline refinement is considered. When the coastline suggests that the state of a load box a quadrangle of size 1/24 x 1/24 deg must be changed from land to sea, the tide mass must either be redistributed or removed. Redistribution is indicated if the particular ocean tide model enforces mass conservation at the coast (most hydrodynamic models do, all hydrodynamic models that do not assimilate data do). Removal is indicated if ocean tide model is strongly constrained by coastal tide observations (as in *Schwiderski* [1980]). Opening a new sea box, the reverse occurs: Under MRD the extra mass is collected from the refinement area, else mass is created. For this reason, coastline refinement under the MRD scheme causes less impact on loading effects than without MRD.

The influence of the near-grid resolution and coastal properties are demonstrated using the convolution method (no. 2 to 8). When using the coarse grid resolution of $0.5^\circ \times 0.5^\circ$ (no. 8), a differential vertical M_2 amplitude of 20.9 mm is obtained. In this case, the island is small; hence the box where the site is located is treated as sea, which gives the relatively large loading effect. However, when including the high-resolution coastline data and a higher grid resolution for the nearby area while still treating the island as sea (no. 4), an amplitude of 20.8 mm is obtained. If now the island is treaded as land and the high grid resolution (no. 3) is used, then an amplitude of 19.3 mm is obtained. This shows that it is important to calculate the near-field effect using a high grid resolution that allow for a high-resolution coastline). Even though the differential vertical M_2 amplitude calculated using the coarse grid resolution fits the GPS results better than the one calculated with the fine grid resolution, it cannot be concluded that it is better to use the coarse grid

resolution than the fine grid resolution, because the accuracy of the ocean tide model is not taken the into consideration. Moreover, we know that ocean tide models are far from perfect near coastal areas. Hence, using a different ocean tide model, but the same coastal properties as in Table 4.3 (no. 2 to 8), we may obtain results in favor of the fine grid resolution.

4.4.2 Tropospheric influence

Now, the tropospheric influence on ocean loading estimation will be considered. Figure 4.5A shows the power spectrum of the hourly differential GPS solution obtained using Strategy 1. Figure 4.5B shows a similar power spectrum, but the GPS solutions are obtained using Strategy 2. The absorption of the tropospheric signal into the ocean tide loading signal is seen by comparing Figure 4.5 and Figure 4.6 (A and B). Figure 4.6A and 4.6B show power spectra of the hourly ZTD derived from hourly and daily GPS solutions, respectively. Figure 4.6B (1-h estimate derived from 24-h GPS solutions) show significant peaks with periods equal to the M2 and S2 tidal constituents. This indicates that the ocean tide loading effect may have been absorbed into the ZTD parameters obtained using strategy 2. However, Figure 4.6A (1-h estimate derived from 1-h GPS solutions) show significant peaks with periods equal to the S2 tidal constituents only. No significant peak with a period equal to M2 is seen. In order to clearly demonstrate which processing strategy absorba ocean loading into ZTD estimates, the differential M2 amplitude and phase lags of the vertical displacements (Table 4.4) and ZTD parameters (Table 4.5) are calculated. Strategy 2 absorbs ocean loading into ZTD estimates. This is obvious when the phase lag of the M2 differential vertical displacements derived from Strategy 1 (Table 4.4) is compared with the M2 phase lag of the 1-h ZTD estimations (Strategy 2 from Table 4.5). The phase lags being almost the same, 102.85 and 105.49, respectively, shows that loading is absorbed into ZTD. However, the phase lags of the 1-h ZTD estimations (Strategy 3 from Table 4.5) not being the same as using strategy 1 (Table 4.4), show that ocean loading is NOT absorbed into ZTD estimation for Strategy 3.

The power spectrum of the hourly ZTD derived from hourly GPS solutions (Figure 4.6A) show peaks at periods of 12, 8, 6, 4.8, 4 . . . hours. It is suspected that they are artifacts resulting from the characteristics of the GPS processing rather than being caused by real geophysical phenomena. For example *Rothacher et al.* [2001] have found similar perturbations, which they attribute to periodic orbital errors at integer fractions of the orbital period. However, the peak at 12-h period may be an artifact also, but it could also be caused by multipath or satellite orbit error.

Despite the large spectral peaks at frequencies different from the M2, this solution strategy is superior to the others. First of all, the M2 effect in the 24h ZTD estimates is slightly larger than in the 1h estimates. Second a reasonable criterion for tidal loading must take only the M2 motion into account, since S2 and K2 and other waves are of nonlunar origin, and these are likely to affect the satellite range with very different spatial signatures than those induced by the tidal motion of the stations. The time series are long enough so that anomalous effects at S2 do not perturb the signal at M2 noticeably.

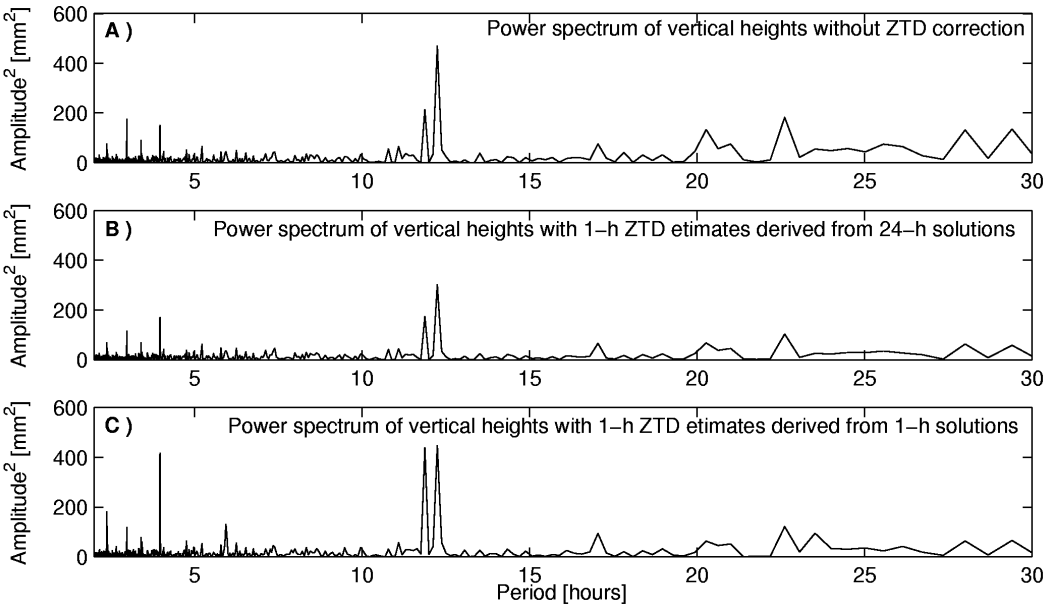

Figure 4.5: Power spectra of the relative vertical displacements derived using A) strategy 1 B) strategy 2 and C) strategy 3. The various strategies are described in the text.

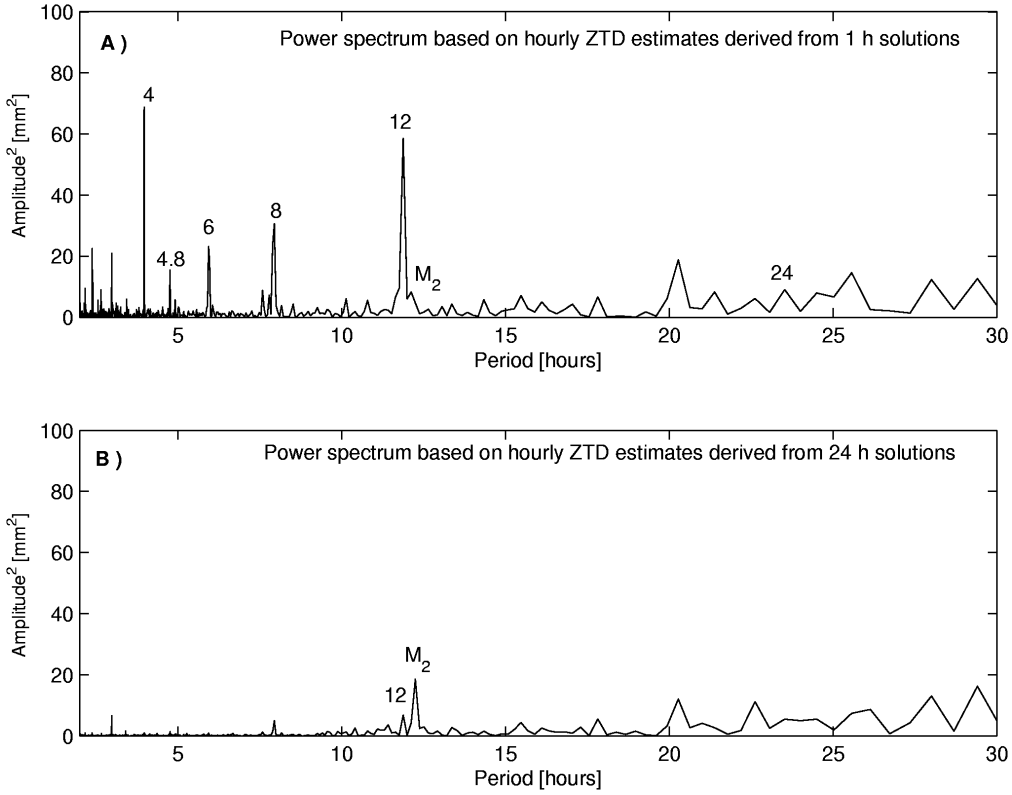

Figure 4.6: A) Power spectrum of the hourly ZTD estimates derived from hourly GPS solutions. B) Power spectrum of the hourly ZTD estimates derived from 24 h GPS solutions.

Table 4.4: The differential amplitudes and Greenwich phase lag of the M2 ocean tide loading constituent due to vertical displacements.

Strategy	Amplitude mm	Greenwich phase lag deg.
Strategy 1 (without ZTD)	22.4 ± 0.4	102.9 ± 1.0
Strategy 2 (with 1-h ZTD derived from 24-h solution)	17.6 ± 0.4	102.1 ± 1.1
Strategy 3 (with 1-h ZTD derived from 1-h solution)	21.3 ± 1.0	99.7 ± 2.8

Table 4.5: The M2 differential amplitudes and Greenwich phase lags of the hourly estimated ZTD parameters derived from hourly and daily GPS solutions, respectively.

Strategy	Amplitude mm	Greenwich phase lag deg.
1-h ZTD estimated using Strategy 2	4.9 ± 0.2	105.5 ± 2.2
1-h ZTD estimated using strategy 3	1.6 ± 0.7	149.6 ± 25.2

An a priori error is computed on the basis of a standard assumption made of precision of phase measurement in receivers. This front-end uncertainty is carried through the data analysis of the Bernese GPS data processing program, disregarding eventual problems like multi-path. The temporal correlation can be judged from the power spectrum and the associated autocovariance series. Table 4.6 column 2 displays the standard deviation derived from the hourly GPS solutions. Column 3 and 4 display the noise at the tide-free frequencies at each side of the M_2 tidal peak.

The noise colour is found to be red (i.e. the noise spectrum to be low-frequency dominated). The slope, however, appears to level out at roughly one period per day. Thus, the precision at 12 hour is somewhat lower than what is obtained assuming independent estimates. In the last column in Table 4.6 is listed the ratios between the mean standard deviation derived from power spectrum and standard deviations derived from the GPS software. Moreover, the mean value of the ratio is 3.4 ± 0.5. Thus, the actual error of the BERNESE software is suspected to be 3.4 times larger than the error given in the hourly solutions.

Table 4.6: The table shows the differential M2 amplitudes and standard deviation. However, the standard deviation are derived from GPS (Column 2) and power spectra (Columns 3 and 4). Furthermore, the last column shows the ratio between the standard deviation derived from power spectrum and GPS.

ps = power spectrum	std = standard deviation				
Observation	Amp. mm	std GPS	std ps (left)	std ps (right)	Ratio $\frac{mean[ps]}{[GPS]}$
Strategy 1 (without ZTD)	22.4	0.4	1.7	1.1	3.5
Strategy 2 (with 1-h ZTD derived from 24-h solution)	17.6	0.4	1.6	1.4	4.2
Strategy 3 (with 1-h ZTD derived from 1-h solution)	21.3	1.0	3.3	2.8	3.0
1-h ZTD estimated using Strategy 2	4.9	0.2	0.4	1.0	3.9
1-h ZTD estimated using strategy 3	1.6	0.7	2.5	1.3	2.8
Horizontal (north-south) M2 wave	5.4	0.3	0.8	1.1	3.1

4.5 Conclusion

This case study demonstrates that the M_2 ocean tide loading wave for vertical and horizontal displacements is measurable by DGPS. Although only the M_2 loading wave is considered here, the main waves S_2, N_2, O_1, Q_1 and P_1 can be detected using GPS. Meanwhile, K_1 and K_2 have to be considered carefully. Multipath and satellite orbit errors must be eliminated. In order to obtain accurate amplitude and phase lags of the main constituents, continuous GPS for a period longer than 6 months is required.

Surface displacements due to ocean tidal loading can be well resolved in the analysis of GPS data using Strategy 3 (estimation of 1-h ZTD derived from 1-h solutions). It is possible to separate the ocean tidal loading and tropospheric effects very well. Indeed, no ocean loading is absorbed into the ZTD parameters using Strategy 3. However, when Strategy 2 (estimation of 1-h ZTD derived from 24-h solutions) is used, loading is absorbed into the tropospheric modeling. More precisely, 23 percent of the M2 ocean tide loading amplitude is absorbed into the zenith delay amplitude at the M2 frequency. *Dragert et al.* [2000] have obtained similar results, however they use 3-hour intervals instead of 1-h intervals.

A number of options are discussed that address problems of actual coastline interaction with gridded ocean tide model data. A global map method based on spherical harmonics seems to differ from the rest of the predictions, which are based on space-domain convolution integrals. Our results point towards somewhat larger variation due to different models than due to different coastline options. Using the coast as resolved by the original model grid has been found to change the

prediction by 4 percent compared to using a five-minute topographic database. Further resolution probably does not improve the predictions significantly.

GPS analysis of observations with the uncertainties and duration in the present work, 3 mm and 6 weeks, is able to discriminate between the different tidal models. Improved coastline resolution appears to be a slightly smaller problem that is likely to become increasingly significant when the time series duration is longer, 0.5 year to one year.

Concerning the load Love numbers, we normally use one set of Love numbers for oceanic crust and another set for continental crust. Moreover, the loading effect has local dependencies and the selected GPS-site CHI3 is located at a subduction zone, where the average crust-structure and thickness is not a good approximation. Hence, we might have to use a more realistic crustal thickness than the one used in this study.

The differential ocean tide loading effect near the coastline of southern Alaska is huge. However, the differential loading effect is more than twice the size of the corresponding differential solid Earth tide effect. This is not a unique case; in addition, the differential ocean loading is found to be larger than the differential solid Earth tide effect is obtainable for several near-coast regions worldwide e.g. southern England, Bay of Hudson and southern Africa.

The power spectrum of the hourly ZTD derived from hourly GPS solutions (Figure 4.6A) shows peaks at periods of 12, 8, 6, 4.8, 4 hours etc. It is suspected that they are artifacts resulting from the characteristics of the GPS processing. For example [*Rothacher et. al.*, 2001] have found similar perturbations, which they attribute to periodic orbital errors at integer fractions of the orbital period. However, since the semi-diurnal and diurnal ocean tides are relatively large in Alaska, the non-linear tides may cause vertical surface deformations of the order of millimeters in the third- diurnal, quarter-diurnal and fifth-diurnal tidal band.

Additionally, the peak at 12-h period may be caused by multipath or satellite orbit error. Moreover, when using Strategy 2 (1-h ZTD derived from 24 h solutions), we probably add 24-h and also 12-h periods to the time series. This can be avoided e.g. by using 28-h windows instead of 24-h windows. Using 28-h windows, the data are supposed to overlap by 2-h at each side of the day. This will also improve the ZTD modeling. Furthermore, ambiguities were solved using 24-h windows, again, it is better to have overlap between the windows to reduce or eliminate artifact signals.

Chapter 5

Shallow-water loading tides in Japan from SG

5.1 Motivation

The indirect deformations of the Earth caused by variations in the surface load from tides are known as ocean tide loading (OTL) deformations, and are detectable by measuring surface displacements, tilt and gravity changes. To predict the OTL effect, an ocean tide model (describing the spatial and temporal distribution of the surface load) and a elastic Earth model (describing how the Earth responds to the surface load) are needed. The ongoing satellite altimetric missions have improved global ocean tide models considerably to obtain accuracies of 2-3 cm in the deep oceans. However, these global ocean tide models still show poor accuracy in continental shelf regions [*Andersen*, 1999].

Several studies have pointed out the significance of the OTL effect on gravity measurements. The OTL influences on gravity measurements have been considered by, e.g., *Baker and Bos* [2001], *Jentzsch et al.* [2000] and *Mukai et al.* [2001]. All these investigations have focused on the main diurnal and semi-diurnal tidal waves (Q_1, O_1, P_1, K_1, N_2, M_2, S_2 and K_2). Modeled and observed loading amplitudes are consistent within 10 % and the deviations between modeled and observed phases are 10 degrees for most parts of the main waves [*Mukai et al.*, 2001].

In contrast to GPS positioning, gravity measurements are not sensitive to for tropospheric effects but are sensitive to total atmospheric pressure. Thus, they are a much better source for OTL analysis and may be used for detection of tidal signals with very small amplitudes. This advantage is utilized by *Merriam* [1995], who showed that shallow-water loading tides are detectable with a superconducting gravimeter. *Merriam* [1995] also compared his results with tide gauge observations from St John, New Brunswick, Canada, showing consistency between the two sets of data.

The purpose of this case study is to detect the shallow-water loading effects at two different superconducting gravity sites in Japan: Esashi and Matsushiro (see Figure 5.1 and Table 5.1). One is located relatively close to the east coast and the other is close to the west coast. To compare these gravity observations with tide gauges, several tide gauge sites have been selected located on the east and west coasts of Japan (se Figure 5.1). Hence, we are able to broadly locate the 'sources' of the observed shallow water loading tides.

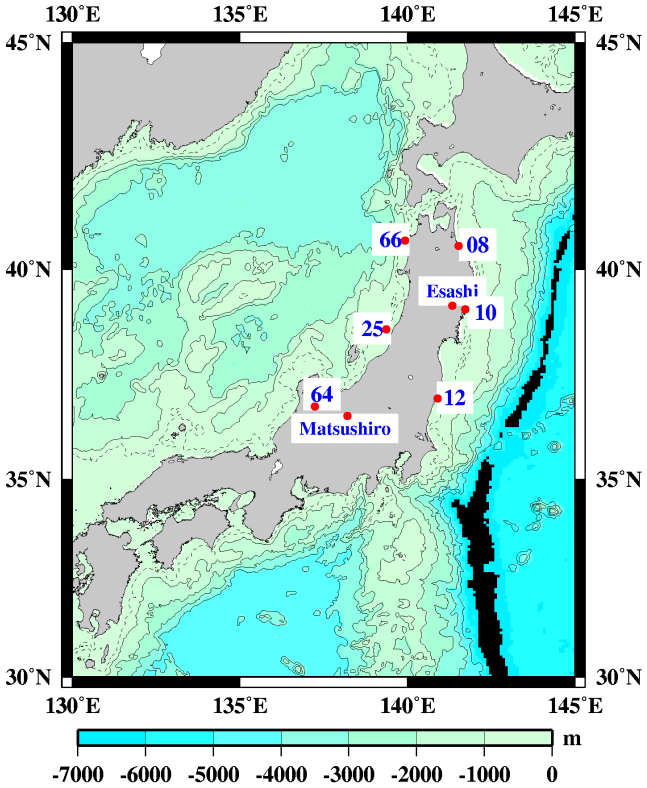

Figure 5.1: Location of the selected gravity sites (Matsushiro and Esashi) and the tide gauges (08, 10, 12, 66, 25 and 64).

Table 5.1: Coordinates for the selected gravity stations and their distance to the east coast.

Station name	Latitude [deg.]	Longitude [deg]	Height [m]	Distance to east coast [km]
Matsushiro	36.5439	138.2032	451	223 km
Esashi	39.1511	141.3318	434	33 km

5.2 Theory

Shallow-water tides are overtides and compound tides of the astronomical components and appear within the diurnal, semi-diurnal, third-diurnal, quarter-diurnal, and even higher, constituent bands. The shallow water momentum and conservation equations are given by e.g. *Gill* [1982],

$$\frac{\partial \vec{v}}{\partial t} + \vec{v} \cdot \nabla \vec{v} = -\vec{g}\nabla\eta - \vec{g}\vec{k} - f\vec{k} \times \vec{v} - \mu|v|\vec{v} \tag{5.1}$$

$$\frac{\partial \eta}{\partial t} = -\nabla \cdot (D\vec{v}) \tag{5.2}$$

where t is time, $\vec{v}$ is the velocity vector, η is the deflection of the free water surface from some reference height, and D is the total water depth. Furthermore, $\vec{g}$ is the gravity vector, μ is the water friction parameter of the basin, f is the Coriolis parameter and $\vec{k}$ is the vertical unit vector. The non-linearities in equation 5.1 and 5.2 are introduced through the spatial advection term $(\vec{v}\cdot\nabla\vec{v})$, the friction term $(\mu|v|\vec{v})$ and the continuity term $(\nabla\cdot(D\vec{v}))$. These terms cause modulation and distortion of the astronomical tidal constituents, which can be described as combinations of the original constituents. In contrast to the linear tidal constituents, the shallow water tides can have frequencies which are not found in the tide-generating potential. In general, the continuity and advection terms generate shallow water constituents from an even number of astronomical constituents (e.g., M_4 from $2\omega_{M2}$), whereas the friction term generates odd harmonics (e.g. M_6 from $3\omega_{M2}$) [*Le Provost*, 1991], where ω is the angular velocity of the Earth's rotation.

The total OTL effect depends upon the spatial distribution of the surface mass load. However, the spatial distribution of the load can be described by the wavelength of the tidal wave, λ. This is related to the water depth D and the period of the waves through [*Pugh*, 1987],

$$\lambda = cP = (gD)^{1/2}P, \tag{5.3}$$

where g is the magnitude of gravity, and P is the period of the waves. Shallow-water overtones will thus have wavelengths smaller than the semi-diurnal and diurnal astronomical constituents. From equation 5.3, quarter-diurnal tides at 50 m depth have a wavelength of 490 km and sexto-diurnal of 325 km, compared to a diurnal wavelength of 1950 km at the same water depth. Hence, near the coasts, where the water depth is relatively small, the wavelength of the shallow- water overtones becomes small. This means that we need a high-resolution tide model to correctly model the loading effect in the area.

5.3 Data Analysis

The superconducting gravity data used were taken from the Japanese stations Esashi and Matsushiro (Table 5.1 and Figure 5.1), where the non-linear tidal constituents are generated in the shallow waters on the Japanese shelf. The moderate shelf offshore Japan may not provide the optimal conditions in terms of studying shallow-water tides, but was chosen for this study as observations of both sea level and gravity are available. An optimal area is one where the diurnal and semi-diurnal ocean tides have large amplitudes and the continental shelf covers a large area (e.g., the North Sea).

Superconducting gravimeters (SG) are able to measure relative gravity variations with very high precision. The sensitivity of these instruments is close to 0.01 nm/s^2 at tidal and normal mode frequencies [*Meurers*, 2001]. Consequently, we are able to observe gravity variations caused by effects such as the loading effect due to shallow water tides, which have relatively small amplitudes.

For Esashi, data collected during the period from 5 July 1997 to 31 December 1999 is used, and for Matsushiro data collected from 23 April 1998 to 31 December 2000 is used. The raw data were sampled every second and decimated (not averaged) to hourly values, which were used for the final processing. To correct for

the atmospheric effect, pressure data were observed for both sites and air pressure correction were applied using complex admittance [*Merriam*, 1995]. In order to correct for the solid Earth tide effect we use latitude-dependent parameters from the [*Wahr*, 1981] [*Dehant*, 1987] [*Dehant and Zschau*, 1989]. The solid Earth tide effect is believed to be modeled very well [*Merriam*, 1995]. Hence, adding solid Earth tide correction, pressure correction, and drift correction to the raw gravity observations leaves us with a residual signal, which is assumed to be dominated by the ocean loading signal. Ocean tide loading near 1 and 2 cycles per day (cpd) in Japan is considered in several other studies, e.g. *Mukai et al.* [2001], hence only the spectrum from 3 to 6 cpd will be considered here. The amplitudes and phase lags of the shallow water loading signal are then obtained by fitting cosine functions to the residual signal using the least squares method.

Hourly tide-gauge observations from January 1, 1995 to December 31, 2001 were obtained from the 'Hydrographic and Oceanographic Department, Japan Coast Guard', 'Japan Meteorological Agency' and 'Hokkaido Development Agency'. three tide gauge sites on the Japanese east coast and three on the west coast (Figure 5.1) were selected. Amplitudes and phase lags of the oceanic tides were calculated by fitting cosine functions to the sea level observations.

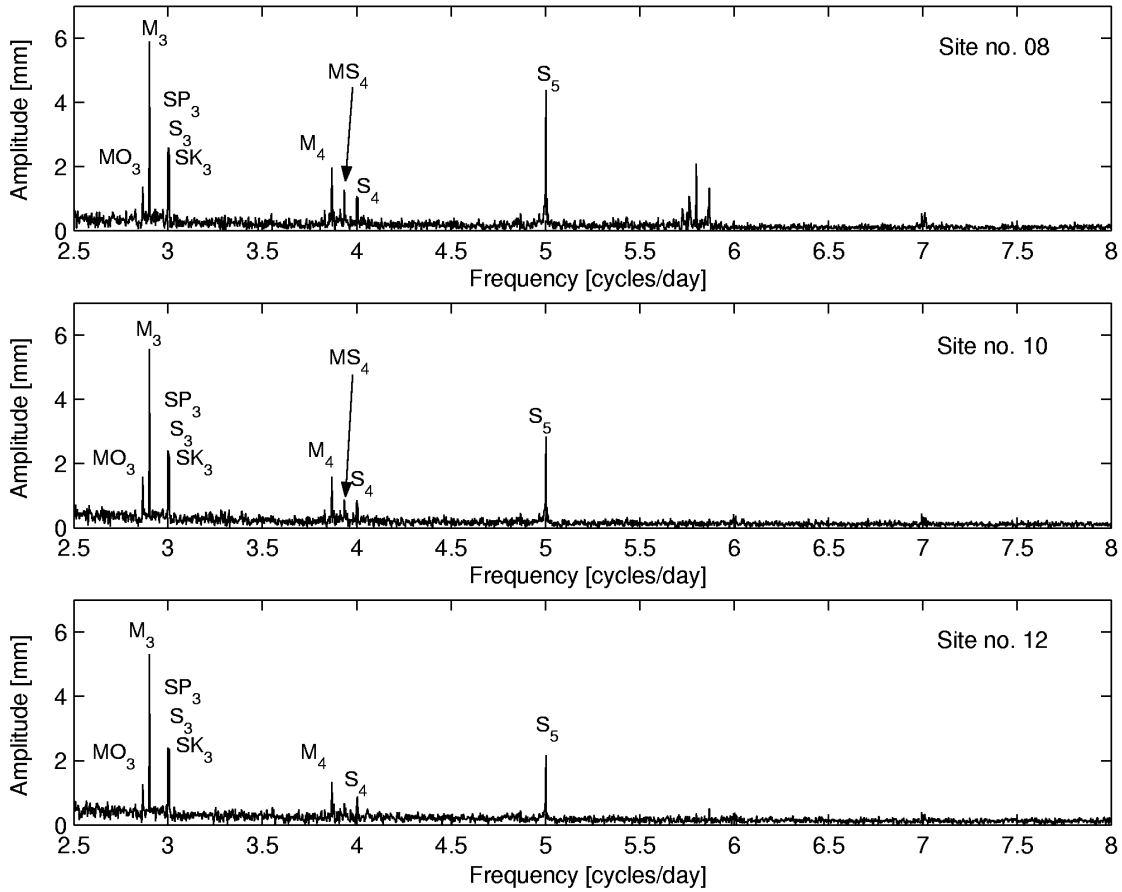

Figure 5.2: Amplitude spectra of the tide gauge data at the Japanese east coast (site no. 08, 10 and 12). The frequency is given in cpd (cycles per day), and the amplitude is given in mm.

Figure 5.2 displays the amplitude spectra of the sea level observations from the tide gauge sites on the Japanese east coast. Significant peaks are seen at the third, fourth, fifth and sixth diurnal tidal frequency bands due to shallow water tides. Site no. 8 shows the largest amplitudes for the solar waves S_3, S_4 and S_5, whereas site no. 12 shows the smallest amplitudes. Only one peak is visible in Figure 5.2 at 3 cpd (corresponding to the S_3 wave), but the graph consists of three peaks at the tidal constituents: SP_3, S_3 and SK_3. To resolve adjacent frequencies, the Rayleigh sampling criterion requires a minimum record length of $T = 1/(\omega_1 - \omega_2)$. According to this, the three tidal frequencies are resolvable in records longer than one year, which is fulfilled with all data records used here, since more than two years of continuous data is used here. Figure 5.3 is an enlargement of site no. 8 in Figure 5.2 (top) at the ter-diurnal (three times daily) band. Figure 5.3 shows that the three solar constituents near 3 cpd are resolved very well.

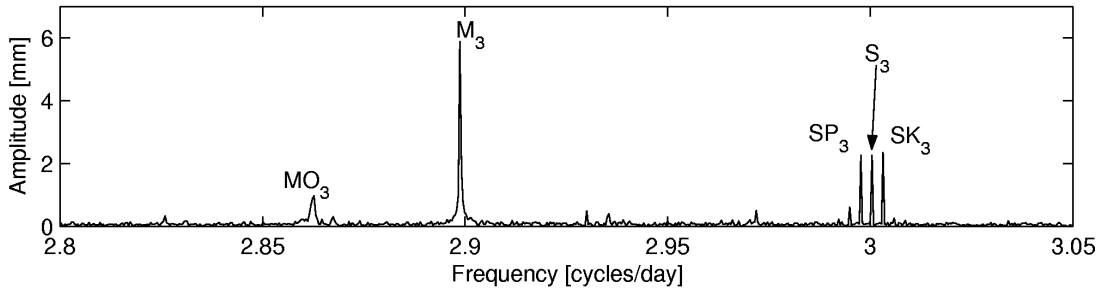

Figure 5.3: Amplitude spectra of the tide gauge data from station no 8. The figure is an enlargement of Figure 5.2 (top) at the terdiurnal band and shows that the three solar waves, SP_3 S_3 and SK_3 are well resolved.

Figure 5.4 displays amplitude spectra of the sea level observations from the tide gauge sites at the Japanese west coast. The northern site (no. 66) shows almost no significant shallow water tides, while the southern site (no. 64) shows some moderate peaks. In contrast to the east coast, the west coast shows no significant peaks for the S_3, S_4 or S_5 solar waves. In general, the shallow water tides at the west coast are very small compared to the east coast. This is probably related to the amplitudes of the diurnal and semi-diurnal constituents, which are 3 to 7 times larger at the east coast compared to the west coast.

Figure 5.5 displays amplitude spectra of the observed SG gravity data. The largest peaks appear at Esashi (Figure 5.5, top), which is the site closest to the east coast. The spectrum for Esashi shows significant loading peaks at frequencies equal to the shallow water tidal peaks at the east coast (cf. Figure 5.2). In addition, the spectrum for Esashi is very similar to the tide gauge spectrum of site no. 10 (Figure 5.2, middle). All three solar waves S_3, S_4 and S_5 occur with significant peaks in the gravity amplitude spectrum for Esashi.

The amplitude spectra of the observed gravity at Matsushiro (Figure 5.5, bottom) display significant peaks with the same frequencies as those peaks observed at Esashi, but with smaller shallow water loading amplitude. All three solar waves S_3, S_4 and S_5 are significant at Matsushiro. There are no S_3, S_4 or S_5 shallow water tides at the west coast of Japan, and we expect that the observed S_3, S_4 and S_5 shallow water loading waves at Matsushiro and Esashi are generated from

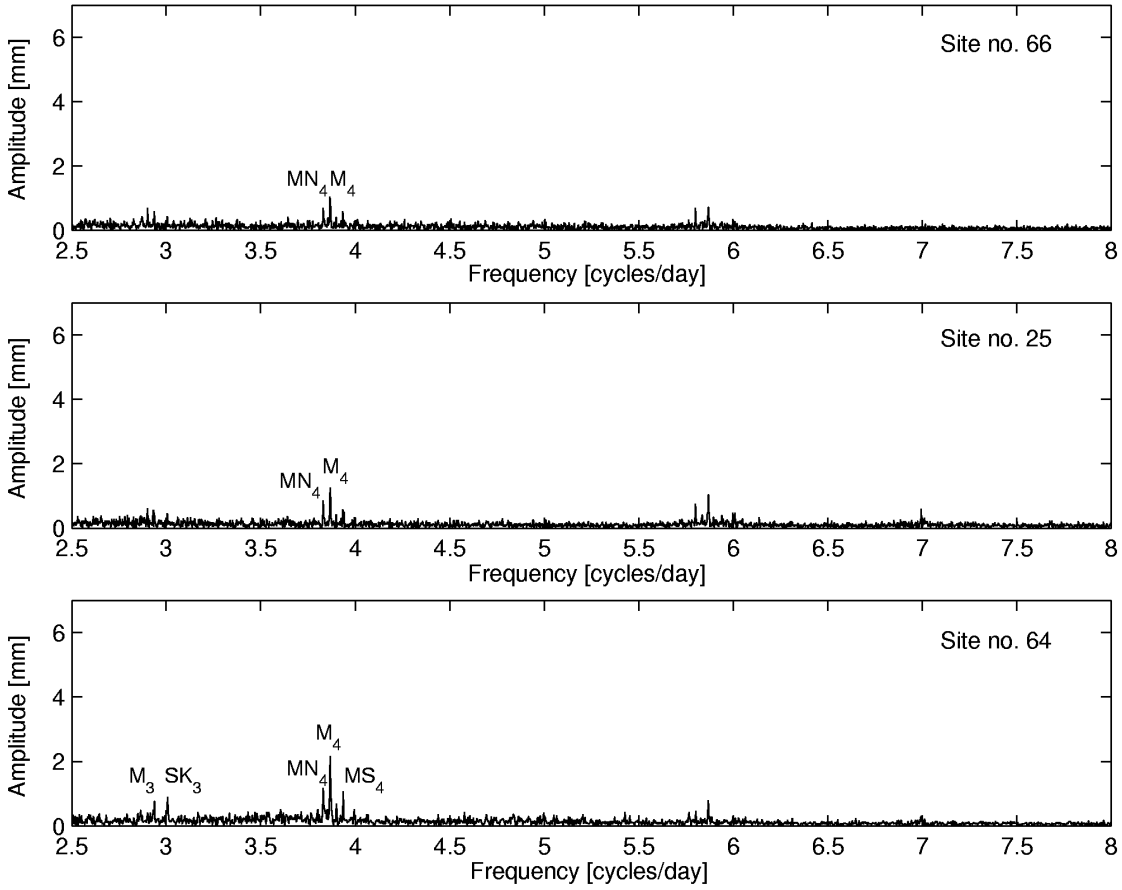

Figure 5.4: Amplitude spectra of the tide gauge data at the Japanese west coast (site no. 66, 25 and 64). The frequency is given in cpd, and the amplitude is given in mm.

tides at the Japanese east coast. This is seen from Tables 5.2 and 5.3 by comparing the phase lags of the gravity and the tide gauge tidal waves. Table 5.2 lists the amplitudes and phase lags of the tide gauge waves from all six stations. However, the waves SP_3, S_3, $3SP_4$, S_4 and S_5 are not significant at the west coast stations (marked with 'n.s.' in Table 5.2). Table 5.3 lists the amplitudes and phase lags of the shallow-water loading waves. Tables 5.2 and 5.3 show that the observed S_3 shallow water tidal waves at the east coast and the observed S_3 shallow water loading waves at Esashi and Matsushiro have phase lags which are consistent within 20-25 degrees. Similarly, the observed shallow water tidal waves S_4 and S_5 at the east coast are consistent with the observed shallow water loading waves within 20-30 degrees. Thus, the S_3, S_4 and S_5 shallow water loading signal observed at Matsushiro is generated from the east coast, even though the site is located closer to the west coast. Similarly the observed SK_3 and SP_3 loading waves are also generated from oceanic tides at the Japanese east coast.

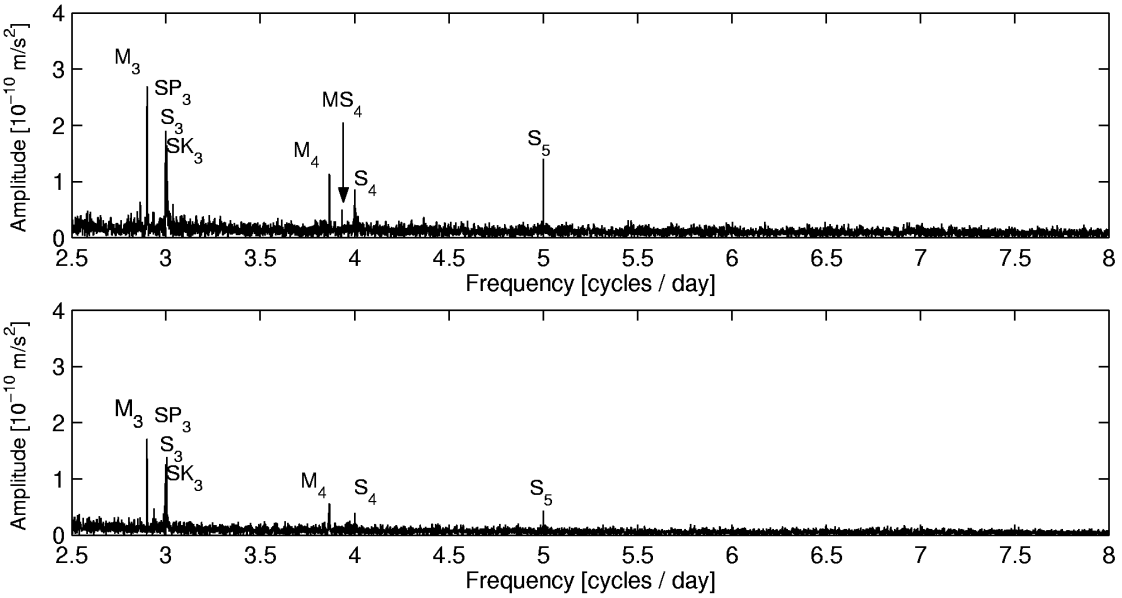

Figure 5.5: Amplitude spectra of the gravity data for Esashi (top) and Matsushiro (bottom). The frequency is given in cpd, and the amplitude is given in $10^{-10}m/s^2$.

Table 5.2: Amplitudes and phase lags of the shallow water waves at the tide gauge stations. The amplitudes are given in mm and the 1σ formal error obtained from the least square fit is 0.35 mm.

		Station no. 8		Station no. 10		Station no. 12	
Wave	Freq.	Amp.	Phase	Amp.	Phase	Amp.	Phase
	deg/h	mm	deg	mm	deg	mm	deg
M_3	43.4762	6.18	37.6	5.65	1.5	5.45	31.0
SP_3	44.9590	2.24	48.3	2.19	40.6	1.94	43.4
S_3	45.0000	2.26	109.8	2.13	108.3	2.03	108.8
SK_3	45.0411	2.33	55.6	1.99	63.1	2.06	56.1
M_4	57.9682	2.35	311.3	1.64	278.8	1.49	326.0
MS_4	58.9841	1.71	19.4	0.96	353.1	0.85	10.3
$3SP_4$	59.9590	1.38	227.5	0.98	226.3	0.98	217.0
S_4	60.0000	1.01	269.5	0.80	295.8	0.85	282.0
S_5	75.0000	4.14	350.9	2.80	349.8	2.01	343.1

table 5.2 continued

		Station no. 66		Station no. 25		Station no. 64	
Wave	Freq. deg/h	Amp. mm	Phase deg.	Amp. mm	Phase deg	Amp. mm	Phase deg
M_3	43.4762	0.86	295.7	0.70	300.3	0.42	309.5
SP_3	44.9590	n.s.	-	n.s.	-	n.s.	-
S_3	45.0000	n.s.	-	n.s.	-	n.s.	-
SK_3	45.0411	n.s.	-	0.40	95.8	0.46	137.1
M_4	57.9682	0.80	277.3	1.49	283.5	1.65	289.2
MS_4	58.9841	0.40	161.5	0.60	148.8	0.70	138.2
$3SP_4$	59.9590	n.s.	-	n.s.	-	n.s.	-
S_4	60.0000	n.s.	-	n.s.	-	n.s.	-
S_5	75.0000	n.s.	-	n.s.	-	n.s.	-

Table 5.3: Amplitudes and phase lags of the shallow water loading waves at Esashi and Matsushiro. The amplitudes are given in nanogal and the 1σ formal error obtained from the least square fit is 0.12 ngal on the amplitudes at Esashi and 0.11 ngal on the amplitudes at Matsushiro.

		Esashi		Matsushiro	
Wave	Freq. deg/h	Amp. ngal	Phase deg	Amp. ngal	Phase deg
M_3	43.4762	35.97	15.1	17.56	341.0
SP_3	44.9590	25.92	32.2	14.39	42.0
S_3	45.0000	15.19	77.2	10.35	89.8
SK_3	45.0411	25.48	45.6	15.77	41.0
M_4	57.9682	11.79	328.6	7.36	333.5
MS_4	58.9841	5.43	26.1	1.54	143.5
$3SP_4$	59.9590	8.22	212.6	2.11	188.6
S_4	60.0000	8.10	251.0	3.47	268.9
S_5	75.0000	13.89	355.3	4.36	339.7

5.4 Discussion

Shallow-water ocean tides of 50 cm are observed in the northwest European shelf [*Andersen*, 1999] and waves of 10 cm are observed in the Bay of Fundy [*Merriam*, 1995]. These amplitudes are much larger than the amplitudes presented in this study concerning the Japanese east and west coasts. Using TOPEX/Poseidon satellite altimetry data, we may obtain a good spatial distribution of the tides in the northwest European shelf, and consequently good modeling of the shallow-water loading effect.

With the current accuracy of GPS, we may be able to observe vertical displacements due to shallow-water ocean tides in the northwest European shelf area. In addition, the previous case study (see Chapter 4) concerning GPS and OTL shows variations in the vertical displacements with periods near the third-diurnal, quarter-diurnal and fifth- diurnal tidal bands. They are believed to be artifacts resulting

from the GPS processing rather than being caused by geophysical phenomena. However, since the semi-diurnal and diurnal ocean tides are relatively large in the area considered in that study, the shallow-water loading effect may cause some of the observed third- diurnal, quarter-diurnal and fifth-diurnal vertical displacements.

5.5 Conclusion

Shallow-water tides at the Japanese east coast have an amplitude of a few millimeters, as observed from tide gauges. However, they are still able to generate an OTL signal at gravity sites located several hundred kilometres inland. The main part of the shallow water loading signal observed at Matsushiro is due to shallow water tides at the east coast. This is shown in Table 5.2, where the phase lags of the loading waves are consistent with the shallow water waves. To model the shallow water loading tides, we need to know the spatial distribution of the shallow water tides. This can be obtained by using more tide gauge sites or by using satellite data. However, satellite altimetry does not have an accuracy of millimeters, and the Japanese east coast is thus not a good test area for modeling the shallow water loading effect using altimetry data.

Shallow-water ocean tides of 50 cm are observed in the northwest European shelf area [*Andersen*, 1999]. These amplitudes are much larger than the amplitudes observed in Japan. Additionally, using TOPEX/POSEIDON satellite altimetry data it is possible to obtain a good spatial distribution of the shallow-water ocean tides, and consequently a good modeling of the shallow-water loading deformations. A study regarding shallow-water tides and GPS in the northwest European shelf area is currently ongoing. The purpose of the study is to analyze GPS time series due to Shallow-water tides and artifact signals in the third-diurnal, quarter-diurnal and fifth-diurnal tidal band. In order to separate the main the Shallow-water tides from artifact signal more than 1 year of hourly solution are needed. Furthermore, different strategies e.g. using overlap between the daily time windows are being used to eliminate possible software generated surface displacements.

Chapter 6

Postglacial Rebound in Greenland

6.1 Motivation

Glaciers and ice sheets have a strong influence on the physical environment and the shape of the Earth. As they melt or grow during climatic changes, they deform the Earth resulting in isostatic imbalance. The recovery of the isostatic balance may last several thousand years or even more. At the present time glacier ice covers about 1/10 of the Earth's land surface, where 94 percent is located in Greenland and Antarctica [*Sugden and John*, 1976]. However, during an ice age the ice may cover 1/3 of the total land surface of the Earth. One of the most important sources in revealing the climatic history is study of ice-core from polar ice. Several ice-core drilling projects have been performed in Greenland and Antarctica during the past couple of decades. Among these are the ice-core drilling projects in GRIP and GISP-2 in central Greenland. The GRIP and GISP-2 ice cores have a length of about 3 km corresponding to an age of about 250 kyrs BP (before present) for the ice at the bottom of the cores. The cores show, that the Earth has been through several dramatic climate changes during the past 130 kyrs and the 'Late Glacial Temperature Minimum' (LGTM) occurred nearly 21 kyrs ago [*Johnsen et al.*, 1995]. However, ice cores are not the only data source which can provide us with past temperature history. Variations in the $\delta^{18}O$ measurements in fossil foraminifera from ocean sedimentary cores can also provide us with useful climatic history. Additionally, sedimentary cores allow us to go further back than 130 kyrs. These glacial geological observations have showen periodicity in the climatic changes of about 100 kyrs, 41 kyrs, 23 kyrs and 19 kyrs, which according to *Milankovitch* [1941] can be attributed to variations in the precession of the Earth's axis, variations in the tilt of the Earth's axis relative to the orbit motion of the Earth around the Sun and variation in the eccentricity of the orbit.

The latest ice age, also know as 'Last Glacial Maximum' (LGM) occurred nearly 21.000 years ago and ice covered Canada, Greenland, Fennoscandia and Siberia in the north and the Antarctica in the south. To observe the ongoing glacial isostatic adjustment in Greenland, GPS and tide gauge observations are used. The tide gauge observations are measurements of sea level relative to the surface of the crust. These observations contain several contributions caused by various physical mechanisms. In order to observe the surface deformation caused by glacial isostatic adjustment, we have to distinguish between those relative sea level variations, which are isostatic (caused by tectonic processes, sedimentation and isostatic rebound

following removal of ice) and those, which are eustatic. The eustatic relative sea level variations are caused by changes in the volume of the water in the global oceans. The separation of the isostatic variations from the eustatic variations can be obtained using e.g. TOPEX/POSEIDON (T/P) altimetry data. Performing the difference between the tide gauge and T/P observations gives an estimate of the vertical crustal motion.

In this case study the main focus will be on the secular vertical surface motions in west Greenland. A Previous study by Wahr et al. [2001] showed that the area is subsiding due to the Earth's viscoelastic response to past ice mass variability. In their study they use GPS data from Kellyville (KELY) and Kulusuk (KULU) (see Figure 6.1). They showed that KELY is sinking by 5.8 +/- 1.0 mm/yr and KULU is sinking by 2.1 +/- 1.5 mm/yr. The subsidence at KELY is explained by glaciation during the last 4000 years, although the area has been deglaciating prior to 4000 years ago. This is in fact supported by geological evidence in the area, which shows that the ice sheet may have expanded by about 50 km during the last 4000 years [*Le Meur and Huybrechts*, 1996]. However, the geologic observations were carried out only in the Kangerlussuaq area (near KELY). Furthermore, the recent uplift model by Tarasov and Peltier do also show subsidence at the western part of Greenland [*Tarasov and Peltier*, 2002]. In their recent GrB ice-sheet margin model they show that the ice sheet margin in west Greenland (between latitude 62° N to 72° N) has re-advanced during the last 8000 years to its current position, resulting in subsidence of land along the west coast. In this thesis I will take a closer look at the area below latitude 65° N, and see whether the re-advance of the ice-sheet margin also took place in this area or the re-advance only occurred in the mid-western part of Greenland.

The first scientific investigation concerning glacial isostatic adjustment process, which suggests sinking of west Greenland was published by Captain F. Froda in 1925. In July 1897 Captain F. Froda measured the height of some balanus-stripes on a rock relative to a fix point [*Froda*, 1898],[*Froda*, 1925]. His method is based on the concept that the balanus-stripes on the rocks at the coast are found at a rather constant distance below the mean level of high water. Thus, the sinking of land may therefore be determined by measuring the height of the balanus-stripes relative to a fixed point at different time. He made the first observations in Godhavn (marked with a triangle in Figure 6.1) in 1897 and then repeated his observations in 1923. He discovered that the land has sunk 15 cm during a time period of 26 years. In 1946 J. F. Chantelou repeated the measurements made by Captain F. Froda in Godhavn. The results of these observations were published by *Egedal* in 1947 suggesting that the land is sinking by about 1 cm/yr. It should be noted that both of these publication neglect the eustatic contribution.

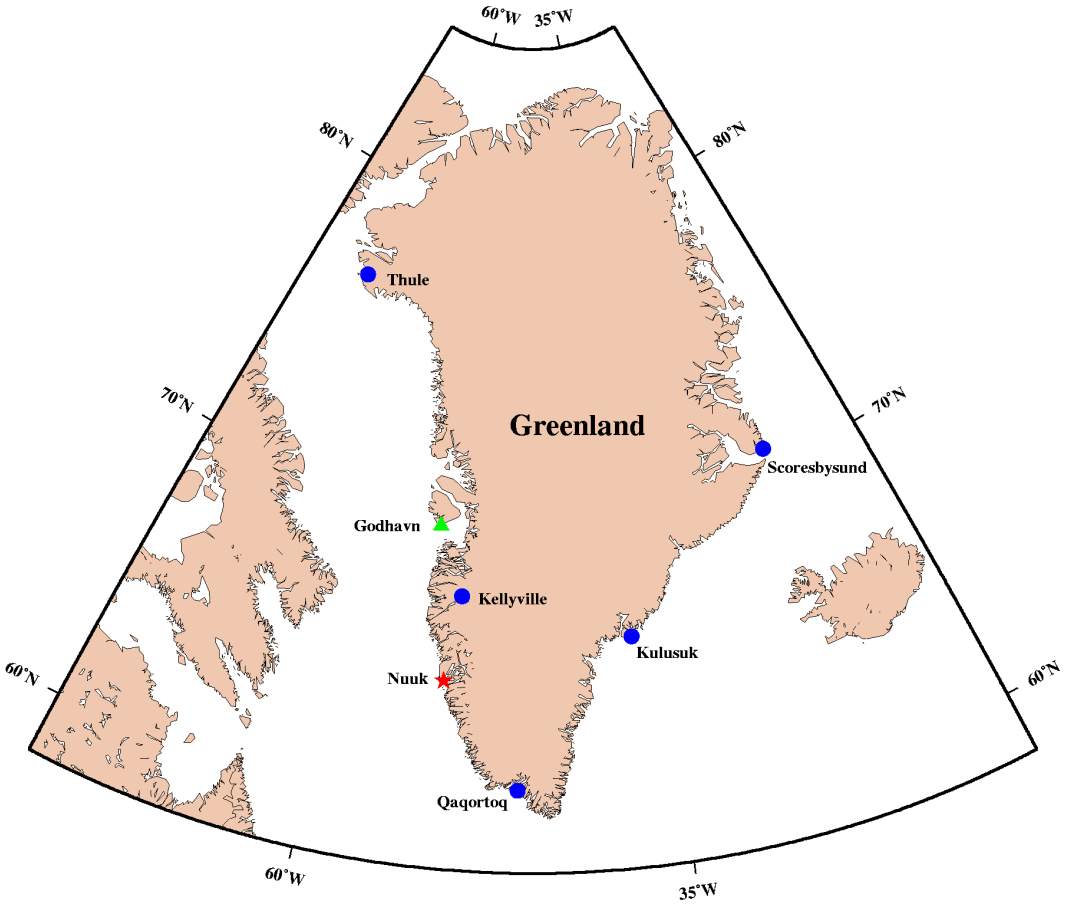

Figure 6.1: Location of GPS sites (blue dots), tide gauge (red star) and historic sea level observations (green triangle).

The plan of this chapter is as follows. I will start with a short description of the latest deglaciation models. The theory is already discussed in Chapter 3 (Surface load on a spherical Earth). Here, I will describe the data source, Earth model and the land/ice/ocean resolution used to construct the deglaciation models. Next, I will analyze GPS, tide gauge and Topex/Peseidon observation in order to estimate the secular surface motions in Greenland. Finally, the results will be discussed and the re-advance of the ice-sheet in western Greenland will be considered.

6.2 Deglaciation models

A glaciation or deglaciation model can be constructed by use of the sea level equations if RSL (relative sea level) history is available. RSL history can be achieved from different geological sources. One of the most important sources is carbon dating of RSL using e.g. mollusk shells, whalebone or wood. Age determination using ^{14}C is nowadays a widely applied method and indeed very useful in reconstruction of the sea level history. Using ^{14}C it is possible to reconstruct local changes in ice thickness. Similar to the ^{14}C method, U and Th can also be used for age determination and thereby the sea level variations. Another deglaciation history revealing

source is the ratio between ^{18}O and ^{16}O in deep-sea sedimentary cores. If e.g. an ice sheet grows, ^{16}O is removed from the oceans and stored in the ice. Thus, the ratio between ^{18}O/^{16}O increases in the ocean (and the marine microorganisms). Hence, a large ratio corresponds to a glacial maxima and small ration corresponds to interglacial periods. Basically, variations in the oxygen ratio over time can directly be translated to past surface temperatures. While the ^{14}C method reveals local changes in ice thickness, the oxygen ration reveals global changes in ice thickness. Both δ^{18}O and ^{14}C are used to constrain deglaciation models.

6.2.1 ICE-3G

The ICE-3G deglaciation model was created by *Tushingham and Peltier* in 1991. The model is a modification of the earlier models ICE-1G and ICE-2G [*Wu and Peltier*, 1983]. Unlike ICE-1G and ICE-2G, the ICE-3G model is global containing deglaciation history from Greenland, Iceland, Canada, Scandinavia etc. The model describes the global deglaciation history from 4 kyrs to 18 kyrs B.P. Hence, changes in the ice volume during the last 4 kyrs are not covered by the model.

The ICE-3G model is tuned to fit ^{14}C dated RSL history globally. In the tuning procedure a total number of 192 sites are used, where 69 are located in Artic Canada and Greenland, 73 in Northern Europe and 25 in Eastern Europe and the rest elsewhere. The tuning procedure is as follos; RSL of a site is compared with modeled estimate, if e.g. the modeled RSL is lower than the observed value, then the thickness of the ice load is either increased or the melting delayed. The iteration process is performed about 19 times until the model fits the observations. Once the deglaciation model has been created it is compared with δ^{18}O observations. Since, δ^{18}O is not used in the first part of the modeling it can, in some sense, be used to evaluate the model obtained from the ^{14}C RSL observations. Afterward, δ^{18}O is used to additionally constrain the ICE-3G model.

An important issue in modeling of the various deglaciation models is the choice of viscosity profile through the Earth. The problem is simplified by assuming the viscosity has only a radial dependency. The ICE-3G deglaciation model uses the viscosity profile shown in Table 6.1. The ICE-1G and ICE-2G have shown that the profile in Table 6.1 is reasonable. The thickness of the elastic lithosphere is set to 120 km. The upper and lower part of the upper mantle have a constant viscosity of 1×10^{21} Pa s, while the lower mantle have a viscosity of 2×10^{21} Pa s.

Table 6.1: Radial viscosity profile used to create the ICE-3G model

Layer	Outer radius	Viscosity [10^{21} Pa s]
Lower mantle	5701 km	2.0
Lower part of upper mantle	5971 km	1.0
Upper part of upper mantle	6251 km	1.0
Elastic lithosphere	6371 km	0.0

Figure 6.2 (A) displays uplift rates in mm/yr obtained using the ICE-3G model and the viscosity profile shown in Table 6.1. Similar to the ocean tide models, the ICE-3G deglaciation history load model is defined by a number of cells

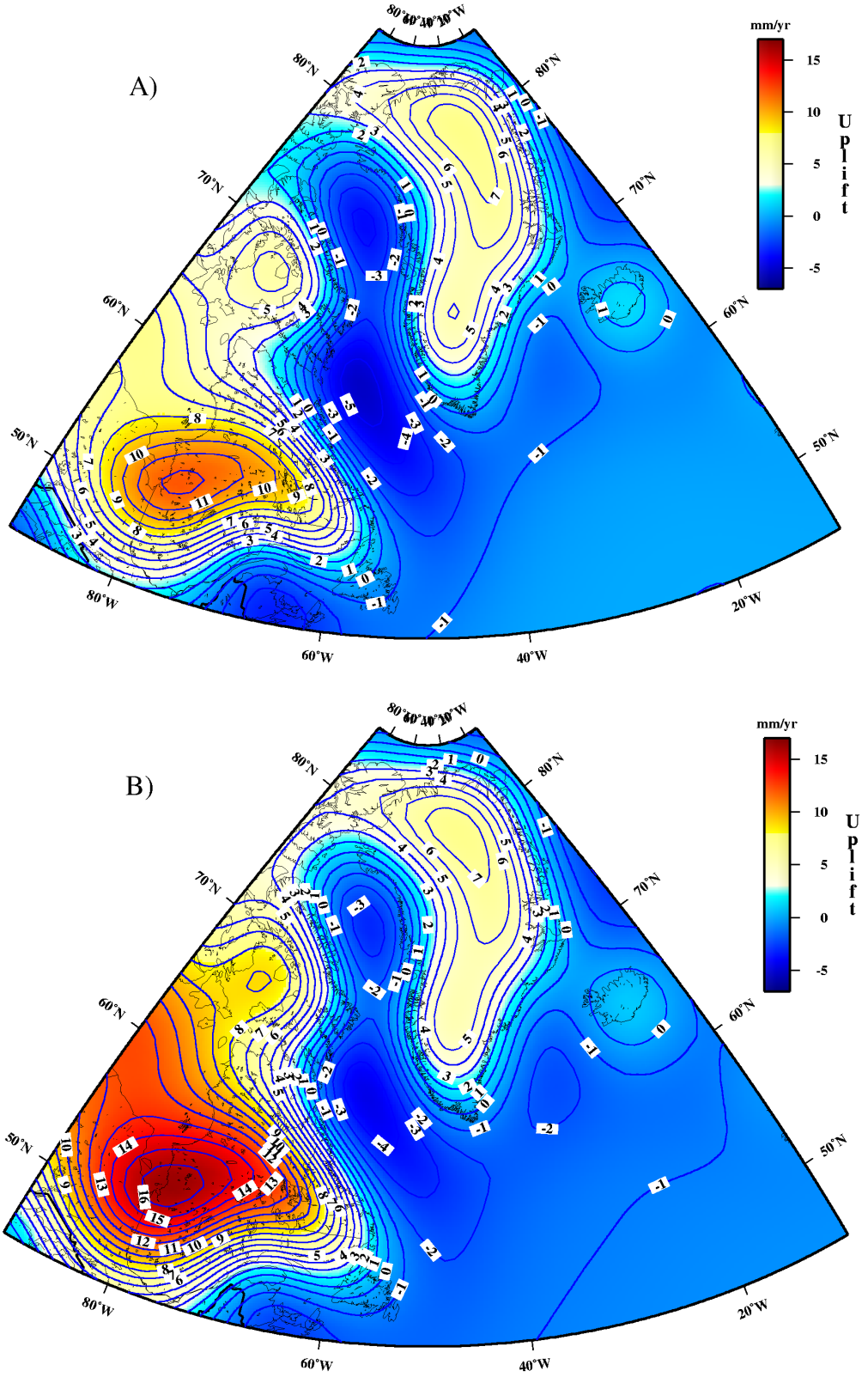

Figure 6.2: Predicted vertical displacements in mm/yr due to deglaciation. A) ICE-3G predictions obtained using the viscosity profile given in Table 6.1, B) ICE-3G predictions obtained using the viscosity profile given in Table 6.2.

with each cell containing the thickness and time of the ice load. However, the cell size and structure used to construct the ICE-3G model is very different from what is used in the case of ocean tide models. First of all the cells used in ICE-3G have the form of a disc, additionally, the size of the discs vary. Usage of disk-formation will off course lead to overlap in some area and gaps in other areas. The total number of cells (discs) used in the ICE-3G is 808. The oceans in the ICE-3G are also defined using disc-cells. The total number of 'ocean-discs' used is 557. In order to describe the land-sea lines as best as possible, small discs are used near coastlines, while large discs are used in open oceans areas.

The influence of a viscosity profile is demonstrated by Figure 6.2 (B). The figure shows uplift rates in mm/yr obtained using the ICE-3G deglaciation model. However, the viscosity profile used in Figure 6.2 (B) is different from the one used in Figure 6.2 (A). Table 6.3 displays the viscosity profile used to predict the uplift rated in Figure 6.2 (B). The profile is a simplification of the improved viscosity profile used by Peltier in the recent models i.e. ICE-4G and ICE-5G [*Peltier*, 2002]. The original modified profile contains more than 40 layers, it is simplified here to make it comparable with the profile given in Table 6.1.

Table 6.2: Radial viscosity profile as used in Figure 6.2 (B)

Layer	Outer radius	Viscosity [10^{21} Pa s]
Lower mantle	5701 km	5.0
Lower part of upper mantle	5971 km	2.0
Upper part of upper mantle	6251 km	0.7
Elastic lithosphere	6371 km	0.0

Differences between the two viscosity profiles are rather small in Greenland, mainly because Greenland is still covered with a thick layer of ice. However, differences between the two models are really visible in Eastern Canada, because the ice has melted and the land is uplifting. The differences between the two viscosity profiles yields differences of the uplift rates of almost 5 mm/yr in Eastern Canada.

6.2.2 ICE-4G

The ICE-4G model by Peltier is a modification of the IGE-3G model. A detailed description of the model will not be given here, since the basics data and method for creation of the deglaciation history is similar to what is used to obtain the ICE-3G deglaciation history. The main difference between ICE-4G and ICE-3G is the timing of the deglaciation events [*Peltier*, 1995]. Furthermore, additional RSL sites are used to constrain the ICE-4G model.

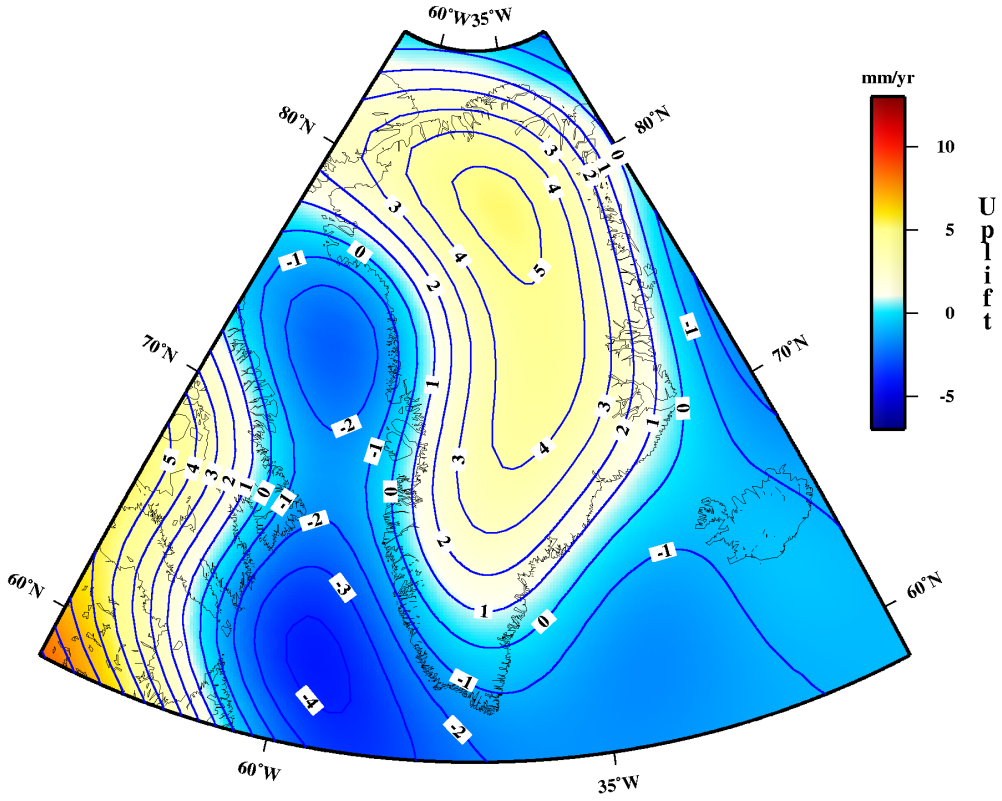

Figure 6.3: Predicted vertical displacements in mm/yr due to ICE-4G deglaciation history.

Figure 6.3 displays uplift rates in mm/yr of the ICE-4G model. ICE-4G predicts current uplift rates of about 7 mm/yr in the center of the ice-sheet, while ICE-3G predicts uplift rates of about 5 mm/yr. The differences are rather small for Greenland.

6.3 GPS and tide gauge observations

In May 1995 Kort og Matrikel-Styrelsen (KMS) established the permanent GPS station, THU1, at Thule Airbase (see Figure 6.1). The station consist of an Dorne Margolin antenna with chokerings and a ROGUE SNR-12 RM GPS receiver. The station has been operated fine most of the time, however, in 1997 and 2001 the data contains relatively large gaps due to failure in the connection between the receiver and antenna. The THU1 GPS antenna is mounted on the roof of an apartment building owned by the US air force. The building is made of steel and is not an ideal place for GPS observation, because the building may expand/compress due to temperature variations. In order to avoid thermal variations, in March 1999 KMS established a second GPS station, THU2, at Thule airbase. The distance between the THU1 and the THU2 antenna is 963.312 meters. THU2 consist of an ASH701073.1 antenna with dome and an Ashtech Z18 receiver. The antenna is monitored on a concrete pillar on bedrock. The THU2 data contains relatively large gaps in 1999 and 2000, however, after 2000 the station has been collecting

data without significant gaps. THU1 contains no antenna replacements, while the THU2 antenna was replaced once on November 17, 2000. Figure 6.4 displays the Thule GPS stations, THU1 and THU2.

Figure 6.4: THU1 and THU2 GPS sites at Thule air base in Greenland.

Besides the GPS stations in Thule, KMS is also running a permanent GPS station, SCOB, in Scoresbysund, which was established in August 1997 and a permanent station, QAQ1, in Qaqortoq, which was established in October, 2001. The SCOB antenna has never been replaced, while the QAQ1 antenna has been replaced three times during fall 2003. On August 26, 2003, the original antenna, an ASH701941.B with dome, was bowed away from the pillar. On September 5 the antenna was monitored back on the pillar, however, without the dome because it was damaged. A new dome was mounted on the antenna on September 29, 2003. On December 30, 2003, the original antenna was replaced by an ASH701945EM.

University of Colorado and the ECGS operates the station KELY near Kangerlussuaq and the station KULU in Kulusuk. KELY was installed in July 1995 and KULU was installed in July 1996. KULU has one antenna replacement, and KELY has had two antenna replacements. The dates of the antenna replacements are listed in Table 6.3. Furthermore, THU1, KELY and QAQ1 are also included in the IGS network.

Table 6.3: Date of antenna shifts and when the stations started operating.

Site name	Installed	antenna shift 1	antenna shift 2	antenna shift 3
THU1	1995-05-02			
THU2	1998-10-26	2000-11-17		
KELY	1995-07-23	1996-04-05	2001-09-14	
QAQ1	2001-10-15	2003-09-05	2003-09-29	2003-12-30
KULU	1996-07-21	1999-05-09		
SCOB	1997-08-09			

The tide gauge data used in this study is collected by Farvandsvæsnet (FRV). In 1992 FRV installed a tide gauge in Nuuk (also known as Godthaab) on the west coast of Greenland (see Figure 6.1). The tide gauge instrument is placed on the bottom of a well to be protected from flowing objects. The tide gauge consists of a pressure instrument, which measures the bottom pressure variations

and additional instruments to measure the temperature and the salinity in the water. The NUUK tide gauge data contain relatively large gaps mainly due to freezing of the water during winter periods. During about 10 years of measurements, 3 winter periods have led to serious data gaps, while the instrument has survived the other winter periods without loss of data. In the summer 2004 the NUUK-tide gauge stopped operating in Nuuk and was moved to its new location at Thule Airbase. Furthermore, in the future Danish Spacecenter (DS) will be responsible for collection and distribution of the tide gauge data for all tide gauges in Greenland.

6.4 Analysis of the GPS data

Site coordinates were estimated using the GIPSY OASIS II software [*Zumberge*, 1997] developed at the Jet Propulsion Laboratory (JPL). GPS orbits, Earth orientation, and clock products obtained by JPL based on a global network of GPS sites were used in the data processing. Receiver clock parameters and atmosphere parameters were modeled and a cut-off angle of 15 degrees was used. The data were corrected due to the solid Earth tide and the ocean tide loading effect. The amplitudes and phase lags of the main ocean tide loading signal were calculated using the online loading provider by H.-G. Scherneck (see www.oso.chalmers.se/∼loading). The GOT00.2 [*Ray*, 1999] ocean tide model was used for the loading correction. Site coordinates for each day were obtained using precise point positioning (PPP). The site coordinates were computed in the nonfiducial frame and then transformed to the ITRF2000 frame. The transformation parameters from the free-network estimates to the ITRF2000 for a particular day are available at the following ftp site, 'sideshow.jpl.nasa.gov/pub/gipsy_products/x-files'. Figure 6.5 displays the daily point solution for THU1 and THU2. The Figure at the top displays north-south displacements, the one in the middle displays east-west displacements and the Figure at the bottom displays vertical displacements. The two Thule stations are located less than a kilometer from another; hence, the secular uplift rate is assumed to be the same at both locations. However, the annual and semiannual signal is not identical at both sites. To estimate secular displacements at Thule, data from both stations is used. From May 2, 1995, to April 19, 2001, data from THU1 is used and from April 20, 2001 to December 2004 data from THU2 is used. Station change on April 19, 2001, is selected because it gives fewest gaps and fewest antenna offsets for the combined time series. In the following the combined THU1 and THU2 time series will be denoted THUL. Figure 6.6 displays the vertical displacements for THUL. The arrow on April 19, 2001 marks the offset between THU1 to THU2. The offset (a constant displacement introduced at April 19, 2001) is obtained by fitting (using least squares) a secular term, annual and semi-annual terms and an offset simultaneously to the daily solutions shown in Figure 6.5. An annual and a semi-annual term is simultaneously fitted to the THU1 daily solutions and another annual and semi-annual term is fitted to the THU2 daily solutions. Each daily solution is weighted with the 1σ formal error generated by the GIPSY OASIS II software. The solid curve in Figure 6.6 displays the fitted displacements. Note, the differences in the annual and semi-annual varying displacements before and after

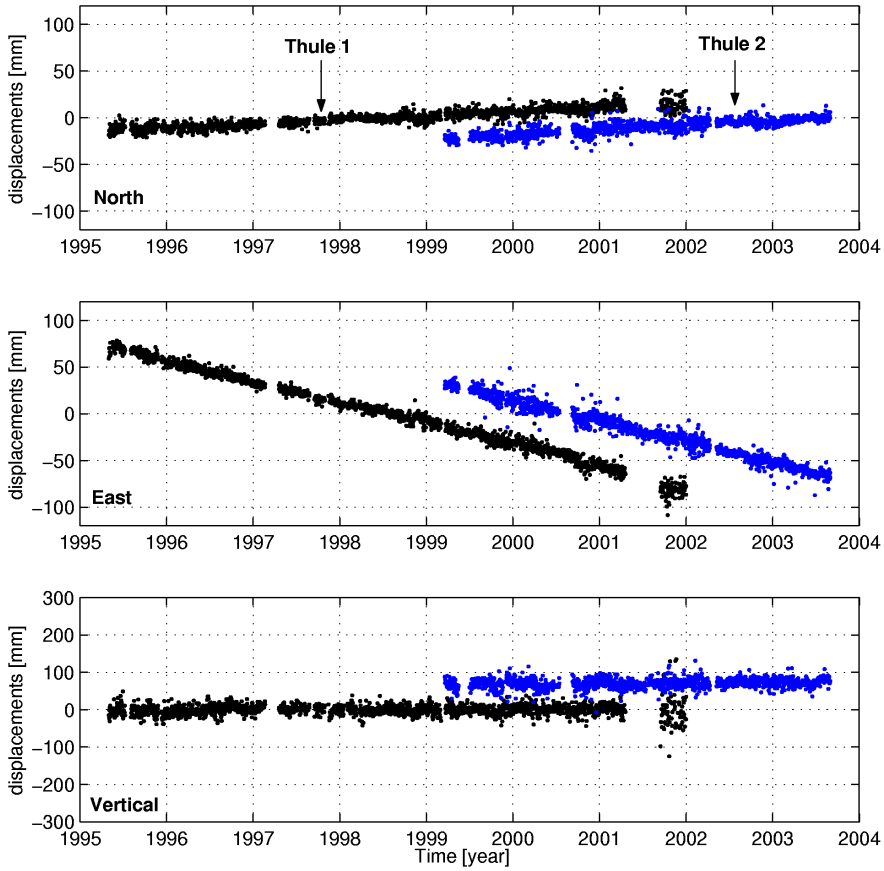

Figure 6.5: point solutions for THU1 and THU2. North (Top), east (middle) and vertical (bottom) displacements.

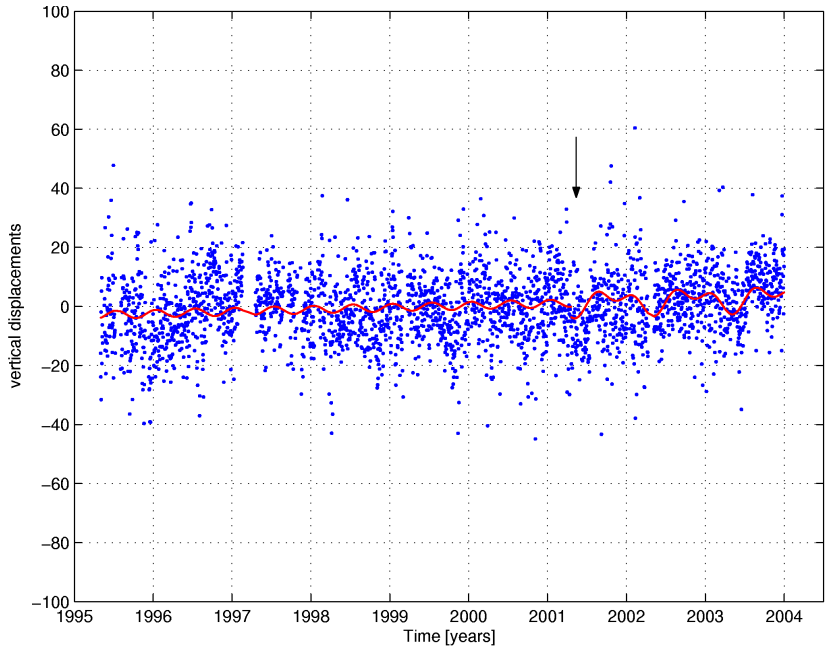

Figure 6.6: Vertical displacements for THUL. The solid curve displays an annual, semi-annual and secular fit.

the offset. As shown by *Wahr et al.* [2001] the daily solutions are not entirely uncorrelated. The correlation is taken into account by estimating the decorrelation time for the residuals of the daily solutions. The residuals are obtained by removing the offset, the secular, annually and semi-annually varying terms from the daily solutions. Figure 6.7 (A) displays the autocorrelation for THU1 for the vertical

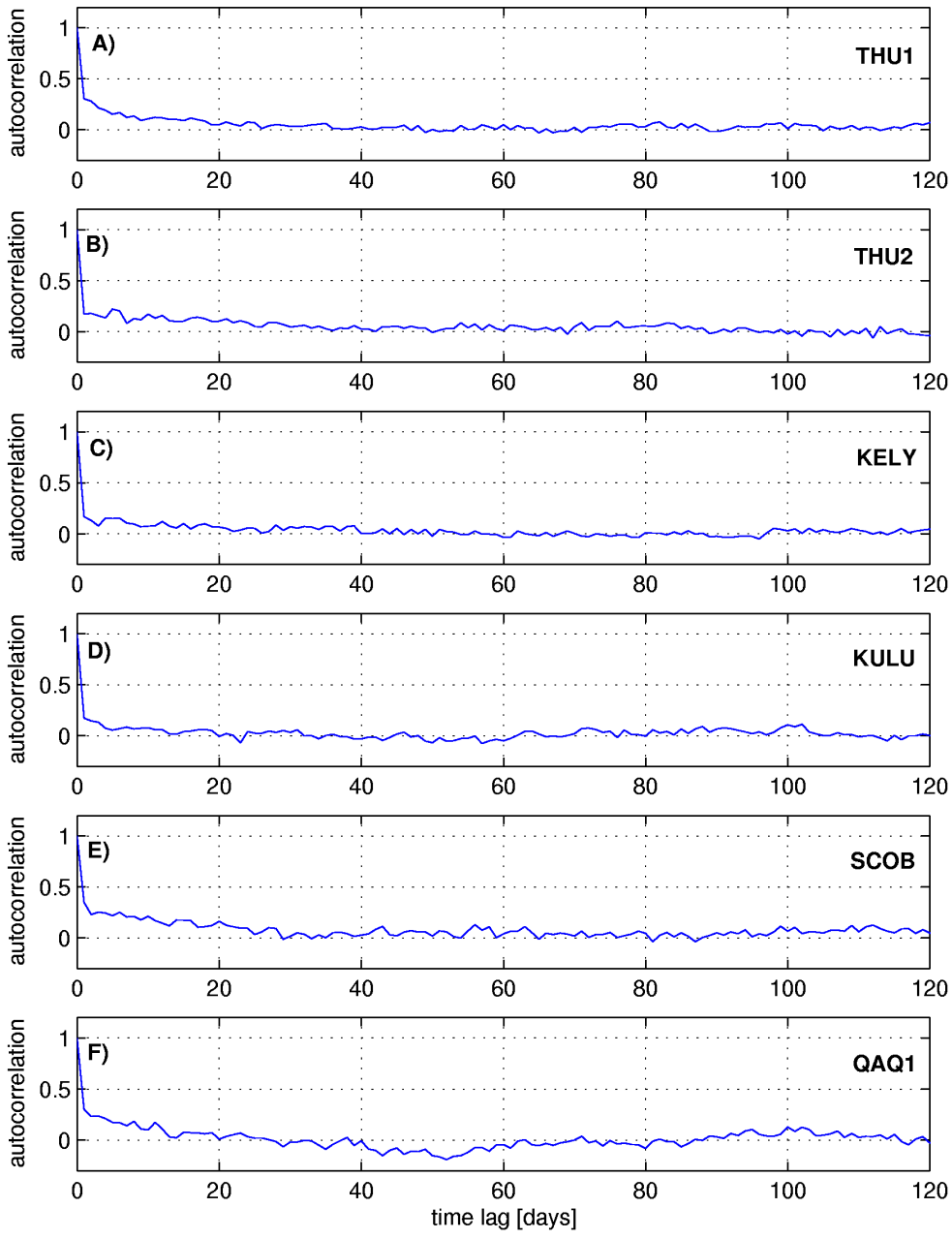

Figure 6.7: Autocorrelations of the vertical residuals.

displacements and Figure 6.7 (B) displays the autocorrelation for THU2. The time lag, τ, is given in days. The figures show that the autocorrelation for both sites decreases significantly during $\tau = 0$ to $\tau = 1$. Furthermore, at both Thule stations the autocorrelation decreases to about zero when the time lag τ becomes about 36 days. This correlation over time is caused by e.g. modeling error of the troposphere,

satellite orbit errors, and loading from the atmosphere, ocean, and water/snow/ice on land. These effects do not change much within 1 km, which explains why we observe almost the same decay time at both Thule stations. The decorrelation times for KELY, KULU, SCOB and QAQ1 are 40, 32, 29 and 27 days, respectively. Thus, multiday averages are constructed for each site depending on the decorrelation time. For THUL, averages of 36-day are constructed, for KELY averages of 40 day are constructed etc. Now, each average has to be assigned with an error. However, the 1σ formal errors generated by the GIPSY OASIS II (PPP) does not take orbit errors into account. A more realistic error can be obtained simply by multiplying the 1σ formal errors with a constant, c. The constant, c, is obtained by χ^2 fitting [*Numerical recipes in fortran 77*, pp 654-660] the residual to the mean value for the given interval. The constant is obtained under the conditions, that the number of degree of freedom (number of observations minus number of unknowns) is about χ^2, and the quantity value Q is between 0.5-1.0. This gives a more realistic estimate of the error. For the 36-day averages for THUL, 'c'-values between 2.5 and 5 have been estimated. The errors for the 36-day averages for THUL becomes about 3 mm. Assigning these χ^2-errors to the 36-day averages, a secular term, annually and semi-annually varying terms are simultaneously fitted to the 36-day averages. An uplift rate of 0.53 ± 0.13 mm/yr is obtained for THUL. However, the error due to reference frame drift is not included in this error estimate. To account for this effect the formula by *Argus and Heflin* [1995] is used. They suggest that the frame error can be expressed as ±5 mm/*(number of years of data).* The data span for THUL is about 9.6 years. Thus, the frame error is 0.52 mm/yr. The best uplift rate for THUL including all error considerations is thus 0.53 ± 0.54 mm/yr. Figure 6.8 displays the 36-day averages and the modeled secular, annually and semi-annually terms. Similar procedure is carried out for KELY, KULU, SCOB and QAQ1. Using 40-day averages for KELY an uplift rate of -3.80 ± 0.26 mm/yr is obtained. Here, errors due to two antenna offsets are included. When the reference frame error is taken into account the error increases to 0.60 mm/yr. An uplift rate of 0.99 ± 0.20 is obtained for KULU and an uplift rate of -0.38 ± 0.10 mm/yr is obtained for SCOB. The error for SCOB is relative small because of no antenna replacements, while one antenna replacements is taken into account in the estimation of the KULU uplift error. Taking the reference frame error into account, the KULU uplift error becomes 0.64 mm/yr and the SCOB uplift error becomes 0.69 mm/yr. Furthermore, an uplift rate of 3.23 ± 0.81 is estimated for QAQ1. Even though the antenna has

Table 6.4: Secular uplift rates.

Station	uplift rates	error without frame error	error with frame error
	[mm/yr]	[mm/yr]	[mm/yr]
THUL	0.53	0.13	0.54
KELY	-3.80	0.26	0.60
KULU	0.99	0.20	0.64
SCOB	-0.38	0.10	0.69
QAQ1	3.23	0.81	1.76

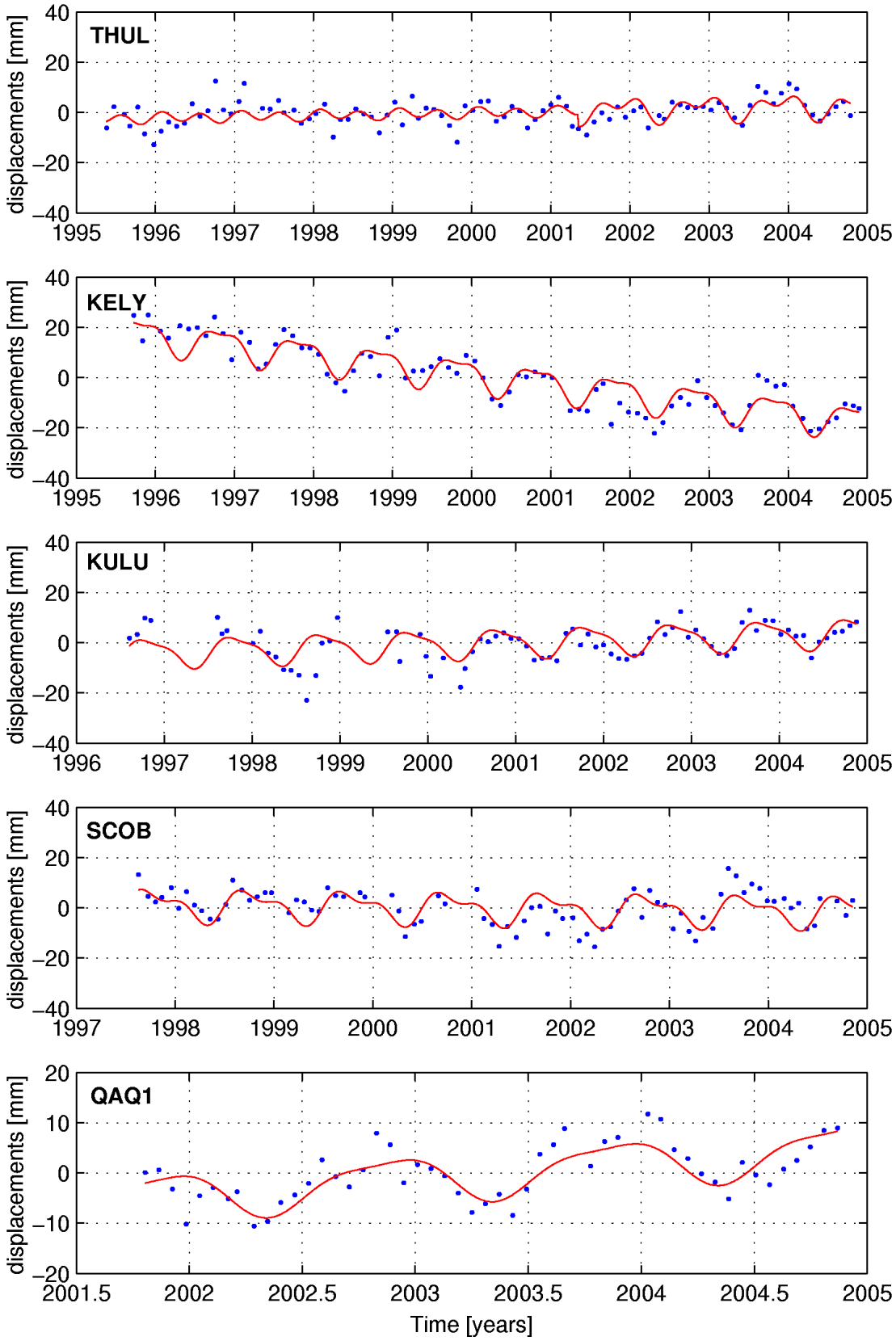

Figure 6.8: Multiday averages and the fitted secular, annually and semi-annually vertical variations for THUL, KELY, KULU, SCOB and QAQ1.

been replaces three times, only two offsets have been introduce in the uplift estimations. The reason is that observations between September 5, 2003 and September 29, 2003 are not included. Introducing two offsets in the uplift estimations and taking the reference frame into account the error becomes 1.76 mm/yr. Uplift rates and errors are listed in Table 6.4.

Figure 6.9 displays a convergence plot for THUL and KELY. The plot is obtained by fitting a secular term to the first 300 days of observation, then 36 days are added, and further 36 days are added etc. Each secular solution is plotted as a dot and the time represent the termination time of data used to estimate the uplift rate. The figure shows that THUL has almost converged to a constant value, while KELY seems to be oscillating between -3.8 mm/yr and -4.5 mm/yr.

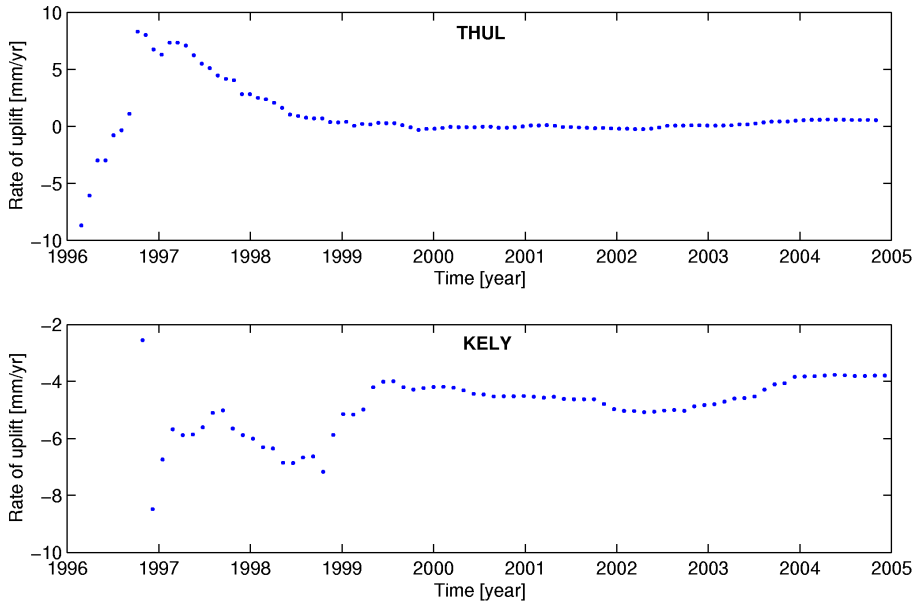

Figure 6.9: convergence plot for THUL and KELY

6.5 Analysis of the tide gauge and satellite altimetry data

The satellite radar altimeter mission TOPEX/POSEIDON (T/P) has provided sea level measurements with near-global coverage (66° S 66 N°), 23 cm point-to-point accuracy, and 10-day temporal resolution for over 12 years, greatly exceeding its design lifetime [*Fu and Cazenave*, 2000]. Since T/P was launched in August 1992, it has operated in several phases that in many respects can be treated as separate missions. In addition to the experimental POSEIDON altimeter, two distinct TOPEX altimeters have operated. The primary TOPEX-A altimeter operated from shortly after launch until January 1999. After instrument degradation was observed starting in mid-1997, redundant backup TOPEX-B began to be used as the primary science instrument for the remainder of the mission. The last T/P 10-day repeat cycle to use TOPEX-A was cycle 235, ending on 9 February 1999. TOPEX-B was

turned on at the beginning of cycle 236 on the same day. At the end of the verification phase of T/P's successor Jason, the original T/P mission ending during cycle 365, and the satellite was moved to a new orbit during a month-long drift phase.

TOPEX data from Merged Geophysical Data Records Revision B (MGDRs) for cycles 10 to 365 to compute along-track values for sea surface height (SSH) is used in thus study. T/P's along-track sampling frequency is roughly 1 Hz, equivalent to 7 km. Several modifications to the MGDRs have proved necessary. First, is replaced the MGDR ocean and load tides with those from the GOT99.2 model and equilibrium long-period ocean tides with those used for Jason. Corrections are applied for known errors in the wet troposphere and sea state bias models.

Two modifications to the wet troposphere path delay were applied. *Keihm et al.* [2000] discovered a drift in one channel on the TOPEX Microwave Radiometer (TMR), which caused a noticeable drift in comparisons between T/P SSH measurements and a global tide gauge network [*Mitchum*, 1998]. Correction for this drift is applied based on global means [*Keihm et al.*, 1998]. Furthermore, A TMR yaw correction to account for a slightly greater path delay when the satellite is in fixed rather than sinusoidal yaw is also included. This TMR yaw correction, available on the GDR Correction Product Version C, accounts for the 15-hour thermal transition between yaw states [*Zlotnicki and Callahan*, 2002].

Chambers et al. [2003] estimated new sea state bias models for each of the two different TOPEX altimeters that have operated during the mission. Replacing the SSB model on TOPEX removes most of the 37 mm bias between TOPEX-A and TOPEX-B that had been observed in the tide gauge calibrations. Furthermore, retracking corrections or corrections to the ionosphere path delay that result from changes to the sea state bias model are not applied.

Because it is difficult to test the instruments once they are on-orbit, the calibration of the altimeter sea level measurements using tide gauge measurements has always been a critical component of sea level determination [*Chambers et al.*, 1998; *Mitchum*, 1994; *Mitchum*, 1998; *Mitchum*, 2000]. The tide gauge calibration results have uncovered numerous problems with the measurements since the launch of T/P. With each improvement, the calibration is recomputed, and thus the T/P dataset has undergone a continuous series of improvements over time. The tide gauge calibration sometimes uncovers errors in the measurements that cannot be initially identified, and thus the calibration values have often been applied directly to the measurements to create a correct sea level [*Nerem*, 1995; *Nerem et al.*, 1999; *Nerem et al.*, 1997]. The drift during the original T/P mission estimated from the calibration is 0.1 ± 0.4 mm/year [*Leuliette et al.*, 2004]. The calibration error is almost entirely driven by errors in the land motion estimates used for each of the tide gauges [*Mitchum*, 2000]. As this correction is consistent with no drift over the ten-year period used in this study, it is elected not to apply the calibration values to the sea surface heights.

Finally, variations in the sea surface attributable to a hydrostatic response to changes in atmospheric pressure, known as the instantaneous inverse barometer (IB) effect is removed. The IB field available on the MGDRs assumes a constant mean global surface pressure. Here, we substituted the constant mean with time-varying mean global pressure over the oceans computed from ECMWF atmospheric pressure products. Figure 6.10 displays T/P along-track points near the tide gauge site in Nuuk.

The tide gauge data for Nuuk obtained from FRV has a sampling rate of 15 minutes. The data consists of relative sea level variations and atmospheric pressure observations. The inverse barometer effect is removed using the formula,

$$h_{IB} = -9.948(P_{obs} - P_g)$$

P_{obs} is the observed pressure in millibars at the tide gauge site and P_g is the global mean pressure in millibars. The resulting inverted barometer correction, h_{IB} is given in millimeters. The Global mean pressure is interpolated from values determined at 6-hour intervals from CNES. Furthermore, the ocean tides, h_{ot} are removed from the observed relative sea level variation by modeling these tides imperially. Thus we have,

$$h_{residual} = h_{observed} - h_{IB} - h_{ot}$$

To estimate an uplift rate at NUUK, sea surface height measurements at NUUK are required. Moreover, the time span of sea surface height time series has to be identical to the time span of the tide gauge time series. The time series of sea surface height measurements near the NUUK tide gauge is constructed by computing a weighted mean of TOPEX/POSEIDON (T/P) values sampled within 75 km of the station (29 along-track locations as shown in Figure 6.10). T/P data is processed as described in *Leuliette et al.*, [2004]. Seasonal variations are removed with a least-squares fit at annual and semi-annual periods. The mean is weighted using the distance from the gauge to each along-track point. Only T/P sea surface heights during the original mission (January 1993-August 2002) is used.

In order to see whether the residual tide gauge signal is showing the same variations as T/P signal, a filtering procedure is performed on both time series. Figure 6.11 displays filtered time series. The green curve shows a time series of the Nuuk tide gauge observations. The red curve shows a time series of the interpolated T/P measurements. The blue curve shows a time series of the T/P along track point no 07. The filtering procedure is as follows; the mean value is estimated for an interval of 365 days (=window of 365 days). Then, the window is moved 30 days and the mean for this 365-day interval is estimated. Then, the window is again moved 30 days and the mean is estimated etc. This mean estimation procedure basically removes all variations with period less than 1 yr.

The time series of the interpolated T/P measurements and the time series of the along track point no. 07 are very similar. During the period from June 1994 to end of 2002, all three time series show almost the same variations. However, there seems to be an offset in the tide gauge observations after the large gap during winter 1994.

The filtering procedure is only performed to detect the offset, thus, filtered data is not used to estimate the uplift rate at NUUK.

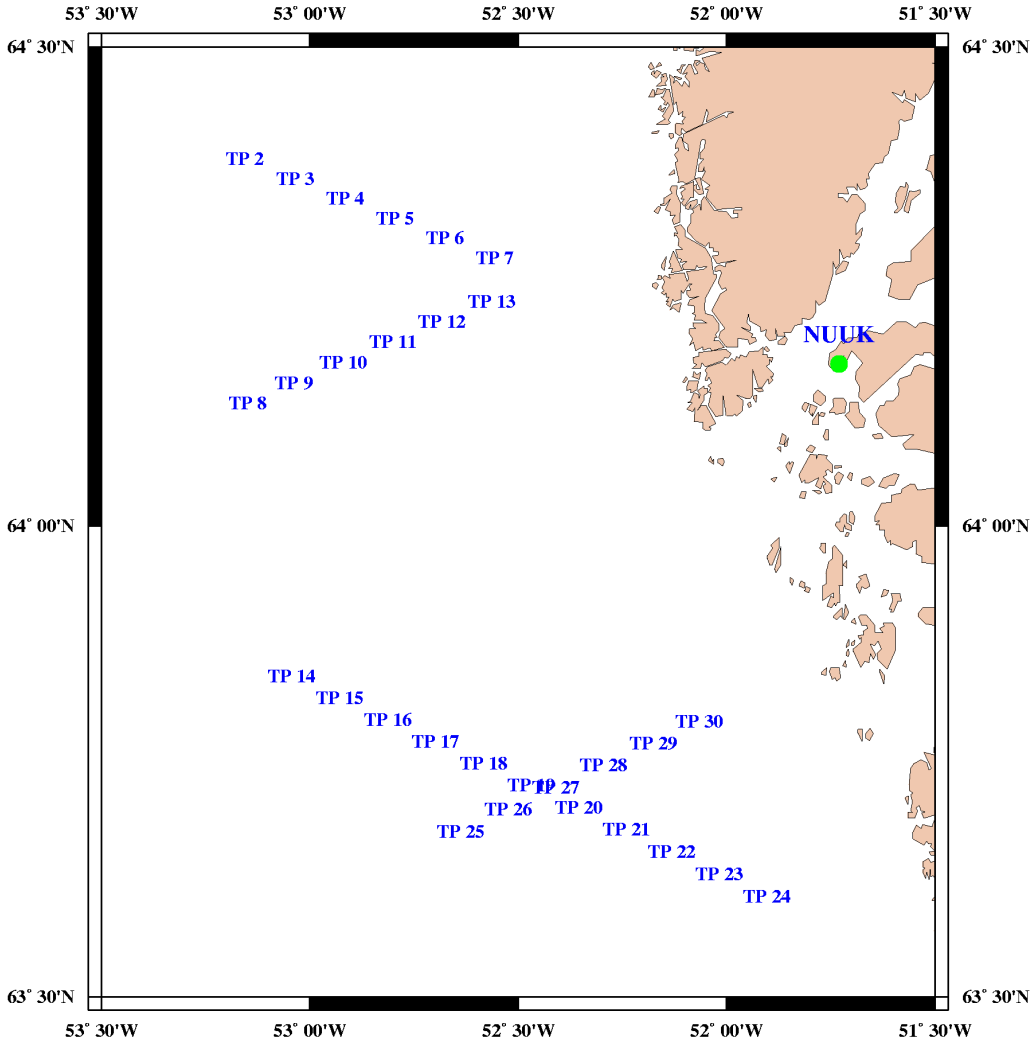

Figure 6.10: Location of the TOPEX/POSEIDON along-track points near Nuuk.

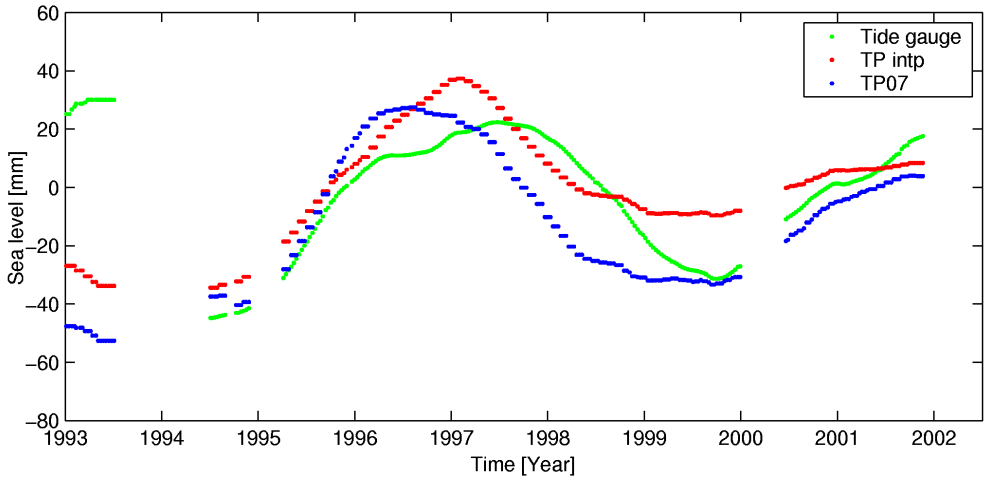

Figure 6.11: Filtered time series for the TP along-track point no. 7, the tide gauge in NUUK and the interpolated TP measurements.

Figure 6.12 displays the "interpolated TP measurements" minus the "tide gauge observations". The solid line is a linear fit. In order to avoid introducing an offset during the fitting procedure, data measured before 1994.5 is not used. Fitting the monthly mean variations using chi-square to a straight line yields an uplift rate of -1.68 +/- 1.75 mm/yr at NUUK.

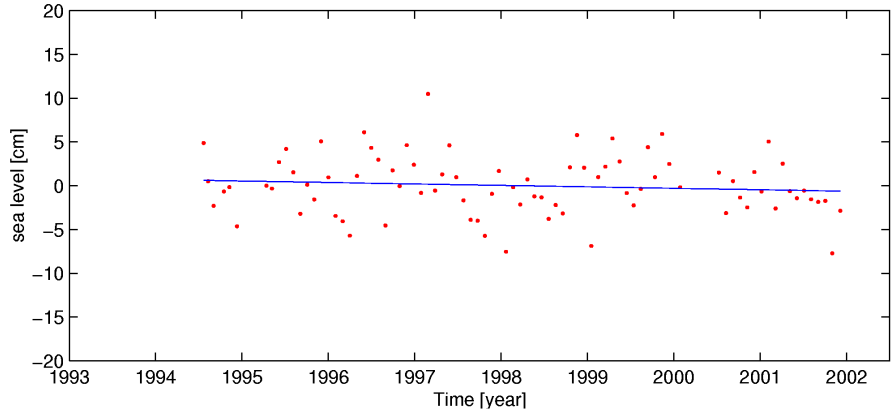

Figure 6.12: Monthly averages of the "interpolated TP measurements" minus the "tide gauge observations. The solid line is the best linear fit.

6.6 Results

Uplift rates for the GPS sites and the Nuuk tide gauge site are listed in Table 6.5. Also is listed modeled uplift rates based on the ICE-3G deglaciation history. There seems to be disagreements between the modeled and observed value for especially KELY and NUUK. *Wahr et al.* [2001] explains the disagreement with the fact, that the ICE-3G model does not include deglaciation history for the last 4 kyrs. Furthermore, Wahr suggests that the western ice sheet margin have advanced about 50 km during the past 3-4 kyrs. This is in fact supported by geological evidence in the area, which shows that the ice sheet may have expanded about 50 km during the last 4 kyrs [*Le Meur and Huybrechts*, 1996].

Table 6.5: Observed and modeled uplift rates in mm/yr.

Site name	Observed uplift [mm/yr]	ICE-3G [mm/yr]	GrB [mm/yr]
THUL	0.53 ± 0.54	-0.66	0.11
KELY	-3.80 ± 0.60	3.34	-5.56
KULU	0.99 ± 0.64	1.51	1.00
SCOB	-0.38 ± 0.69	0.40	0.01
QAQ1	3.23 ± 1.76	0.47	-1.18
NUUK	-1.68 ± 1.75	1.29	-4.79

Also surface temperature reconstructed from borehole measurements from the DYE3 ice-core suggest the ice margin (in average) have advanced during the past ~ 5 kyrs. Figure 6.13 (A) displays the temperature history over the past 30 kyrs at DYE3 and figure (B) displays the location of DYE3 (data is adopted from *Dahl-Jensen et*

al. [1998]). However, it should be noted, that the temperatures reconstructed from the ice-cores reflect average temperatures in the considered region and not the local temperature conditions in the area.

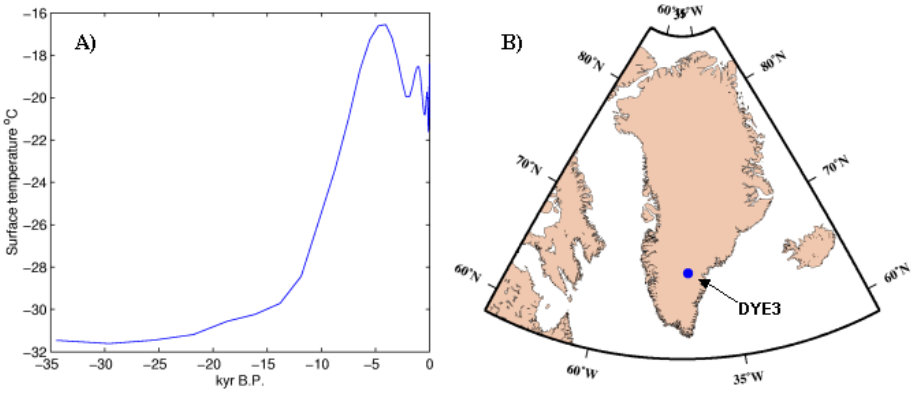

Figure 6.13: A) Surface temperatures reconstructed from the DYE3 ice-cores. B) Location of the DYE3 borehole

The last column in Table 6.5 displays uplift rates from the GrB deglaciation model [*Tarasov and Peltier*, 2002]. Unlike ICE-3G and ICE-4G, the latest model does include deglaciation history during the past 4 kyrs. Hence, the model does contain the ice-sheet margin advancement effect in west Greenland. Furthermore, the model is tuned to fit the uplift rates at the GPS sites at THU1, KELY and KULU. Figure 6.14 displays the GrB uplift model. The subsidence rate in south-west Greenland is almost 9 mm/yr.

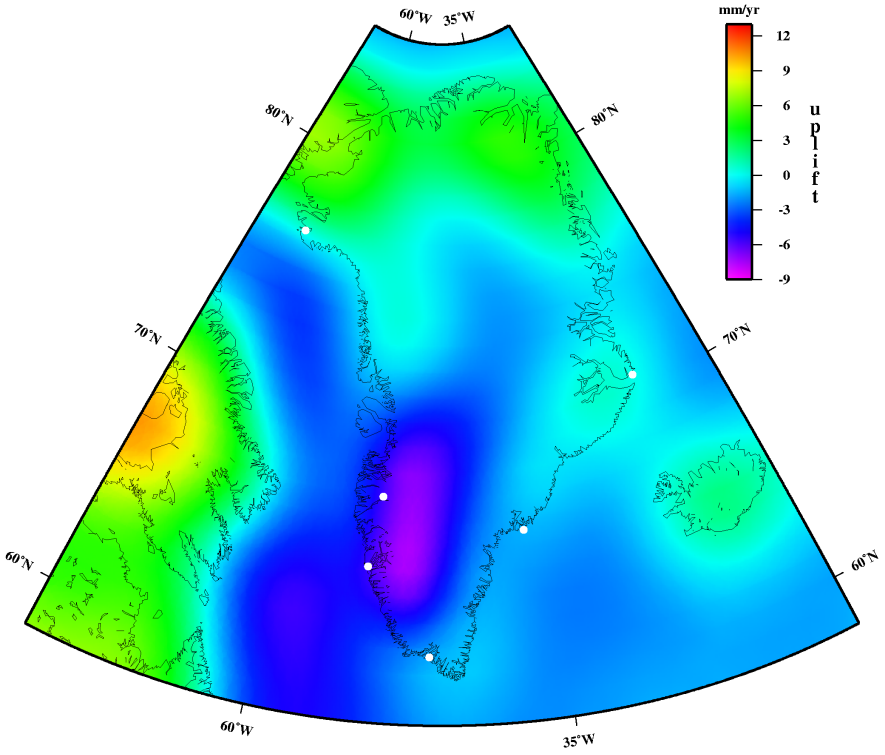

Figure 6.14: GrB uplift rates in mm/yr. The white dots denote GPS and tide gauge sites

6.7 Conclusion

The THU2 GPS station started operating in 1998, while the THU1 GPS station ended operating in the beginning of 2003. In order to reduce the frame error, data from both stations is used (since the frame error depends on the length of the data span). Using measurements from both Thule sites an average crustal uplift rate of 0.53 mm/yr ± 0.54 mm/yr is obtained. GPS measurements at KELY suggest an uplift rate of -3.80 ± 0.60 mm/yr. The negative uplift rate (=subsidence) is explained by *Wahr et al.* [2001] as a result of ice margin advancement in the area during the past 4 kyrs. However, GPS measurements at QAQ1 suggest crustal uplift rate of 3.23 ± 1.76 mm/yr, which indeed suggests, the ice margin advancement during the past 4 kyrs did not take place in this area. Additionally, the tide gauge in Nuuk suggests a crustal uplift rate of -1.68 ± 1.75 mm/yr, which indicate the ice margin have not as advanced much as 50 km during the past 4 kyrs as near KELY. The DYE3 temperature history confirms glaciation in southern Greenland during the past 4-5 kyr. However, GPS measurements at KULU suggest a crustal uplift rate of 0.99 ± 0.64 mm/yr. Hence, the glaciation was concentrated in western Greenland only.

The GrB deglaciation model is tied to GPS sites. Thus, we would expect the GPS and GrB uplift rates at KELY, KULU and THU1 to be identical. As displayed in Table 6.5 this not the case. The differences are caused by usage of different ITRF reference frames. The GrB model is tied to GPS results estimated using the ITRF 1997 reference frames, while the GPS results displayed in this thesis are obtained using the IGS 2000 reference frame.

Chapter 7

Crustal deformations at GPS sites in Denmark

7.1 Motivation

The National Survey and Cadastre (KMS) is responsible for the geodetic definition of the reference network in Denmark. Permanent GPS stations play an important role in the monitoring and maintenance of the geodetic network. During 1998 and 1999 KMS established three permanent GPS station in Denmark, SMID, SULD and BUDP. Using almost 4.5 years of continuous data from the Danish station and the Swedish station, ONSA, daily GPS solutions are analyzed due to crustal deformation caused by glacial isostatic adjustment (GIA). The present deformations due to the 'Late Glacial Temperature Minimum' (LGTM) in Fennoscandia have rates of more than 10 mm/year in the vertical direction in the northern Scandinavia. In the horizontal direction the displacements are smaller, about 1-3 mm/year. In Denmark, the postglacial rebound is relatively small in both the vertical and the horizontal direction. Figure 7.2 displays vertical and horizontal velocities obtained using the Milne-model [*Milne et al.*, 2001].

7.2 GPS Data Analysis

In September 1998 KMS established two permanent GPS stations, one in Suldrup (SULD) and one in Smidstrup (SMID). Besides these two stations a third station, BUDP, was established in Buddinge in January 1999. All three stations are mounted on solid concrete pillars, which are electrically heated to prevent thermal expansion. The data is of high quality and useful in many geophysical studies, e.g. continental drift, atmosphere loading or measurements of the postglacial rebound. Here, data measured during the period from January 1999 to April 2003 is used. Additionally, data from the Swedish permanent GPS station ONSA is used. The locations of the GPS stations are shown in Figure 7.2.

The GPS data have been analyzed using the GIPSY OASIS II software [*Zumberge et al.*, 1997] developed at the Jet Propulsion Laboratory (JPL). GPS orbits, Earth orientation, and clock products obtained by JPL based on a global network of GPS sites are used. Receiver clock parameters and atmosphere parameters were modeled and a cut-off angle of 15 degrees was used. The data were corrected due to

the solid Earth tide and the ocean tide loading effect. The amplitudes and phase lags of the main ocean tide loading signal were calculated by the online loading provider by H.-G. Scherneck, (www.oso.chalmers.se/∼loading) Using the precise point positioning approach, site coordinates were computed in the nonfiducial frame and then transformed the coordinates into the ITRF00 frame. The transformation parameters from the free-network estimates to ITRF00 for a particular day are available at the following ftp site,
sideshow.jpl.nasa.gov/pub/gipsy_products/x-files

The velocity vector, $\vec{V}$, describing the rigid plate motion is given by *Nocquet et al.*, [2001]

$$\vec{V} = \Omega\vec{X} \tag{7.1}$$

where $\vec{X}$ is the site coordinate vector and Ω is the Euler matrix,

$$\Omega = \begin{pmatrix} 0 & -w_z & w_y \\ w_z & 0 & -w_x \\ -w_y & w_x & 0 \end{pmatrix}$$

Furthermore, the rotation parameters used in our study are (w_x, w_y, w_z) = (0.081 ± 0.021, 0.489 ± 0.008, -0.792 ± 0.026) given in mas/year. These parameter are adopted from *Kierulf et al.* [2003]. In addition, postglacial rebound is taken into account in the estimation of these parameters. Hence, postglacial rebound is not absorbed in the estimation of the rigid plate rotation parameters *Kierulf et al.* [2003].

7.3 Results

Daily solutions of site positions obtained using the GIPSY OASIS II software are shown in Figure 7.1. The mean value of the particular component (north, east and vertical) is removed. The left figures show the north-south component (counted positive in the north direction). The figures in the middle show the east-west component (counted positive in the east direction) and the right figures show the vertical component (counted positive upward). The displacements are given in mm. From top to bottom, time series of the four GPS sites, BUDP, SMID, SULD and ONSA are displayed. The solid light lines show a linear fit (using least square adjustment) to the daily point solutions. The rigid motion of Eurasia is significant and may be removed using site velocities calculated by equation 7.1. The estimated velocity residuals after removing the rigid plate rotation are shown in Table 7.1. In order to estimate the error, the 1σ formal errors generated by the GIPSY OASIS II software are used. Furthermore, it is assumed that the errors are uncorrelated due to time. Errors in the vertical due to the reference frame drift are simply estimated by assuming that the drift error is given as (see*Argus and Heflin*, [1995]).
$\sigma_{drift} = 5/(\text{number of years})$
Thus, we get
$\sigma = \sqrt{\sigma^2_{drift} + \sigma^2_{GIPSY}}$
Similarly the horizontal errors are obtained by adding (in quadrature) the error of the rigid plate rotation (see previous section). The last column in Table 7.1 shows

the modeled glacial isostatic adjustment by *Milne et al.*, [2001]. The model is based on the ICE-3G ice model and the PREM Earth model with a lithosphere thickness

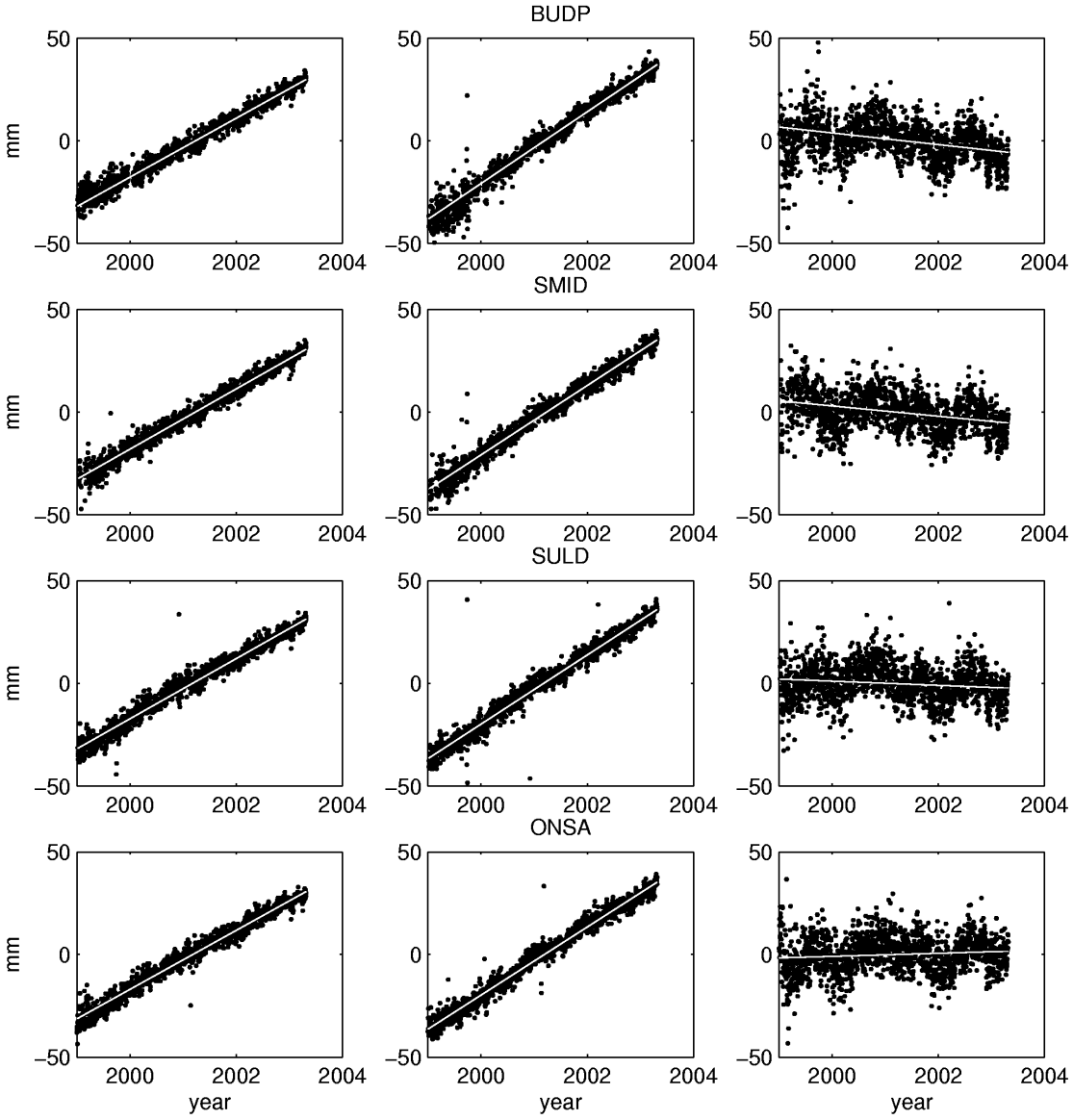

Figure 7.1: Time series of site positions obtained using the GIPSY OASIS II software. The mean value of each component (north, east and vertical) is subtracted. The left figures show the north component, the figures in the middle show the east component and the right figures show the vertical component (all components are given in mm). From top to bottom, we display the four GPS sites, BUDP, SMID, SULD and ONSA. The solid light lines show a linear fit to the observations.

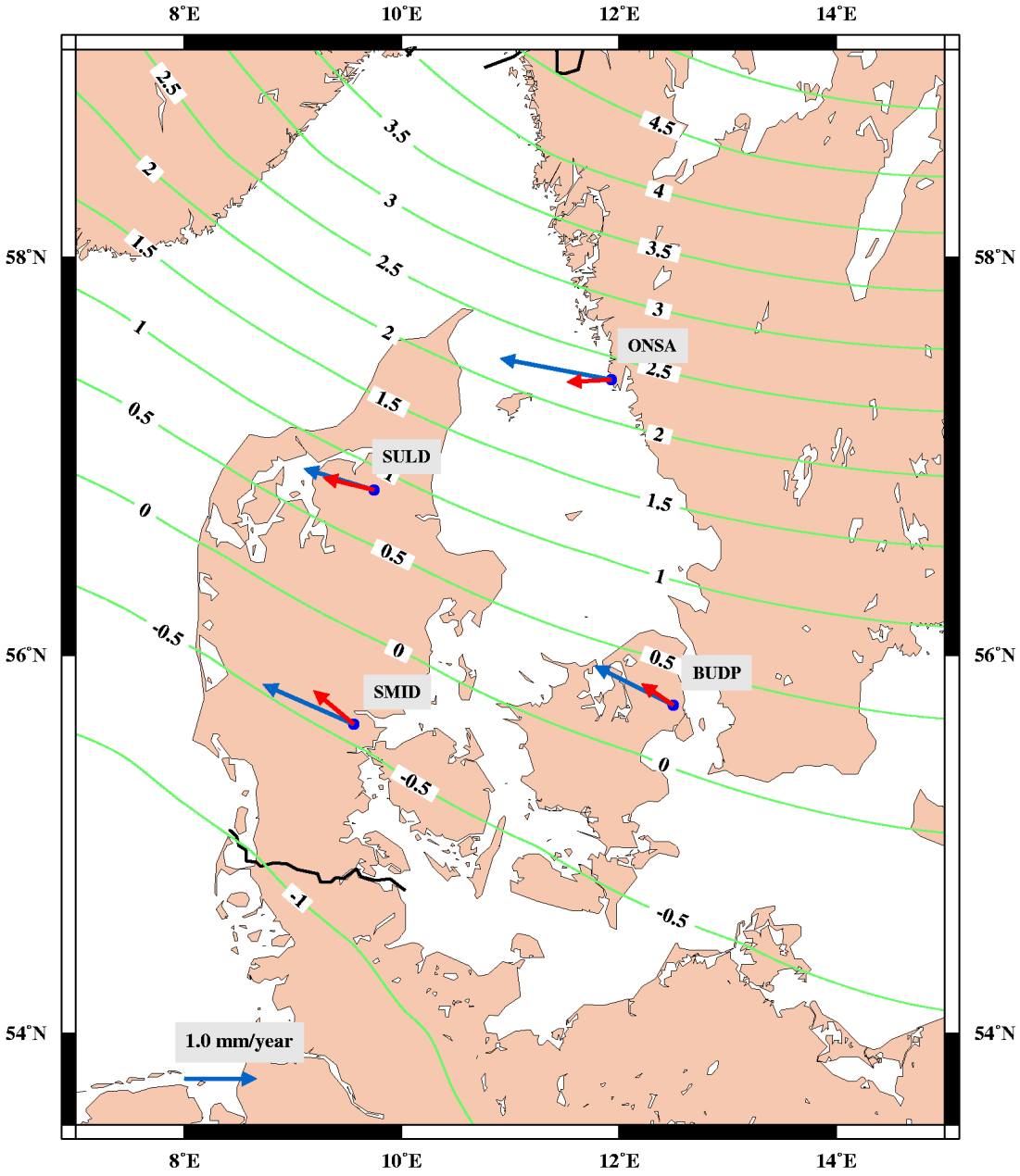

Figure 7.2: The solid lines displays contours [with interval of 0.5 mm/year] of the vertical velocity rates based upon the GIA model by Milne and the red collored vectors display the horizontal velocity rates due to the Milne model. The blue vectors display the observed horizontal velocity residual.

Table 7.1: Modeled and observed, vertical and horizontal GIA rates in mm/yr.

Station name		GPS residual [mm/year]	error [mm/year]	predicted GIA (Milne) [mm/year]
BUDP	North	0.54	0.36	0.30
	East	-1.09	0.42	-0.44
	Vertical	-3.58	1.13	0.24
SMID	North	0.55	0.35	0.47
	East	-1.26	0.42	-0.56
	Vertical	-2.66	1.12	-0.45
SULD	North	0.31	0.35	0.18
	East	-1.00	0.41	-0.71
	Vertical	-1.07	1.11	0.80
ONSA	North	0.29	0.35	-0.03
	East	-1.54	0.41	-0.62
	Vertical	0.70	1.11	2.26

of 120 km. For all the stations, the observed velocity residuals are larger than the modeled glacial isostatic adjustment. This is displayed more illustratively in Figure 7.2. The solid lines displays contour lines of the vertical velocities rates according to the GIA model by Milne and the red colored vectors display the horizontal velocity rates due to the Milne GIA model. The blue vectors display the observed horizontal velocity residual. The modeled horizontal GIA velocities and the observed horizontal residuals show almost the same direction for all station. However, the observed velocity residuals are larger than the modeled velocities at all station. This may indicate that the modeled GIA velocities are too small by a factor, or perhaps the rigid plate motion is not fully removed.

Daily point solutions of the vertical displacements obtained by the GIPSY OASIS II software (displayed in Figure 7.1, right) can be better determined if one of the stations are kept fixed. However, then we have to consider relative deformations between the sites. In addition, the rate of the vertical velocity residual is very much dependent on which reference frame is used. Hence, using e.g. the ITRF97 different results from those listed in Table 7.1 would be obtained. Therefore, it is more appropriate to compare differences in the vertical velocities between the involved stations rather than the absolute values. The difference of the observed vertical velocity residual rate between ONSA and SMID seems to agree with the expected rate according to the Milne GIA model. Furthermore, the observed residual rate between ONSA and SULD seems to be consistent with the model rate. However, when considering the difference of the vertical rate between ONSA and BUDP, there seems to be a disagreement between the observed and the modeled rates. BUDP is moving downward with a velocity rate, which is not explainable with the GIA only.

7.4 Conclusion

Data from the three Danish and the one Swedish continuously operating GPS stations have been analyzed due to vertical and horizontal displacements. The modeled horizontal GIA velocities and the observed horizontal residuals show almost the same direction for all station. However, the observed velocity residuals are larger than the modeled GIA velocities. The reason for this disagreement could be that the rigid plate motion is not fully removed, or that the predicted GIA is not fully correct. However, this can be investigated using more GPS stations and by considering a larger area. The spatial distribution of the two effects is different. Hence, by considering a larger area it is possible to separate these effects. Furthermore, The difference of the observed vertical velocity residual rate between ONSA and SMID seems to agree with the expected rate according to the Milne GIA model. The observed residual rate between ONSA and SULD are also consistent with the model rate. However, BUDP is moving downward relative to ONSA by a velocity, which is almost twice the expected rate due to the GIA model.

Moreover, here almost 4 1/2 years of continues GPS data for each site is used. The sites are still operating and more data will contribute significantly for a better determination of the vertical component. In addition KMS have monitoring 3 new stations, which started operating in 2004.

Chapter 8

Conclusion

Using GPS data from sites in Alaska, the M_2 ocean tide loading wave for vertical and horizontal displacements is measurable by DGPS. Surface displacements due to ocean tide loading can be well resolved in the analysis of GPS data using Strategy 3 (estimation of 1-h ZTD derived from 1-h solutions). The M_2 ocean tide loading and troposphere effects are very well separated. Indeed, no ocean loading is absorbed into the ZTD parameters using Strategy 3. However, when we use Strategy 2 (estimation of 1-h ZTD derived from 24-h solutions) loading is absorbed into the tropospheric modeling. More precisely, 23 percent of the $M2$ ocean tide loading amplitude is absorbed into the zenith delay amplitude at the $M2$ frequency. However, Strategy 3 introduces periodic signals with third-diurnal, quarter-diurnal and fifth-diurnal periods. If these signals are artifacts, we believe they can be avoided using e.g. using a 28-h observation windows instead of a 24-h windows.

GPS analysis of observations with the uncertainties and duration in the present work, 3 mm and 6 weeks, is able to resolve between different tide models. Improved coastline resolution appears to be a slightly smaller problem that is likely to become significant when the time series duration is longer, 0.5 to one year.

The differential ocean tide loading effect near the coastline of southern Alaska is huge. However, the differential loading effect is more than twice the size of the corresponding differential solid Earth tide effect. This is not a unique case; in addition, the differential ocean loading is found to be larger than the differential solid Earth tide effect for several near-coast regions worldwide e.g. southern England, Bay of Hudson and southern Africa.

A study involving shallow-water tides and GPS in the northwest European shelf area is currently ongoing. The purpose of the study is to analyze GPS time series due to shallow-water tides and artifact signals in the third-diurnal, quarter-diurnal and fifth-diurnal tidal band. In order to separate the main shallow-water tides from artifact signal requires more than 1 year of hourly solutions. Also the diurnal and semi-diurnal band is currently being investigated in more detail (e.g. using different strategies for the tropospheric correction).

The semidiurnal ocean tide loading wave, M_2, is of major importance, because it is in general much larger than the other loading waves and it is undisturbed from the other signals (e.g. atmosphere, satellite orbit, software-generated signal, since these do not appear with the M2 frequency). The coastline resolution nowadays is very accurate and the ocean tide models are getting better and better, thus, we are getting close to being able to evaluate the Greens function using GPS! Since

GPS sites are located almost everywhere, a very good spatial coverage of the Earth Elasticity may be achieved (at least on the continents).

Using measurements from both Thule sites an average crustal uplift rate of 0.53 mm/yr ± 0.54 mm/yr is obtained. GPS measurements at KELY suggest an uplift rate of -3.80 ± 0.60 mm/yr. The negative uplift rate (=subsidence) is explained by Wahr et al. [2001] as a result of ice margin advancement in the area during the past 4 kyrs. However, GPS measurements at QAQ1 suggest crustal uplift rate of 3.23 ± 1.76 mm/yr, which indeed suggests, the ice margin advancement during the past 4 kyrs did not take place in the this area. Additionally, the tide gauge in Nuuk suggests a crustal uplift rate of -1.68 ± 1.75 mm/yr, which indicates that the ice margin have not advanced as much as 50 km during the past 4 kyrs as near KELY. The DYE3 temperature history confirms glaciation in southern Greenland during the past 4-5 kyrs. Additionally, ice core studies from other areas in Greenland also show glaciation during the past 4-5 kyrs, however, the largest temperature fluctuations were found in southern Greenland. Furthermore, measurements at KULU suggest a crustal uplift rate of 0.99 ± 0.64 mm/yr. Thus, the glaciation was most likely only concentrated in western Greenland.

The convergence plot (Figure 6.9) for THUL looks good and shows that the uplift rate for THUL has more or less stabilized. However, the convergence plot for KELY is quit warning. Even after 10 years of data the uplift rate has not stabilized. The question is what is causing the disturbances? Are there multi-year variations in the uplift signal caused by e.g. changes in the ice-mass volume? Can GPS orbit errors generate multi-year variation? For instance, what happens if JPL uses 300 sites to obtain clock and orbit parameters instead of 200 sites? Will that produce an small offset in the GPS site coordinates? What about the nearby ocean, is the ocean causing the disturbances? Multi-year signals have already been detected in the ocean (Figure 6.11) near NUUK; can these produce Elastic deformation at millimeter level? What is the range of the multi-year variations near KELY?

Like the vertical secular displacements, the horizontal secular displacements do also contain important information about the deglaciation history and may be used to improve existing deglaciation models. In the near future, the horizontal motions will be analyzed. In order to remove the rigid plate motion effect, new rotation parameters have to be estimated and we have to make sure that PGR is not absorbed in the estimation of the rigid plate rotation.

The GPS and tide gauge uplift rates presented here are to be incorporated (by W R Peltier, *personal communication*) in a new version of the ICE-5G uplift model.

The European Center for Geodynamics and Seismology (ECGS) is planning to establish 5 new GPS station at the west coast of Greenland and KMS is planning to establish 1 new GPS station also at the west coast of Greenland. The purposes of these new GPS stations is to obtain a better spatial distribution of the ice re-advancement during the last 5-6 kyrs. KMS is also considering new GPS stations in North and East Greenland. At the moment, SCOB is the only GPS station in this area of Greenland.

One of the purposes of this thesis was to study the annual and semi-annual variation. However, the time did not allow me to investigate these signals in detail. They are therefore not included in this thesis. These variations will be investigated in detail in the nearest future. I would like to say that the annual signal is probably

very difficult to study, because it has so many sources. Just to mention few of them, atmosphere loading, geocenter motion, seasonal ice mass balance...

Chapter 9

Literature

Agnew, Duncan Carr, Conservation of mass in tidal loading computations, *Geophys. J. R. astr. Soc.*, 72, 321-325, 1983.

Andersen, Ole Baltazar, Shallow water tides in the northwest European shelf region from TOPEX/POSEIDON altimetry, *J. Geophys Res.*, 104 (C4), 7729-774, 1999.

Argus, D.F and M.B. Heflin, plate motion and crustal deformation estimated with geodetic data from the Global Positioning System *Geophys. Res. Lett.*, 22, 1973-1976, 1995.

Baker, T F, Bos M S, Tidal gravity observations and ocean tide models *J Geodetic Soc Japan*, 47(1): 76-81, 2001.

Baker, Trevor F., Deborah J. Curtis and Alan H. Dodson, Ocean Tide Loading and GPS, *GPS WORLD*, 54-59, March 1995.

Baker, Trevor F., R. J. Edge and G. Jeffries, Tidal gravity and ocean tide loading in Europe, *Geophys. J. Int.*, 107, 1-11, 1991.

Baker, Trevor F., D. J. Curtis and A. H. Dodson, A new test of Earth tide models in central Europe, *Geophys. J. Int.*, vol 23, 24, 3559-3562, 1996.

Beutler, G., H. Bock, E. Brockmann, R. Dach, P. Fridez, W. Gurtner, U. Hugentobler, D. Ineichen, J. Johnson, M. Meindl, L. Mervart, M. Rothacher, S. Schaer, T. Springer, R. Weber, Bernese GPS Software Version 4.2 *UNIVERSITY OF BERNE*, Switzerland, 2000.

Black, H. D., An easily implemented algorithm for the tropospheric range correction, *J. Geophys Res.*, 83 (B4), 1978.

Chambers, D.P., J.C. Ries, C.K. Shum, and B.D. Tapley, On the use of tide gauges to determine altimeter drift, *J. Geophys. Res.*, 103 (C6), 12885-12890, 1998.

Chambers, D.P., J.C. Ries, and T.J. Urban, Calibration and Verification of Jason-1 Using Global Along-Track Residuals with TOPEX, *Marine Geodesy*, 26 (3), 305-317, 2003.

DACH, R., AND R. DIETRICH, Influence of the ocean loading effect on GPS derived precipitable water vapor, *Geophys. Res. Lett.*, 18, 2953-2958, 2000.

DAHL-JENSEN D., K. MOSEGAARD, N. GUNDESTRUP, S.J. JOHNSEN, A.W. HANSEN, G.D. CLOW AND N. BALLING, Past temperatures directly from the Greenland ice Sheet. *Science*, Vol. 282, p. 268-271, Oct. 1998

DEHANT, V , Tidal parameters for an inelastic Earth *Phys Earth planet Inter*, 49: 97-116, 1987.

DEHANT, V AND J. ZSCHAU, The effect of mantle inelasticty om tidal gravity: a comparison between the spherical and the elliptical Earth model, *Geophysical Journal*, 97, 549-555, 1989.

DODSON, A. H. AND T. F. BAKER, Ocean tide loading effects on height, *Geodesy Surveying in the Future, The impottance of heights*, Gavle, Sweden, 15-17 March, 1999.

DRAGERT, H. AND R. D. HYNDMAN, Continuous GPS monitoring of elastic strain in the northern Cascadia subduction zone, *Geophysical Research Letters*, vol. 22, no.7, Apr. 1, 755-558, 1995.

DRAGERT, H., T. S. JAMES, AND A. LAMBERT, Ocean loading corrections for continuous GPS: A case study at the Canadian coastal site Holberg, *Geophys. Res. Lett.*, 27: 2045-2048, 2000.

DZIEWONSKI, A.M. AND ANDERSON, D.L., Preliminary reference Earth model *Phys. Earth planet. Inter.*, 25, 297-356, 1981.

EGBERT, G. D., BENNETT, A. F., AND FOREMAN, M. G. G., TOPEX/POSEIDON tides estimated using a global inverse model, *J. Geophys. Res.*, 99(C12), 24,821-24,852, 1994.

EGEDAL, J., The sinking of Greenland, *Meddelelser om Grønland*, 1947.

FARREL W. E., Deformation of the Earth by Surface Loads, *Reviews of Geophysics and Space Physics*, vol. 10, no. 3, 762-795, Aug 1972.

FRANCIS, O. AND P. MAZZEGA, GLOBAL CHARTS OF OCEAN TIDE LOADING EFFECTS, *J. Geophys Res.*, 95 (C7), 11.411-11.424, 1990.

FU, L.-L., AND A. CAZENAVE, Satellite altimetry and Earth sciences: a handbook of techniques and applications, *Academic Press*, 463 pp., San Diego, CA, 2000.

GEORGIADOU, Y. AND A. KLEUSBERG, On carrier signal multipath effects in relative GPS positioning, *man. geod.*, 13, 172-179, 1988.

GILL, A E , Atmosphere-Ocean Dynamics, *Academic Press*, San Diego, California, p 662, 1982.

GREGORIUS, THIERRY, GIPSY-OASIS II: How it works, NASA Jet Propulsion Labaratory, California Institute of Technology, Pasadena, USA, 1996.

HENDERSHOTT M. C., The Effects of Solid Earth Deformation on Global Ocean Tides, *Geophys. J. R. astr. Soc.*, 29, 389-402, 1972.

JENTZSCH, G, KNUDSEN P, RAMATSCHI M , Ocean tide loading affecting precise geodetic observations on Greenland: error account of surface deformations by tidal gravity measurements, *Phys Chem Earth*, 25(4): 401-407, 2000.

JOHANSSON, J.M., J.L. DAVIS, H.-G. SCHERNECK, G.A. MILNE, M. VERMEER, J.X. MITROVICA, R.A. BENNETT, G. ELGERED, P. ELOSEGUI, H. KOIVULA, M. POUTANEN, B.O. RNNNG, AND I.I. SHAPIRO, Continuous GPS measurements of postglacial adjustment in Fennoscandia, 1. Geodetic Results, *J. Geophys Res.*, vol. 107, no. B8, 2002.

JOHNSEN, SIGFUS J., D. DAHL-JENSEN, W. DANSGAARD AND N. GUNDESTRUP, Greenland palaeotemperatures derived from GRIP bore hole temperatures and ice core isotope profiles *Tellus*, 47B, 624-629, 1995.

KEIHM, S., V. ZLOTNICKI, C. RUF, AND B. HAINES, TMR drift and scale error assessment, *Report to TOPEX Project*, 1998.

KEIHM, S.J., V. ZLOTNICKI, AND C.S. RUF, TOPEX Microwave Radiometer performance evaluation, 1992-1998, *IEEE Transactions on Geoscience and Remote Sensing*, 38 (3), 1379-1386, 2000.

KHAN, S. A., AND C. C. TSCHERNING, Determination of semi-diurnal ocean tide loading constituents using GPS in Alaska, *Geophys. R. Lett.*, 99(C12), 28(11): 2249-2252, 2001.

KHAN S. A., AND HANS-GEORG SCHERNECK, The M_2 ocean tide loading wave in Alaska: vertical and horizontal displacements, modelled and observed *J. Geod.*, vol. 77, 117-127, 2003.

KHAN S. A., AND J. L. HØYER, Shallow-water loading tides in Japan from superconducting gravimetry *J. Geod.*, vol. 78, 245-250, 2004.

KHAN S. A., P. KNUDSEN AND C. C. TSCHERNING, Crustal deformations at permanent GPS sites in Denmark gravimetry *The Proceedings of the International Association of Geodesy*, 556-560, Sapporo Japan, 2003.

KIERULF, H.P., H.-P. PLAG, AND O. KRISTIANSEN, Towards the true rotation of a rigid Eurasia *EUREF Publication*, no. 11, Verlag des Bundesamtes für Kartographie undGeodäsie, Frankfurt am Main, 2003.

KIRCHNER, M., Study of local site displacements due to ocean tide loading using a GPS network in Island, *Research Report*, No. 184, Onsala Space Observatory, Sweden.

LAMBERT, A., S. D. PAGIATAKIS, A. P. BILLYARD AND H. DRAGERT, Improved ocean tide loading correction for gravity and displacement: Canada and nothern United States, *J. Geophys. Res.*, vol. 103, no. B12, 30231-30244, 1998.

Le Meur, E. and P. Huybrechts, A comparison of different ways of dealing with isostasy: examples from modeling the Antarctic ice sheet during the last glacial cycle, *Annals of Glaciology*, 23, 309-317, 1996.

Le Provost, C, Generation of overtides and compound tides, *Tidal Hydrodynamics*, John Wiley & Sons, New York, 269-320, 1991.

Le Provost, C., Genco, M. L., Lyard, F., Vincent, P., and Canceil, P., Spectroscopy of the world ocean tides from a finite-element hydrodynamic model, *J. Geophys. Res.*, 99(C12): 24,777-24,797, 1994.

Le Provost, C., and P. Vincent, Some Tests of Precision for a Finete Element Model of Ocean Tides, *Journal of computational physics*, 65, 273-291, 1986.

Lefévre, F., F. H. Lyard, Le Provost, C. and E. J. O. Schrama, FES99: A tide finite element solution assimilating tide gauge and altimetric information, *J. Atm. Oceano. Tech.*, 19 (9), 2000.

Leuliette, E.W., R.S. Nerem, and G.T. Mitchum, Calibration of TOPEX/ Posiedon and Jason altimeter data to construct a continuous record of mean sea level change, *Marine Geodesy*, pp. 79-94, 2004.

Longman, I. M., A Greens Function for Determinig the Deformation of the Earth under Surface Mass Loads (Theory), *J. Geophys. Res.*, vol. 67, no. 2, 845-850, 1962.

Longman, I. M., A Greens Function for Determinig the Deformation of the Earth under Surface Mass Loads (Computations and Numerical Results), *J. Geophys. Res.*, vol. 68, no. 2, 485-496, 1963.

Matsumoto, K., Takanezawa, T. and Ooe, M., Ocean Tide Models Developed by Assimilating TOPEX/POSEIDON Altimeter Data into Hydrodynamical Model: A Global Model and a Regional Model Around Japan, *J. of Oceanog.*, 56: 567-581, 2000.

Melchior, Paul, The Tides Of The Planet Earth, 1st ed., 1978, Pergamon Press, London.

Merriam, J B, Non-linear tides observed with the superconducting gravimeter, *Geophys J Int*, 123: 529-540, 1995.

Meurers, B, Superconducting gravimetry in geophysical research today *J Geodetic Soc Japan*, 47(1): 300-307, 2001.

Milne, G..M., J. L. Davis, Jerry X. Mitrovica, H.-G. Scherneck, J. M. Johansson, M. Vermeer, H. Koivula, Space-Geodetic Constraints on Glacial Isostatic Adjustment in Fennoscandia *Science 22*, vol. 291, 2001.

Mitchum, G.T., Comparison of TOPEX sea surface heights and tide gauge sea levels, *J. Geophys. Res.*, 99 (C12), 24,541-24,554, 1994.

MITCHUM, G.T., Monitoring the stability of satellite altimeters with tide gauges, *Journal of Atmospheric and Oceanic Technology*, 15 (3), 721-730, 1998.

MITCHUM, G.T., An Improved Calibration of Satellite Altimetric Heights Using Tide Gauge Sea Levels with Adjustment for Land Motion *Marine Geodesy*, 23 (3), 145-166, 2000.

MUKAI, A, TAKEMOTO S, HIGASHI T, FUKUDA Y, Oceanic tidal loadings estimated from gravity observations in Kyoto and Bandung *J Geodetic Soc Japan*, 47(1): 261-266, 2001.

NEREM, R.S, Global mean sea-level variations from TOPEX/Poseidon altimeter data *Science*, 268 (5211), 708-710, 1995.

NEREM, R.S., D.P. CHAMBERS, E.W. LEULIETTE, G.T. MITCHUM, AND B.S. GIESE, Variations in global mean sea level associated with the 1997-1998 ENSO event: Implications for measuring long-term sea level change *Geophys. Res. Lett.*, 26 (19), 3005-3008, 1999.

NEREM, R.S., B.J. HAINES, J. HENDRICKS, J.F. MINSTER, G.T. MITCHUM, AND W.B. WHITE, Improved determination of global mean sea level variations using TOPEX/POSEIDON altimeter data *Geophys. Res. Lett.*, 24 (11), 1331-1334, 1997.

NOCQUET, J.-M., E. CALAIS, Z. ALTAMIMI, P. SILLARD, C. BOUCHER, Intraplate deformation in western Europe deduced from an analysis of the International Terrestrial Reference Frame 1997 (ITRF97) velocity field, *J. Geophys. Res.*, vol. 106 , no. B6 , p. 11239, 2001.

PAGIATAKIS, SPIROS D., Stochastic significance of peaks in the least-squares spectrum, *J. Geod.*, In press, 1998.

PAGIATAKIS, SPIROS D., The response of a realistic Earth to ocean tide loading, *Geophys. J. Int.*, 103, 541-560, 1990.

PARKE, M. E., ROBERT H. STEWART, DAVID L. FARLESS AND DAVID E. CARTWRIGHT, On the Choice of orbits for an Altimetric Satellite to Study Ocean Circulations and tides, *J. Geophys. Res.*, vol. 92, no. C11, 11.693-11.707, 1987.

PELTIER W. R., VLBI baseline variations from the ICE-4G model of postglacial rebound, *Geophys Res. Lett.*, 22, no. 4, 465-468, 1995.

PELTIER W. R., Global glacial isostatic adjustment: palaeogeodetic and space-geodetic tests of the ICE-4G (VM2) model, *J. of quat. science*, 17(5-6), 491-510, 2002.

PETERSEN, FRODE, The Glaciers of the Blaesedalen in Disco, *Meddelelser om Grnland*, no. 6, 41-54, 1995.

PETERSEN, FRODE, Opmaalingsexpedition til Egedesminde-District 1897, *Meddelelser om Grnland*, 1898.

PRESS, W. H, W. T. VETTERLING, S. A. TEUKOLSKY, B. P. FLANNERY, Numerical Recipes in Fortran 77, Second ed., 494-502, Cambridge, 1992.

PUGH, D T, Tides, Surges and Mean Sea-level, A Handbook for Engineers and Scientists, John Wiley & Sons, New York, 472pp, 1987.

RAY, R., A Global ocean tide model from T/P altimetry: GOT99.2, *NASA Technical Memorandum*, 209478. NASA, Greenbelt, MD, USA, 1999.

RAY, R.D. AND B.V. SANCHEZ, Radial Deformation of the Earth by Oceanic Tidal Loading, *NASA Technical Memorandum*, 100743. NASA. Greenbelt, MD, USA, 1989.

ROTHACHER, M., G. BEUTLER, R. WEBER AND J. HEFTY, High-Frequency Variation of Earth Rotation from Global Positioning System Data, *J. Geophys. Res.*, 106 (B7): 13711-13738, 2001.

ROW, L. W., D. A. HASTINGS, AND P. K. DUNBAR, TerrainBase Worldwide Digital Terrain Data, CDROM. NOAA. National Geophysical Data Center. Boulder CO. USA, 1995.

SASAO, TETSUO AND JOHN M. WAHR, An excitation mechanism for the free 'core nutation', *Geophys. J. R. astr. Soc.*, 64, 729-746, 1981.

SCHERNECK, H.-G., J.M. JOHANSSON, G. ELGERED, J.L. DAVIS, B. JONSSON, G. HEDLING, H. KOIVULA, M. OLLIKAINEN, M. POUTANEN, M. VERMEER, J.X. MITROVICA, AND G.A. MILNE, BIFROST: Observing the Three-Dimensional Deformation of Fennoscandia *Ice Sheets, Sea Level and the Dynamic Earth*, Mitrovica, J.X. and B.L.A. Vermeersen (eds), pp. 69-93, AGU Geodynamics Series, Vol. 29, American Geophysical Union, Washington, D.C., 2002.

SCHERNECK, HANS-GEORG, Crustal Loading Affecting VLBI Sites, *Universety of Uppsala*, Report no.20, Department of Geodesy, UPPSALA 1983.

SCHERNECK, HANS-GEORG, A parametrized solid Earth tide model and ocean tide loading effects for global geodetic baseline measurements, *Geophys. J. int.*, 106, 677-694, 1991.

SCHERNECK, H.-G., J.M. JOHANSSON, AND F.H. WEBB, Ocean Loading Tides in GPS and Rapid Variations of the Frame Origin, *Geodesy beyond 2000 The Challenges of the First Decade. IAG General Assembly Birmingham*, 32-40, 2000.

SCHERNECK H-G, M. S. BOS, Ocean Tide and Atmospheric Loading *International VLBI Service for Geodesy and Astrometry 2002 General Meeting Proceedings*, NASA/CP-2002-210002 (in press), 2002.

SCHERNECK, HANS-GEORG AND RUDIGER HAAS, Effect of horizontal displacements due to ocean tide loading on the determination of polar motion and UT1, *Geophysical Research Letters*, vol. 26, no.4, feb. 15, 501-504, 1999.

SCHWIDERSKI, E. W., On Charting Global Ocean Tides, *Rev. Geophys. Space Phys*, 18(1): 243-268, 1980.

SEEBER, GÜNTER, Satellite Geodesy, de Gruyter, 1993, Berlin.

SUGDEN DAVID E., AND BRIAN S. JOHN, Glaciers and Landscape: A Geomorphological Approach *Edward Arnold*, London, 1976.

TARASOV, L. AND W.R. PELTIER, Greenland glacial history and local geodynamic consequences, *Geophys. J. Int.*, 150, 198-229, 2002.

TUSHINGHAM, A.M., AND PELTIER, W.R., ICE-3G: A new global model of late Pleistocene deglaciation based upon geophysical predictions of postglacial relative sea level, *J. Geophys. R.*, 96, B3, 4497-4523, 1991.

VAN DAM, T.M., G. BLEWITT, AND M. HEFLIN, Detection of atmospheric pressure loading using the Global Positioning *J. Geophys Res.*, 99, pp. 23939-23950, 1994.

VAN DAM, T.M. AND J.M. WAHR, Modeling environmental loading effects, Invited, Proceedings EGS, Ed. H.-P. Plag and S. Zerbini . *Physics and Chemistry of the Earth*, 23, 1077-1087, 1998

WAHR, J., The forced nutations of an elliptical, rotating, elastic and oceanless Earth, *Geophys. J. R. astr. Soc.*, 64, 705-727, 1981.

WAHR, J., Body tides on an elliptical rotating, elastic and oceanless Earth *Geophys. J. R. astr. Soc.*, 64, 677-703, 1981.

WAHR, JOHN M. AND TETSUO SASAO, A diurnal resonance in the ocean tide and in the Earth's load response due to the resonant free 'core nutation', *Geophys. J. R. astr. Soc.*, 64, 747-765, 1981.

WAHR, J., T. VAN DAM, K. LARSON, O. FRANCIS, Geodetic measurements in Greenland and their implications, *J. Geophys. Res.*, 106(B8), 16567-16582, 2001.

WESSEL, P., AND SMITH W. H. F., A global, self-consistent, hierarchical, high-resolution shoreline database, *J. Geophys. Res.*, 101(B4): 8741-8743, 1996.

WU, P. AND PELTIER, W. R., Glacial isostatic adjustment and the free air gravity as a constraint on deep mantle viscosity, *Goephys. J. R. astr. Soc.*, 74, 377-449, 1983.

WÜBBENA, G., Zur Modellierung von GPS Beobachtungen für die hochgenaue Positionsbestimmung, *Wiss.Arb.Univ*, no. 168, Hannover, 1991.

ZLOTNICKI, V., AND P. CALLAHAN, TOPEX and Jason Microwave Radiometer assessment against DMSP-SSM/I and TRMM/TMI, *Jason-1/TOPEX/Poseidon Science Working Team Meeting*, Biarritz, France, 2002.

ZUMBERGE, J.F., M.B. HEFLIN, D.C. JEFFERSON, M.M. WATKINS AND F.H. WEBB, Precise point positioning for the efficient and robust analysis of GPS data from large networks *J. Geophys. Res.*, 102, p. 5005-5017, 1997,

Appendix A

Formulas

A.1 Analytical expressions

The following equations are used to determine the Green's functions.

$$\sum_{n=0}^{\infty} P_n(\cos\alpha) = \frac{1}{2\sin(\frac{\alpha}{2})} \tag{A.1}$$

$$\sum_{n=0}^{\infty} nP_n(\cos\alpha) = -\frac{1}{4\sin(\frac{\alpha}{2})} \tag{A.2}$$

$$\sum_{n=1}^{\infty} \frac{1}{n}\frac{\partial P_n(\cos\alpha)}{\partial\alpha} = -\frac{\cos(\frac{\alpha}{2})\left[1+2\sin(\frac{\alpha}{2})\right]}{2\sin(\frac{\alpha}{2})\left[1+\sin(\frac{\alpha}{2})\right]} \tag{A.3}$$

$$\sum_{n=0}^{\infty} \frac{1}{n}P_n(\cos\alpha) = -\log\left[\sin(\frac{\alpha}{2}) + \sin^2(\frac{\alpha}{2})\right] \tag{A.4}$$

A.2 Gravity potential and gravity

The gravity potential due to surface load is given by,

$$\Upsilon_n = W_n + \Phi_n - gU_n \tag{A.5}$$

To find the derivative of the first and second potentials it is convenient to separate them. Assume, the potential, P, given as a function of spherical coordinates (θ, λ, r) is defined as,

$$P(\lambda,\theta,r) = S(\lambda,\theta)r^n \tag{A.6}$$

The derivative of P with respect to r is given by,

$$\frac{\partial P}{\partial r} = \frac{n}{r}S(\lambda,\theta)r^{n-1} = \frac{n}{r}P \tag{A.7}$$

The differentiation depends on 'n'. Thus, the first and second term in A5 yields,

$$W_n \propto r^n \Rightarrow \frac{\partial W_n}{\partial r} = \frac{n}{r} W_n \tag{A.8}$$

$$\Phi_n \propto \frac{1}{r^{n+1}} \Rightarrow \frac{\partial \Phi_n}{\partial r} = -\frac{n+1}{r} \Phi_n \tag{A.9}$$

The third term is given by,

$$gU_n = \frac{h_n^{'} W_n}{g} \frac{\partial \Upsilon}{\partial r} \tag{A.10}$$

$$\Downarrow$$

$$\frac{\partial (gU_n)}{\partial r} = \frac{h_n^{'} W_n}{g} \frac{\partial^2 \Upsilon}{\partial r^2} = \frac{h_n^{'} W_n}{g} \frac{2Gm}{r^3} \tag{A.11}$$

Setting $r = a$ and using the scale factor, $Gm = ga^2$, the last expression may be written as,

$$\frac{\partial (gU_n)}{\partial r} = \frac{2h_n^{'} W_n}{a} \tag{A.12}$$

Setting $r = a$ and substituting the equations A8, A9 and A12 into A5 and introducing the Load love numbers gives,

$$dg_{load}(\alpha) = \frac{\partial \Upsilon}{\partial r} = \frac{g}{m_e} \sum_{n=0}^{\infty} [n + 2h_n^{'} - (n+1)k_n^{'}] P_n(\cos \alpha) \tag{A.13}$$

A.3 Definition of the convolution integral

The convolution integral is generally defined as [Kreyszig, 1993]

$$h(t) = (f * g)(t) = \int_0^t f(\tau) g(t - \tau) d\tau \tag{A.14}$$

Thus, for a loading mass we defined the convolution integral as,

$$L(\vec{r}_{obs}) = \int \rho h(\vec{r}_{load}) G(|\vec{r}_{obs} - \vec{r}_{load}|) d\Omega \tag{A.15}$$

$\vec{r}_{obs}$ and $\vec{r}_{load}$ denotes the position vector (coordinates) of the observation point and load point. $d\Omega$ is a surface area element and it is a function of $\vec{r}_{load}$

Danish National Space Center – Scientific report

Danish National Space Center – Denmark, Scientific report series is an informal report series, published at irregular intervals.

1. Khan, Shfaqat Abbas. Surface deformations analyzed using GPS time series

Danish National Space Center
Juliane Maries Vej 30
DK-2100 København Ø
Phone +45 3532 5700
Fax + 45 3532 2475
Mail office@spacecenter.dk
www.spacecenter.dk